Freie Universität Berlin

Understanding the Interaction of CO and O$_2$ with MgO(001) and Supported Metal Atoms:
Towards Single-Atom Catalysis

INAUGURAL-DISSERTATION

To obtain the Academic degree
Doctor Rerum Naturalium (Dr. rer. nat.)

Submitted to
The Department of Biology, Chemistry and Pharmacy
of Freie Universität Berlin

By
Kai Töpfer
from Berlin

2019

This work was prepared under supervision of

PROF. JEAN CHRISTOPHE TREMBLAY, PH.D.
(CNRS/UNIVERSITÉ DE LORRAINE)

from
MAY 2015 UNTIL DECEMBER 2019

1st Reviewer: PROF. JEAN CHRISTOPHE TREMBLAY, PH.D.
2nd Reviewer: PROF. DR. BEATE PAULUS

Date of Defense: February 24th, 2020

Abstract

This thesis contributes to the fundamental understanding of the interactions of a single gold atom supported by a defective and defect-free MgO(001) surface in a mixed CO/O_2 atmosphere. Using cluster models and point charge embedding within a density functional theory framework, the CO oxidation reaction for a single gold atom is simulated on differently charged oxygen vacancies of MgO(001) to rationalise its experimentally observed lack of catalytic activity. The results show, that only the F^0 colour centre promotes the electron redistribution towards an adsorbed oxygen molecule and sufficiently weakens the oxygen bond, as required for a sustainable catalytic cycle. The moderate adsorption energy of the gold atom, however, cannot prevent the insertion of oxygen atoms into the vacancy, which remains after the formation of the first CO_2 molecule. The surface becomes invariably repaired, which set the focus on the chemistry on a defect-free MgO(001) surface. To contribute towards the field of heterogeneous single-atom catalysis, various analysis tools are used to shed light on the binding situation of supported group 11 metal atoms to the defect-free substrate and both CO and O_2 molecules. Cooperative effects are found to enhance the stability of CO upon co-adsorption with O_2 for all three metal centres. The results gives further insights to the lack of catalytic activity with respect to the CO oxidation under thermal conditions as a competition between $OC-O_2$ bond activation and surface diffusion leading to metal atom agglomeration.

For the simulation of surface dynamics, an accurate description of the potential energy surface is achieved for CO on a defect-free MgO(001) surface by parametrizing a reactive bond order force field to a new set of *ab initio* data. Theoretical investigation of the non-reactive scattering of CO from the surface are done by performing quasi-classical scattering dynamic simulations. The scattering behaviour for several incidence energies and different initial ro-vibrational states of impinging CO is evaluated, which illustrates the role of surface atom motion on energy transfer processes. The analysis of time of flight spectra and scattering angle distributions reveals two different scattering channels, which become particularly noticeable at low incidence energies due to the weak interaction potential of CO with MgO(001). The scattering process is strongly influenced by the anisotropy of the potential energy surface for CO impinging in upwards and downwards alignment. Eventually, the observations are in agreement with the established Baule model especially for the distinct scattering features at low incident energies.

Kurzzusammenfassung

Die Arbeit vertieft das Wissen über die Wechselwirkungen zwischen einzelnen Goldatomen auf defekthaltigen und defektfreien MgO(001)-Oberflächen in einer gemischten CO/O_2 Atmosphäre. Mit Hilfe der Cluster-Einbettungs-Methode und der Dichtefunktionaltheorie wird die Oxidationsreaktion von CO auf einen einzelnen Goldatom simuliert, welches verschieden geladenen Sauerstoff-Fehlstellen der Oberfläche besetzt, um experimentelle Ergebnisse nachzuvollziehen. Es zeigt sich, dass nur die neutral geladenen F^0-Fehlstellen durch Elektronenumlagerung in Richtung adsorbierten Sauerstoff-Molekülen in der Lage sind, die Sauerstoffbindung soweit zu schwächen, um eine katalytische Reaktion zu ermöglichen. Dennoch ist die moderate Bindungsenergie eines Goldatoms auf der Fehlstelle nicht ausreichend um die Einlagerung eines einzelnen Sauerstoffatoms zu verhindern, das nach der Bildung des ersten CO_2 Moleküls auf der Oberfläche zurückbleibt. Dies führt zur unwiderruflichen Reparatur der Oberflächendefekte. Deswegen verschiebt sich der Fokus auf die Chemie der defektfreien MgO(001)-Oberfläche. Es werden verschiedene Analysemethoden verwendet, um die Bindungsverhältnisse der Metalle der 11. Gruppe mit CO als auch O_2 zu verstehen und weitere Einblicke aud den Gebiet der heterogenen Einzelatom-Katalyse zu bekommen. Die gemeinsame Anlagerung von CO und O_2 auf allen drei Metallzentren verstärkt die jeweilige Adsorptionsstärke durch kooperative Effekte. Das Ausbleiben einer katalytischen Oxidation von CO unter thermischen Bedingungen wird durch die Ergebnisse unterstützt, vor allem wegen des Widerspruchs, sowohl gleichzeitig einen Bindungsbruch zu ermöglichen, ohne dabei die Metallatome zu größeren Clustern zusammenzuführen.

Für die Simulation von Oberflächenprozesse wurde eine präzise Beschreibung des Potentials von CO auf defektfreien MgO(001)-Oberflächen unter Einbezug reaktiver Kraftfelder entwickelt. Es sind quasi-klassische Streusimulationen von CO durchgeführt und dessen Streuverhalten bei verschiedenen Einschlagsenergien und Rotationsschwingungszuständen untersucht worden. Besonderes Augenmerk fällt dabei auf die Bewegungsmöglichkeit der Oberflächenatome. Die Spektren der Flugzeit und Verteilung der Streuwinkel deuten auf zwei verschiedene Streukanäle hin, welche sich vor allem bei schwachen Einschlagsenergien deutlich hervorheben. Dies ist im Einklang mit der schwachen Natur der Gas-Oberflächen-Wechselwirkung. Der Streuprozess hängt deutlich von der Orientierung des Kohlenmonoxids beim Einschlag ab, was an der Anisotropie der Potentialenergiefläche ersichtlich wird. Die Beobachtungen, vor allem bei kleinen Einschlagsenergien, stimmen

mit den Vorhersagen des etablierten Baule-Modells überein.

Contents

List of Publications

Paper A K. Töpfer and J. C. Tremblay
"How surface reparation prevents catalytic oxidation of carbon monoxide on atomic gold at defective magnesium oxide surfaces"
Phys. Chem. Chem. Phys. **18**, 18590–18597 (2016)
DOI: 10.1039/C6CP02339H

Paper B K. Töpfer and J. C. Tremblay
"First-Principle Investigations of the Interaction between CO and O_2 with Group 11 Atoms on a Defect-Free MgO(001) Surface"
J. Phys. Chem. A **122**, 2307–2317 (2018)
DOI: 10.1021/acs.jpca.8b00647

Paper C K. Töpfer, G. Füchsel and J. C. Tremblay
"Energy Transfers in a Weakly Coupled Gas-Surface System: The Scattering of CO from MgO(001)"
submitted, **2019**

Chapter 1

Introduction

The ability of catalysts to change the rate of a desired chemical reaction has an immeasurable importance for most of modern industrial processes.[1] Catalysts can be classified as heterogeneous, homogeneous or enzymatic in accordance to the phases of the catalytic material and the reactants, and have mostly in common to feature metal centres.[2,3] While homogeneous and enzymatic catalysts coordinate the metal centre in well-defined chemical environment, the heterogeneous ones range from bare metal surfaces, nanoparticles or clusters, to even single metal atom on surface support. The interest in the latter subject has been surging in recent years[4–13] and is referred to as single-atom catalysis by T. Zhang, J. Li and J. Liu and coworkers in 2011, when they reported about the high catalytic activity for CO oxidation on dispersed Pt atoms on FeO_x.[14] The main object of single-atom catalysis is the maximization of the surface to volume ratio, that ultimately reduce the amount of catalytic material required, providing it remains catalytic active. This strategy already proved successfully, e.g., for the CO oxidation on a single Pd atom supported by $MgO(001)$[15] in 2001 and with various metal atoms on FeO_x,[6,14] CeO_2,[16,17] Al_2O_3[18,19] and more.[20–23] It can further prohibits selectivity problems associated with non-uniform aggregates of metal cluster, which was shown by the successful, selective hydrogenation of 1,3-butadiene[24] or aerobic oxidation of allylic alcohols,[25] for instance. But then, it is still a common issue to provide sufficient anchoring or immobilization to the supported metal atom and to inhibit the conglomeration towards larger metal cluster.[5,26] Advances in both experiments and theory provide clear pictures of the surface structure and bonding properties. However, catalytic activity of dispersed metal atoms on supportive material were already proposed since 1925 by H. Taylor[27] and further studies found that catalytic reactions can depend

on dispersed atoms rather than clusters.[28–30]

Further developments in soft-landing techniques promoted the research of supported gold nanoparticles with decreasing size from nanoscale to subnanoscale.[31–35] Gold was actually long prevented from attention as a catalyst due to his perfect inertness in bulk form, until first evidences for the catalytic activity of small gold clusters were reported in the early 1970s.[36–38] Since M. Haruta and coworkers observed the catalytic propensity of small gold clusters in the late 1980s,[39–41] a large number of investigations, aiming to explain the high activity of various gold clusters, have been published.[42–47] Their results show, that the catalytic activity depends strongly on the shape and diameter of the gold cluster, and the support material has a large influence on the electronic properties of the gold as well.

Experiments in the gas phase revealed that Au_2^- is the smallest catalytically active cluster for the CO oxidation reaction.[48,49] The negative charge of the gold dimer was found to be crucial for weakening the O_2 bond, thus explaining the cluster activity. This is due to a partial electron transfer from the binding metal to the anti-bonding π^*-orbitals of O_2, benefiting from the unpaired electron in Au_2^-. Such effect is also found for further even-numbered Au_n^- clusters in the gas phase both experimentally[50,51] and in theory.[52–54] The charge of small supported gold clusters results from the electron redistribution between cluster and surface, which is very sensitive to their specific interaction.[55] Especially, the presence of oxygen vacancies in the metal-oxide support[56–58] and the proximity of an underlying metal support on oxide films of various thicknesses[59] have been shown to have a large influence on the charge of deposited gold clusters. Experiments, featuring the CO oxidation on selected Au_n clusters deposited on defective MgO(001) films at low temperatures, show no catalytic activity for single gold atoms and dimers, but demonstrate high catalytic activity for clusters with more than 8 gold atoms.[31] MgO is often chosen as a support for fundamental investigations on metal clusters, due to its stability and comfortable handling in experiments.[60]

Theoretical investigations based on density functional theory have been performed to shed light on the reaction mechanism at selected supported clusters.[61–64] These revealed that the gold clusters bind strongly to electron-rich oxygen vacancies, and that the oxidation reaction can proceed via both Eley-Rideal and Langmuir-Hinshelwood mechanisms. Comparatively little attention has been devoted to the smaller, inactive clusters. For one, a joint theoretical-experimental spectroscopic study of the properties of CO on

Au$_{1,2}$ at various defective sites (e.g., terraces, edges, etc.) has revealed the possibility of initial formation of a positively charged cluster during the catalytic cycle, in which CO adsorption would precede oxygen adsorption.[65] In the presence of oxygen, the number of these defective sites is relatively small, which may have lead in the past to an overestimation of the role played by colour centres as direct catalysts despite the reports of their importance on the catalytic activity on larger gold clusters is well established.[56–59] Arguing that Au$_{1-3}$ clusters would be too small to protect an oxygen vacancy in a mixed atmosphere, M. Amft and coworkers[66] demonstrated by means of first principle calculations that catalytic oxidation of CO by Au$_3$ on defect-free MgO(001) is sustainable.

In **paper A**, we investigate the catalytic CO reaction with O$_2$ on a single gold atom, Au$_1$, adsorbed on differently charged oxygen vacancies on a MgO(001) surface, in order to provide mechanistic understanding for its catalytic inertness. We aim at confirming by means of unbiased first principle calculations that surface reparation is the origin of this inertness, and explain how O$_2$ and CO interact with gold atoms at defective MgO(001) surfaces to nullify their catalytic activity.

To understand the CO oxidation reaction on gold atoms, it appears necessary to investigate its chemistry on defect-free substrates. While supported gold clusters on MgO(001) have demonstrated their potential for CO oxidation, the single-atom catalysis with such system remains unavailable. It is understood that reducing the size of supported metal clusters down to a single atom will affect their binding properties and their reactivity. The origin of the catalytic inertness of gold atoms on magnesium oxide must lie consequently in the subtle details of its electronic structure on the substrate and its interaction with the reagents.

In the following, **paper B** shows the results of our investigation about the co-adsorption behaviour of CO and O$_2$ on single atoms of the group 11 metals (Cu, Ag, and Au) on terrace sites of a defect-free MgO(001) substrate to understand their binding properties. Although they have not enjoyed the same popularity, small anionic silver clusters Ag$_n^-$, with respectively $n = 7, 9, 11$ silver atoms, were similarly found to exhibit a catalytic behaviour regarding the CO oxidation in the gas phase.[67] This activity can be traced back to the capacity of such small clusters to accommodate both reactants in a co-adsorbed intermediate, leading to a mechanism reminiscent of Langmuir-Hinshelwood reactions. On the contrary, neutral gold and silver clusters show only a weak interaction

with O_2 in the gas phase, preventing any further reaction. Nevertheless, Q. Xu and co-workers[68] demonstrated in experiments and supported by theoretical calculation the possibility of co-adsorbing CO and O_2 on group 11 atoms at low temperature. Although no reaction could be induced by thermal excitation, the formation of CO_2 was observed upon irradiation using light with wavelength above 340 nm.

Heterogeneous single-atom catalysis does not mean, that a catalytic cycle is completed by the metal atom alone. It also relies on the interaction with the substrate like the oxygen anion of the metal oxide. The anionic adsorption site could not only serve for metal anchoring, but could also tune the electronic properties of the metal atom by electron charge transfer, for instance. MgO(001) surfaces, supporting single gold and silver atoms, are reported to do not induce any net charge transfer, but effects strong polarization and hybridization on the metal atom.[55,57] However, the adsorption of CO atop gold atoms yields a net charge transfer from the metal to the adsorbate and causes a huge red-shift of the CO stretching frequency about $-300\,cm^{-1}$ lower than for the gas-phase vibration. It becomes thereby comparable to an anionic [Au-CO]$^-$ complex in the gas-phase,[69,70] while the neutral gas phase complex shows a red-shift of about $-100\,cm^{-1}$.[71,72] Thus, the interaction properties of a mixed CO/O_2 gas atmosphere with supported group 11 metal atoms can be heavily differentiate from the gas phase system and might lead to an important contribution to the field of single-atom catalysis. The impact is underlined by the observation, that already gold dimer and larger clusters on MgO(001) induce a tiny change in the stretching frequency of CO up to $-20\,cm^{-1}$.[70] In contrast, CO adsorbed on metal surfaces tends towards larger red-shifts, the more metal atoms are interacting with the molecule extending the electron back-donation into the $2\pi^*$ anti-bonding orbitals.[73]

As for the CO oxidation on supported gold nanoparticles by defective MgO(001), gas-surface reactions are found to be crucially sensitive on the surface structure.It is further reported that catalytic reactions can take place at the interface between support material and the nanoparticle.[74,75] This additionally necessitates an accurate treatment of the surface support to predict stationary states and reaction barriers. Ionic materials, like metal oxides, are well suitable to be modeled by cluster embedding methods. The advantage of finite sized cluster towards periodic density functional calculations is the lower demands in computational effort. Thus, even advanced coupled cluster methods can become affordable for small cluster sizes. In our studies, we have used the periodic electrostatic embedded cluster method, where the surface cluster will be put into a periodic

array of point charges ensuring the proper description of the Madelung potential.[76] It further allows a straightforward treatment of a single colour centre, which would require large unit cells in periodic density functional theory methods to minimise the perturbation due to long-range interactions between these vacancies.

On the other hand, MgO support appears chemically inert for CO and O_2 adsorption. Previous molecular beam experiments of non-reactive CO scattering from bare MgO(001) surfaces show a quasi-elastic scattering process, which appeared to be evident for a weak CO-MgO interaction.[77,78] The angular scattering distribution assumed a cosinus-liked dependence.[79] Its shape was not much affected by a decrease of the surface temperature from room temperature to 400°C suggesting low residence times of CO on the surface.[78] This is in accordance with heat of adsorption measurements revealing a weak CO-MgO(001) attraction with contributions arising possibly from dipole-polar surface interactions.[80] In general, the experimental quantification of especially weak adsorption strength is a non-trivial task and ranges from $0.4\,\mathrm{eV}$[81] to $0.14\,\mathrm{eV}$.[82] The situation on the theoretical side is very similar. Early *ab initio* calculations, performed on Hartree-Fock level of theory, suggest a binding energy of $0.4\,\mathrm{eV}$, while density functional theory yields energy values from 0 to $0.29\,\mathrm{eV}$, see ref. [83] and references therein. The reproduction of experimental values by electronic structure calculations is difficult due to a number of reasons,[84,85] including the fact that experiments themselves have uncertainties.

Molecular beam scattering experiments are a powerful technique to study reaction dynamics at gas-solid interfaces.[86,87] They allow to investigate the dependence of the applied conditions on the early steps in a chemical reaction. Reactive and non-reactive scattering experiments, performed on gas-surface systems, yield details about the reaction mechanism, topological features of the gas-surface interaction potential and energy transfer processes, which may occur in collision events. The importance of the initial ro-vibrational state of the incident molecule on its reactivity has often been investigated on systems including diatomic molecules.[88–90] State-to-state scattering experiments, performed at non-reactive conditions, additionally raise the possibility to screen the topology of the potential energy surface for the gas-surface interaction and to measure energy transfer processes.[91] The latter can only occur between different molecular degree of freedoms of poly-atomic gas molecules by internal vibrational energy redistribution, especially if there is a large mass mismatch between the molecular projectile and the surface atoms. Such energy conversions are ruled by the (electronic ground state) potential

energy surface and conserve the total energy of the molecule. Energy transfer processes between molecule and surface, however, are often associated with energy losses in the scattered particle, and can be mediated by two different dissipative channels, phononic and electronic. While the phononic channel is relatively well understood and commonly involved in systems with large gas-to-surface mass ratios, the electronic channel is less common and typically limited to low band-gap materials and metal catalysts.[92] The presence of dissipative channels may lead to a reduced reactivity, but such a correlation is not always found, particularly when energy losses occur in a molecular degree of freedom that is not aligned with the reaction coordinate.[93]

The experimental and theoretical efforts made to understand the elementary interaction of CO with MgO(001) emphasise its importance for the description of the more complex CO oxidation reaction on gold supported by MgO(001). In **paper C**, we present the first detailed theoretical dynamics investigation on the non-reactive scattering of CO from an ideal MgO(001) surface. The interaction potential is represented by a full-dimensional potential energy surface adopting a force-field approach, which we fitted to *ab initio* reference data obtained from embedded cluster calculations in accordance with the setup used in **paper B**. We are interested in determining energy transfer processes from the CO molecule to the MgO(001) surface, angular distributions, the importance of atom surface motion and that of the impact site for scattering properties.

This dissertation is structured as follows. Chapter 2 gives an overview of the basic quantum mechanical concepts used in this thesis, the density functional theory and an introduction into cluster embedding. It further presents the nudged elastic band method to determine the minimal energy path of a chemical reaction and the energy decomposition analysis to evaluate different chemical bonding situations. It briefly covers the theory behind molecular dynamic simulations and all applied concepts within. Chapter 3 lists the scientific publications which are part of my doctoral studies. Finally, the central findings of the publications are summarised in chapter 4 and discussed within the context of surface science.

Chapter 2

Theoretical Background

The challenge in modeling chemical systems and providing accurate prediction has a long history since the postulation of quantum mechanics. Many contributions lead to the possibilities for describing even complicated chemical systems in a sufficient and affordable manner, when at the beginning the smallest molecules and even atoms were hardly capable to describe properly. Nonetheless, the simulation of apparently even simple processes may still require classical mechanics to keep the computational costs feasible. The subsequent sections will and cannot comprise the fundamental rules of quantum mechanics nor the details and validation of the applied methods. It will rather provide an overview of the theoretical frameworks, which are necessary to understand the work arisen from this dissertation. The underlying literature will be given in the heading of each section, which also serves as a lead for more detailed insights into the concepts and methods. For the sake of simplicity, we write all equations in the compact form using atomic units.

2.1 Quantum Mechanics for Chemical Systems

In this section, we present the backbone describing the interaction within atoms and molecules in a single electronic state. First, we discuss the Schrödinger equation, a linear partial differential equation describing the wave function, that contains all possible information about a quantum chemical system corresponding to the non-relativistic Hamilton operator (Hamiltonian) for molecular systems. Next comes the Born-Oppenheimer ap-

proximation, a widely used assumption for simplifying and lowering the computational cost for the solution of the Schrödinger equation. Last, we briefly discuss the structure of the Hamiltonian to study chemical systems with periodic boundary conditions.

2.1.1 Schrödinger Equation for Electrons and Nuclei

[94, 95]

The central equation to characterise the total wave function $\mathbf{\Phi}\left(\mathbf{x}, \mathbf{R}, t\right)$ of a quantum chemical system is the time-dependent Schrödinger equation (TDSE)[96] ,

$$i\hbar\frac{\partial}{\partial t}\mathbf{\Phi}\left(\mathbf{x}, \mathbf{R}, t\right) = \hat{H}\mathbf{\Phi}\left(\mathbf{x}, \mathbf{R}, t\right) \quad , \tag{2.1}$$

where $\hat{H}$ is the Hamiltonian of the system and t corresponds to the time. The assumption of a time-independent Hamiltonian allows the separation of the variables in position and time. In that case, stationary states ϕ can be obtained by solving the simplified time-independent Schrödinger equation (TISE)

$$\hat{H}\phi\left(\mathbf{x}, \mathbf{R}\right) = E\phi\left(\mathbf{x}, \mathbf{R}\right) \quad . \tag{2.2}$$

The solution of this eigenvalue equation yields the stationary wave function ϕ with its respective energy values E. $\phi\left(\mathbf{x}, \mathbf{R}\right)$ depends on the coordinate $\mathbf{R} = \{\vec{R}_A\}_{A=1}^{N}$ of the N nuclei and $\mathbf{x}$ of n electrons, where $\mathbf{x} = \{\vec{x}_i\}_{i=1}^{n}$ includes the $3n$ spatial coordinates $\mathbf{r} = \{\vec{r}_i\}_{i=1}^{n}$ and n spin coordinates $\mathbf{s} = \{s_i\}_{i=1}^{n}$. For atomic and molecular systems, the non-relativistic and spin-free Hamiltonian describes the kinetic energy of the nuclei $\hat{T}_{\text{nuc}}$ and electrons $\hat{T}_{\text{el}}$, as well as the respective Coulomb interaction between the nuclei $\hat{V}_{\text{nuc}-\text{nuc}}$, the electrons $\hat{V}_{\text{el}-\text{el}}$, and between the nuclei and electrons $\hat{V}_{\text{nuc}-\text{el}}$.

$$\hat{H} = \hat{T}_{\text{nuc}}(\mathbf{R}) + \hat{T}_{\text{el}}(\mathbf{r}) + \hat{V}_{\text{nuc}-\text{nuc}}(\mathbf{R}) + \hat{V}_{\text{el}-\text{el}}(\mathbf{r}) + \hat{V}_{\text{nuc}-\text{el}}(\mathbf{r}, \mathbf{R})$$

$$= -\frac{1}{2}\sum_{A}^{N}\frac{1}{M_A}\nabla_A^2 - \frac{1}{2}\sum_{i}^{n}\nabla_i^2 + \sum_{A}^{N}\sum_{B>A}^{N}\frac{Z_A Z_B}{\overline{R}_{AB}} - \sum_{A}^{N}\sum_{i}^{n}\frac{Z_A}{\overline{r}_{Ai}} + \sum_{i}^{n}\sum_{j>i}^{n}\frac{1}{\overline{r}_{ij}} \tag{2.3}$$

∇_A^2 and ∇_i^2 denote the Laplacian operator for particle A and i, respectively. M_A and Z_A are the mass and core charge of the nuclei A and $\overline{R}_{AB}$, $\overline{r}_{Ai}$ and $\overline{r}_{ij}$ corresponds to the distance between the respective nuclei A, B and electrons i, j. Even if the Hamiltonian

is time-dependent, the solution of the TDSE can be described as a superposition of stationary states of time-independent Hamiltonian. The solution of the TISE is still a highly demanding many-body problem which cannot be solved analytically. It is numerically only exactly accessible for small molecular systems. Further simplification and especially approximations are necessary to numerically solve larger, more sophisticated molecular systems.

2.1.2 Born-Oppenheimer Approximation

[95, 97]

The large difference between the masses of electrons and atomic nuclei, even for the lightest ones, and the resulting difference in their velocities qualifies the separation of the electronic and nuclei motion. Thus, it is well justified to consider the nuclei as frozen in the perspective of the electrons, and, vice versa, the change of the electron positions as instantaneous to the motion of the nuclei. From the perspective of the electron, the nuclei stay in rest and their kinetic energy $\hat{T}_n(\mathbf{R})$ can be regarded as zero. The Hamiltonian for the electronic system $\hat{H}_{\text{el}}$ reduces to

$$
\begin{aligned}
\hat{H}_{\text{el}}\left(\mathbf{r}; \mathbf{R}\right) &= \hat{T}_{\text{el}}(\mathbf{r}) + \hat{V}_{\text{el}-\text{el}}(\mathbf{r}) + \hat{V}_{\text{nuc}-\text{el}}(\mathbf{r}; \mathbf{R}) + \hat{V}_{\text{nuc}-\text{nuc}}(\mathbf{R}) \\
&= \hat{T}_{\text{el}}(\mathbf{r}) + \hat{U}(\mathbf{r}; \mathbf{R}) \quad ,
\end{aligned}
\tag{2.4}
$$

where the potential energy between the nuclei $\hat{V}_{\text{nuc}-\text{nuc}}(\mathbf{R})$ becomes constant and is part of the effective potential on the electron $\hat{U}(\mathbf{r}; \mathbf{R})$. Consequently, the actual explicit dependency of the Coulomb potential between nuclei and electrons becomes parametric on the nuclear coordinates $\mathbf{R}$ as indicated by the semicolon.

$$
\hat{H}_{\text{el}}\left(\mathbf{r}; \mathbf{R}\right) \psi_\lambda\left(\mathbf{x}; \mathbf{R}\right) = \epsilon_\lambda\left(\mathbf{R}\right) \psi_\lambda\left(\mathbf{x}; \mathbf{R}\right)
\tag{2.5}
$$

The solution of the TISE with the electronic Hamiltonian for a fixed nuclear configuration $\mathbf{R}$ in equation (2.5) provides an electronic wave function $\psi_\lambda\left(\mathbf{x}; \mathbf{R}\right)$ of the electronic state λ with associated electronic energy ϵ_λ. With a complete set of orthonormal electronic wave functions, the total wave function can be written as a linear combination of these basis functions

$$
\mathbf{\Phi}\left(\mathbf{x}, \mathbf{R}, t\right) = \sum_\lambda \psi_\lambda\left(\mathbf{x}; \mathbf{R}\right) \chi_\lambda\left(\mathbf{R}, t\right) \quad ,
\tag{2.6}
$$

where $\chi(\mathbf{R}, t)$ is the time-dependent expansion coefficient and is usually referred as the nuclear wave function. This ansatz is known as Born-Huang expansion and exact as long as the summation is not truncated. After substituting equation (2.6) into the TDSE in (2.1) and using equation (2.5), the nuclear equation of motion is obtained by left-multiplying with the electronic wave function $\psi_\lambda^\dagger(\mathbf{r}; \mathbf{R})$ and integrating over the electronic coordinates

$$i\hbar \frac{\partial}{\partial t} \chi_\lambda(\mathbf{R}, t) = \left[\hat{T}_{\mathrm{nuc}}(\mathbf{R}) + \epsilon_\lambda(\mathbf{R}) + \sum_\nu \Lambda_{\lambda\nu}(\mathbf{R}) \right] \chi_\lambda(\mathbf{R}, t) \quad . \tag{2.7}$$

The kinetic or non-adiabatic coupling terms $\Lambda_{\lambda\nu}(\mathbf{R})$ contain the dynamical interaction between the electronic and nuclear motion by

$$\Lambda_{\lambda\nu}(\mathbf{R}) = -\sum_A^N \frac{1}{2M_A} \left[2 \langle \psi_\lambda | \nabla_A | \psi_\nu \rangle \cdot \nabla_A + \langle \psi_\lambda | \nabla_A | \psi_\nu \rangle \right] \quad . \tag{2.8}$$

Both terms in (2.8) involve the derivative of the electronic wave function with respect to the nuclear coordinates. Especially through the division by the atom masses M_A, they are typically smaller by orders of magnitudes compared to the other terms in (2.7). Exceptions can occur at configurations with energetically close lying electronic states. The neglect of these terms leads to the Born-Oppenheimer approximation.[98]

The solution of the electronic TISE for every nuclear configuration provides a set of energy values $\epsilon_\lambda(\mathbf{R})$, that corresponds to an effective potential for each electronic state λ on which the nuclei can move. These adiabatic potentials are labeled as potential energy surfaces (PES). The solution of the electronic TISE remains a challenging task even with the huge simplification introduced by the Born-Oppenheimer approximation and can only be achieved by approximate electronic structure methods.

2.1.3 Structure of the Hamiltonian for Periodic Systems

[99–102]

Periodicity in chemical systems can be found in many ways, for example in polymer chains, surfaces and crystals. All these systems can be described as an infinite repetition or translational symmetry of a fundamental unit cell in either one, two or three dimensions, respectively. The three dimensional lattice of such a unit cell can be described by the three basis vectors $\mathbf{a}_1$, $\mathbf{a}_2$ and $\mathbf{a}_3$ in real space with the length and the angles between them defining its shape. The periodic array of atoms, molecules or ions, that occupy the unit cell, is given by the Bravais lattice, whose points $\mathbf{L}$ are defined by the linear combination of the three basic vectors $\mathbf{a}_i$ weighted by the integers u_i.

$$\mathbf{L} = u_1\mathbf{a}_1 + u_2\mathbf{a}_2 + u_3\mathbf{a}_3 \tag{2.9}$$

Visually speaking, the atomic arrangement looks the same in every respect at each point on the lattice. Consequently, the effective potential of an electron within the system becomes periodically

$$\hat{U}(\mathbf{r} + \mathbf{L}) = \hat{U}(\mathbf{r}) \tag{2.10}$$

for each arbitrary translation along $\mathbf{L}$. Alternatively, the periodicity can be described by a lattice in reciprocal space, where each point $\mathbf{K}$ on such a reciprocal lattice is defined as a linear combination of reciprocal lattice vectors $\mathbf{b}_i$ weighted by the integers v_i.

$$\mathbf{K} = v_1\mathbf{b}_1 + v_2\mathbf{b}_2 + v_3\mathbf{b}_3 \tag{2.11}$$

Each reciprocal lattice vector is orthogonal to two of the three basic vectors in real space $\mathbf{a}_i$. They satisfy the condition

$$\mathbf{b}_i \cdot \mathbf{a}_j = 2\pi\delta_{ij} \quad , \tag{2.12}$$

where δ_{ij} is the Kronecker delta symbol.

The periodic boundary condition can be built into the theoretical framework as it was initially done by F. Bloch in 1929. He introduces the wave function for a particle in a periodic potential, like the electrons in a perfect crystal, also referred as Bloch wave.[103] The wave function of an orbital $\psi_n(\mathbf{k}, \mathbf{r})$, where $\mathbf{k}$ is a reciprocal vector and n is the band

index, has the form of a plane wave times a function called Bloch orbital $u(\mathbf{r})$ with the same periodicity as the system $u(\mathbf{k}, \mathbf{r}) = u(\mathbf{k}, \mathbf{r} + \mathbf{L})$.

$$\psi_n(\mathbf{k}, \mathbf{r}) = e^{i\mathbf{k}\cdot\mathbf{r}} u_n(\mathbf{k}, \mathbf{r}) \tag{2.13}$$

This implies that the wave function values at equivalent positions in different unit cells are related by

$$\psi_n(\mathbf{k}, \mathbf{r} + \mathbf{L}) = e^{i\mathbf{k}\cdot\mathbf{L}} \psi_n(\mathbf{k}, \mathbf{r}) \quad . \tag{2.14}$$

Two reciprocal vectors $\mathbf{k}_1$ and $\mathbf{k}_2$ are equivalent when they only differ by the reciprocal lattice vector $\mathbf{K}$. Thus, there is an equivalent to the unit cell in the reciprocal space which is called the (first) Brillouin zone. Only the $\mathbf{k}$ vectors in that small reference cell have to be taken into account. The real space analog to the Brillouin zone is the Wigner-Seitz cell. Applying the Bloch theorem on the electronic TISE in (2.4) yields

$$\hat{H}_{\mathbf{k},\text{el}} u_n(\mathbf{k}, \mathbf{r}) = \left(\frac{1}{2} \left(\frac{1}{i} \nabla + \mathbf{k} \right)^2 + \hat{U}(\mathbf{r}) \right) u_n(\mathbf{k}, \mathbf{r}) = \epsilon_n(\mathbf{k}) u_n(\mathbf{k}, \mathbf{r}) \quad . \tag{2.15}$$

Each of the orbital wave functions $\psi_n(\mathbf{k}, \mathbf{r})$ are associated to an energy eigenstate $\epsilon_n(\mathbf{k})$, which forms a continuous function in $\mathbf{k}$ in the case of an infinitely periodic system. These function provides a range of energies calling the band structure. The energy difference between the highest occupied energy level of the band structure and the lowest state of an empty band defines the band gap, which classifies periodic materials as a metal, semi conductor or insulator.

2.2 Electronic Structure of Surface Systems

In the following, the basics about the applied methods are described, that are used to solve the electronic structure of the treated surface systems. Density functional theory provides well suited methods to solve the electronic structure of surface systems. It allows to achieve an appropriate accuracy for the electronic energies at affordable computational cost. Modeling surface systems is mostly done using periodic boundary conditions or finite clusters. While the first uses the periodicity of a unit cell to describe the electronic structure of an infinite system, the latter describes the surface by a cluster of limited size, which is surrounded by a sufficiently sized grid of point charges corresponding to the charge of the cluster ions. Obviously, such embedded cluster are not suited for non-ionic metal systems (and due to the strong dependency of metal properties and cluster size), and are usually restricted to insulators or semi conductors. Otherwise, it allows a more effective modeling of defects or supported nanocluster than periodic methods. The computational capability limits the size of the unit cell, that can lead to unintended mutual disturbances between these nanostructures due to the periodicity, if the unit cell is not sufficiently large enough.

First insights in potential dynamic surface processes can be provided by the knowledge about the corresponding transitions states. The search for transition states is not always a straight forward task especially for more complex surface systems. But if the atomic configuration of the initial and final state are known, the nudged elastic band method is capable of converging towards the transition state on the reaction path. A tool to understand the forces behind the chemical binding properties is the energy decomposition analysis. It relates energy differences between electronic structures to bond characteristics and quantifies them.

2.2.1 Density Functional Theory

[94, 101, 104, 105]

Density Functional Theory (DFT) is a quantum mechanical method to investigate the electronic structure of many-body systems. Contrary to wave function based methods, where multi-dimensional wave functions contain all information about a quantum mechan-

ical system (see, e.g., Hartree-Fock method[97]), DFT determines the electronic structure with functionals depending only on the four-dimensional one-electron density $\rho_0(\vec{r})$ of the electronic ground state. The one-electron density of a system with n electrons is defined by the integral over the spin coordinates of all electrons and over all but one spatial orbital

$$\rho_0(\vec{r};\mathbf{R}) = n \int ... \int |\psi_0 (\vec{x}_1 \vec{x}_2, ..., \vec{x}_n; \mathbf{R})|^2 \ \mathrm{d}s_1 \mathrm{d}\vec{x}_2...\mathrm{d}\vec{x}_n \quad . \tag{2.16}$$

The electron density is normalized to the number of electrons

$$n = \int \rho_0(\vec{r};\mathbf{R}) \ \mathrm{d}\vec{r} \tag{2.17}$$

and can be interpreted by the probability $\rho_0(\vec{r};\mathbf{R})\mathrm{d}\vec{r}$ of finding any of the n electrons in the volume element $\mathrm{d}\vec{r}$ irrespective of its spin.

Modern DFT methods base on the theorems proven and published by P. Hohenberg and W. Kohn in 1964[106] . The first theorem implies, that the exact non-degenerate ground state can be uniquely described by the one-electron ground state density $\rho_0(\vec{r};\mathbf{R})$ in an external potential $V_{\text{ext}}(\vec{r};\mathbf{R})$. Hence, it is possible to construct a functional $E[\rho_0]$ that provides the exact ground state energy, if the exact electron density is given. The second theorem states, that for every trial electronic density $\tilde{\rho}_0(\vec{r};\mathbf{R})$, which is normalized to the number of n electrons, the variational principle is fulfilled

$$E_0 \leq E\left[\rho_0(\vec{r})\right] \quad . \tag{2.18}$$

In 1965, W. Kohn and L. J. Sham proposed a practical method for performing DFT calculations.[107] They suggest to map the true system onto a reference system of n non-interacting electrons in an effective potential $V_{\text{eff}}(\vec{r};\mathbf{R})$, that yields the same ground state electronic density as for the true system. The ground state wave function for a non-interacting system is exactly described by a single Slater determinant $\psi_S^{\text{KS}}(\mathbf{x};\mathbf{R})$ formed by a set of one-electron basis functions, the Kohn-Sham orbitals $\varphi(\vec{x};\mathbf{R})$

$$\psi_S^{\text{KS}}(\mathbf{x};\mathbf{R}) = \frac{1}{\sqrt{n}} \begin{vmatrix} \varphi_1(\vec{x}_1;\mathbf{R}) & \varphi_2(\vec{x}_1;\mathbf{R}) & ... & \varphi_n(\vec{x}_1;\mathbf{R}) \\ \varphi_1(\vec{x}_2;\mathbf{R}) & \varphi_2(\vec{x}_2;\mathbf{R}) & ... & \varphi_n(\vec{x}_2;\mathbf{R}) \\ \vdots & \vdots & & \vdots \\ \varphi_1(\vec{x}_n;\mathbf{R}) & \varphi_2(\vec{x}_n;\mathbf{R}) & ... & \varphi_n(\vec{x}_n;\mathbf{R}) \end{vmatrix} \quad , \tag{2.19}$$

which holds the antisymmetry principle of the wave function postulated by quantum theory.[108] The one-electron density $\rho_0^{\mathrm{KS}}(\vec{r}; \mathbf{R})$ derives from the Slater determinant as

$$\rho_0^{\mathrm{KS}}(\vec{r}; \mathbf{R}) = \sum_i^n |\varphi_i(\vec{x}; \mathbf{R})|^2 = \rho_0(\vec{r}; \mathbf{R}) \tag{2.20}$$

and is, in principle, identical to the electron density of the true system $\rho_0(\vec{r}; \mathbf{R})$. In terms of the Kohn-Sham framework, the ground state energy can be expressed as a functional of the one-electron density by

$$E_0\left[\rho_0\right] = T_{\mathrm{S}}\left[\rho_0\right] + V_{\mathrm{nuc-el}}\left[\rho_0\right] + J\left[\rho_0\right] + E_{\mathrm{XC}}\left[\rho_0\right] + V_{\mathrm{nuc-nuc}} \quad , \tag{2.21}$$

where the non-interacting kinetic energy of the electrons is calculated from the Kohn-Sham orbitals

$$T_{\mathrm{S}}\left[\rho_0\right] = -\frac{1}{2} \sum_i^n \left\langle \varphi_i \left| \nabla_i^2 \right| \varphi_i \right\rangle \quad . \tag{2.22}$$

The next two terms of equation (2.21) cover the Coulomb interaction between the nuclei and the electron density

$$V_{\mathrm{nuc-el}}\left[\rho_0\right] = -\sum_A^N \int \frac{Z_A}{|\vec{r} - R_A|} \rho_0(\vec{r}; \mathbf{R}) \, \mathrm{d}\vec{r} \quad , \tag{2.23}$$

and between the electrons, which also called Coulomb repulsion $J\left[\rho_0\right]$

$$J\left[\rho_0\right] = \frac{1}{2} \int \int \frac{1}{|\vec{r} - \vec{r}'|} \rho_0(\vec{r}; \mathbf{R}) \rho_0(\vec{r}'; \mathbf{R}) \, \mathrm{d}\vec{r} \mathrm{d}\vec{r}' \quad . \tag{2.24}$$

The nuclear-nuclear repulsion $V_{\mathrm{nuc-nuc}}$ stays constant in the context of the Born-Oppenheimer approximation. The exchange-correlation energy E_{XC} includes the difference between the electronic kinetic energy of the exact $T\left[\rho_0\right]$ and non-interacting system $T_{\mathrm{S}}\left[\rho_0\right]$ as well as the respective error in the electronic exchange and correlation of the Coulomb repulsion

$$E_{\mathrm{XC}}\left[\rho_0\right] = \left(T\left[\rho_0\right] - T_{\mathrm{S}}\left[\rho_0\right]\right) + \left(V_{\mathrm{el-el}}\left[\rho_0\right] - J\left[\rho_0\right]\right) \quad . \tag{2.25}$$

The last difference also contains the nonphysical behaviour of the electron interaction with its own electron density, which is known as the self-interaction error. In general, the exchange-correlation functional can be respectively split into an exchange E_{X} and

correlation E_C part

$$E_{XC}[\rho_0] = E_X[\rho_0] + E_C[\rho_0] \quad . \tag{2.26}$$

In accordance with the second Hohenberg-Kohn theorem, the electron density can be now variationally calculated in the Kohn-Sham framework. The electronic energy is minimized through the variation of the Kohn-Sham orbitals $\varphi_i(\vec{x}; \mathbf{R})$ by simultaneously retaining their orthonormality

$$\langle \varphi_i | \varphi_j \rangle = \delta_{ij} \tag{2.27}$$

and solving the single-particle Kohn-Sham equation[109]

$$\left(-\frac{1}{2} \nabla_i^2 + \hat{V}_{\text{eff}}(\vec{r}; \mathbf{R}) \right) \varphi_i(\vec{x}; \mathbf{R}) = \epsilon_i(\mathbf{R}) \varphi_i(\vec{x}; \mathbf{R}) \quad . \tag{2.28}$$

The effective potential $\hat{V}_{\text{eff}}(\vec{r}; \mathbf{R})$, seen by the single electrons, is given by

$$\hat{V}_{\text{eff}}(\vec{r}; \mathbf{R}) = -\sum_A^N \frac{Z_A}{(|\vec{r} - R_A|)} + \int \frac{1}{|\vec{r} - \vec{r}'|} \rho_0(\vec{r}'; \mathbf{R}) \, \mathrm{d}\vec{r}' + \hat{V}_{\text{XC}}(\vec{r}; \mathbf{R}) \quad . \tag{2.29}$$

The exchange-correlation potential $\hat{V}_{\text{XC}}(\vec{r}; \mathbf{R})$ is defined as the functional derivative of the exchange-correlation energy $E_{XC}[\rho_0]$ with respect to the electron density $\rho_0^{\text{KS}}(\vec{r}; \mathbf{R})$

$$\hat{V}_{\text{XC}}(\vec{r}'; \mathbf{R}) = \frac{\delta E_{XC}[\rho_0]}{\delta \rho_0(\vec{r}; \mathbf{R})} \quad . \tag{2.30}$$

Actually, the Kohn-Sham formalism is in principal exact for the calculation of the ground state electronic structure of many-body systems, but the analytical form of the exchange-correlation energy is still unknown, even if the first Hohenberg-Kohn theorem states the existence of such an expression. Thus, approximations of the exchange-correlation energy are inevitable and the development of more accurate exchange-correlation functionals is still in progress. Unfortunately, the mostly empirical nature prevents them from being systematically improvable. The "Jacob's ladder" approach, suggested by J. P. Perdew[110], gives a heuristic characterization of the expected accuracy of the exchange-correlation functionals by their use of fundamental variables.

The simplest approximation of the exchange-correlation functional is the local density approximation (LDA), where the electron density is treated locally as a homogeneous electron gas. Hence, the exchange-correlation functional can be written as

$$E_{XC}^{\text{LDA}}[\rho_0] = \int \rho_0(\vec{r}; \mathbf{R}) \epsilon_{XC}^{\text{LDA}}[\rho_0] \, \mathrm{d}\vec{r} \tag{2.31}$$

with $\epsilon_{\mathrm{XC}}^{\mathrm{LDA}}$ as the exchange-correlation energy of the homogeneous electron gas. The exchange part in the local density approximation $E_{\mathrm{X}}^{\mathrm{LDA}}$ was originally derived by F. Bloch and P. Dirac[94,111]. Even if no explicit expression is known for the correlation part $E_{\mathrm{C}}^{\mathrm{LDA}}$, it can be accurately derived by quantum Monte-Carlo simulations.[112–114] This simple approximation of the exchange-correlation energy performs surprisingly well for extended homogeneous systems like solid metals, but lacks accuracy for more inhomogeneous systems such as atoms or molecules. The problem is tackled by including the information about the gradient of the electron density $\nabla\rho_0(\vec{r};\mathbf{R})$ leading to functionals of the generalized gradient approximation (GGA).

$$E_{\mathrm{XC}}^{\mathrm{GGA}}[\rho_0] = \int \rho_0(\vec{r};\mathbf{R})\epsilon_{\mathrm{XC}}^{\mathrm{GGA}}[\rho_0, \nabla\rho_0]\,\mathrm{d}\vec{r} \qquad (2.32)$$

Famous representatives of GGA functionals are B88[115], PW91[116] and the various PBE functionals.[117–120] Further improvements can be achieved by including the second spatial derivative of the electron density $\nabla^2\rho_0(\vec{r};\mathbf{R})$ or, more popular, the kinetic energy density $\sum_i^n |\nabla\varphi_i(\vec{x};\mathbf{R})|^2$. Such functionals are known as meta-GGA approximations.

The inclusion of further variables based on the local electron density cannot remedy major limitations like the self-interaction error, long-range dynamic correlations and strong correlations. Further improvement is achieved by including the exact exchange $K^{\mathrm{HF}}[\{\varphi\}]$ from the Hartree-Fock formalism

$$\begin{aligned} K^{\mathrm{HF}}[\{\varphi\}] &= -\frac{1}{2}\sum_i^n\sum_j^n \int\int \varphi_i(\vec{x})\varphi_j(\vec{x}')\frac{1}{|\vec{x}-\vec{x}'|}\varphi_j(\vec{x})\varphi_i(\vec{x}')\,\mathrm{d}\vec{x}\mathrm{d}\vec{x}' \\ &\equiv E_{\mathrm{X}}^{\mathrm{HF}}[\{\varphi\}] \quad, \end{aligned} \qquad (2.33)$$

which is determined using the Kohn-Sham orbitals. The parametrically dependency to nuclear coordinates $\mathbf{R}$ of the Kohn-Sham orbitals is omitted in equation (2.33). The fractional mixing of the exact exchange to the exchange-correlation energy is tuned by a parameter c_x

$$E_{\mathrm{XC}}^{\mathrm{GH}}[\rho_0] = c_x E_{\mathrm{X}}^{\mathrm{HF}}[\{\varphi\}] + (1-c_x)E_{\mathrm{X}}^{\mathrm{DFT}}[\rho_0] + E_{\mathrm{C}}^{\mathrm{DFT}}[\rho_0] \qquad (2.34)$$

via the global hybrid (GH) formalism. Such electron-correlation functionals are generally referred as hybrid DFT functionals[121] and yield significant improvement upon their local counterparts. Two of the most popular hybrid DFT functionals are the non-empirical PBE0[122] functional with 25% exact exchange and the semi-empirical B3LYP

functional.[115,123,124] The latter contains three parameters, which are optimized to optimally reproduce atomization and ionization energies as well as the proton affinities included in the G2 data base[125] and some total energies.

2.2.2 Periodic Electrostatic Embedded Point Charge Method

[76, 126]

The simplest way to model a crystal surface non-periodically is just to describe a finite part of the surface, called cluster, without any modifications. Thus, it might be treatable by any program for finite, molecular-like structures but it also misses the environment and electrostatic potential of the crystal. The missing bulk environment and the dangling bonds can be at least saturated by hydrogen but the quality of the surface model still heavily depends on the size, shape and stoichiometry of the cluster. As a consequence, a variety of test calculation are mandatory to check for convergence of the cluster size and the accordance of surface properties such as lattice constants, bonding energies or excitation energies like the vertical ionization potential.

The embedding of the cluster into an extended field of point charges allows to preserve the correct electrostatic potential or Madelung potential approximately. Such embedding schemes divide the system into at least three regions. The first one contains the quantum mechanically treated cluster with the adsorption site of gas molecules, supported nanoclusters or even surface defects. The composition of the cluster still has to be chosen in such a way, that the local properties or adsorption behaviour is correctly reproduced. A direct adjacency of the cluster atoms and positive point charges results into an excessive polarization of the electron density in the cluster. Therefore, the positive point charges in the second boundary region, which is also treated quantum mechanically, are represented by effective core potentials (ECP), either as pseudo potentials (PP) or model potentials (MP). The third outer region contains the point charge field, which is sized to reproduce or at least converge towards the correct Madelung potential. Usually, their positions coincide with the lattice points of the crystal structure and the charges are chosen as their formal ones, at least for strongly ionic solids like MgO. Otherwise, it can become difficult for more covalent compounds like TiO_2 to determine an effective charge of the ions.

The electrostatic interaction between the quantum mechanically treated part (QM) and the periodic array of point charges (PC) is accounted by an additional expression for equation (2.21)

$$J^{\text{emb}} = \sum_{\mu\nu}^{\text{cluster}} P_{\mu\nu} F_{\mu\nu}^{\text{emb}} + \sum_{\mathbf{L}}^{\text{lattice}} \sum_{c}^{N_{\text{UC}}} \sum_{A}^{\text{cluster}} \frac{q_c Z_A}{|\mathbf{R}_A - \mathbf{R}_c + \mathbf{L}|} \quad , \tag{2.35}$$

where the second term describe the Coulomb interaction between the nuclei A of the QM cluster with its respective nuclear charge Z_A and each point charge q_c in the unit cell N_{UC} with position R_c for all points on the infinite Bravais lattice $\mathbf{L}$. The first term is an addition to the Coulomb repulsion J^{emb} (see, e.g., equation (2.24)) and adds the products of the density matrix $P_{\mu\nu}$ elements and the elements in $F_{\mu\nu}^{\text{emb}}$:

$$F_{\mu\nu}^{\text{emb}} = - \sum_{\mathbf{L}}^{\text{lattice}} \sum_{c}^{N_{\text{UC}}} q_l \int \int \frac{\eta_\mu(\vec{r} - \mathbf{R}_\mu)\eta_\nu(\vec{r} - \mathbf{R}_\nu)\delta(\vec{r}' - \mathbf{R}_c + \mathbf{L})}{|\vec{r} - \vec{r}'|} \, \mathrm{d}\vec{r}\mathrm{d}\vec{r}' \quad . \tag{2.36}$$

μ and ν are the indices of the basis function η_μ and η_ν at the position $\mathbf{R}_\mu$ and $\mathbf{R}_\nu$, which form, e.g., the Kohn-sham orbitals corresponding to the coefficients from the density matrix $P_{\mu\nu}$. The delta function δ provides the position of the point charges at $\mathbf{R}_l + \mathbf{L}$.

The periodic electrostatic embedded point charge method (PEECM) is an efficient method to calculate the infinite lattice sum in equation (2.35) and (2.36). It uses the periodic fast multipole method (PFMM)[127,128] , which bases on the fast multipole method (FMM) of Greengard and Rokhlin.[129,130] Initially, the PC region is divided into near-field (NF) and far-field parts (FF)[131]

$$F_{\mu\nu}^{\text{emb}} = F_{\mu\nu}^{\text{NF}} + F_{\mu\nu}^{\text{FF}} \tag{2.37}$$

$$J^{\text{emb}} = \sum_{\mu\nu}^{\text{cluster}} P_{\mu\nu} F_{\mu\nu}^{\text{emb}} + J_{\text{nuc}}^{\text{NF}} + J_{\text{nuc}}^{\text{FF}} \quad . \tag{2.38}$$

The defining radius around the QM cluster depends by the well-separateness criterion[127] and is chosen large enough to ensure a rapid convergence of the multipole approximation used for the FF interactions. The Coulomb interaction $J_{\text{nuc}}^{\text{NF}}$ and $F_{\mu\nu}^{\text{NF}}$ of the cluster with the point charges of the unit cells within the NF part are calculated analytically in accordance with equation (2.36) and (2.35), respectively. The remaining contributions of the interaction with the FF point charges are computed by using the multipole expansion[130,132,133] . The details for the computation of the FF contributions can be

found in reference [76].

PFMM evaluates the point charge lattice entirely in the real space and has the advantage of lower computational cost compared to the commonly used Ewald summation[134] , which sum over the contribution in the reciprocal space. Consequently, PFMM yields a different electrostatic potential but only by a constant shift affecting the absolute energies of the QM cluster and canceling out for relative energies.
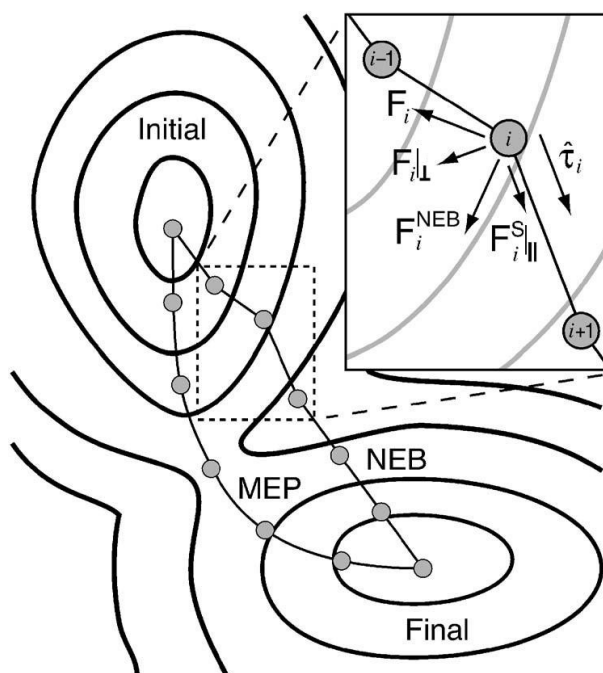
2.2.3 Nudged Elastic Band Method

[135–137]

Figure 2.1: Illustration of the NEB convergence procedure on a PES and the acting forces on the images of the elastic band using 6 images between the initial and final state. Image is taken from the Henkelman group, University of Texas at Austin[138] .

The nudged elastic band (NEB) method serves to determine the minimal energy path (MEP) between an initial and final structure on a PES connected by multiple structures also called images. The images are initially interpolated either linearly, by pair potentials[139] or involving intermediate structures to guide the search into a certain

direction. The purpose of the NEB method is to minimize the effective forces $\mathbf{F}_i^{\mathrm{NEB}}$ acting on the images labeled by the index i, which are connected by an elastic band as it is illustrated in figure 2.1. Each effective force $\mathbf{F}_i^{\mathrm{NEB}}$ sums up the spring force $\mathbf{F}_i^{\mathrm{S}}|_\parallel$ along the local and normalized tangent $\hat{\tau}_i$ and the true force $\mathbf{F}_i = -\nabla E(\mathbf{R}_i)$ perpendicular towards the tangent $\mathbf{F}_i|_\perp$. E corresponds to the energy of the system with the atomic coordinates $\mathbf{R}_i$ and the normalization of the tangent is labeled by the hat (ˆ).

$$\mathbf{F}_i^{\mathrm{NEB}} = \mathbf{F}_i^{\mathrm{s}}|_\parallel + \mathbf{F}_i|_\perp \tag{2.39}$$

The perpendicular component of the force is simply computed by subtracting out the parallel projection of the true force

$$\mathbf{F}_i|_\perp = \mathbf{F}_i - \mathbf{F}_i\hat{\tau}_i \quad , \tag{2.40}$$

and the spring force between adjacent images is a function of the spring constant k

$$\mathbf{F}_i^{\mathrm{S}}|_\parallel = k \left(|\mathbf{R}_{i+1} - \mathbf{R}_i| - |\mathbf{R}_i - \mathbf{R}_{i-1}| \right) \hat{\tau}_i \quad . \tag{2.41}$$

Originally, the local tangent was estimated from both adjacent images[135] , but an improvement in the MEP was observed, when the local tangent $\hat{\tau}_i$ depends only on the adjacent image $i' = i \pm 1$ with the higher energy and the image itself[136]

$$\hat{\tau}_i = \begin{cases} \hat{\tau}_i^+ & \text{if } E(\mathbf{R}_{i+1}) > E(\mathbf{R}_i) > E(\mathbf{R}_{i-1}) \\ \hat{\tau}_i^- & \text{if } E(\mathbf{R}_{i+1}) < E(\mathbf{R}_i) < E(\mathbf{R}_{i-1}) \end{cases} \tag{2.42}$$

with

$$\hat{\tau}_i^+ = \mathbf{R}_{i+1} - \mathbf{R}_i \tag{2.43}$$

$$\hat{\tau}_i^- = \mathbf{R}_i - \mathbf{R}_{i-1} \quad . \tag{2.44}$$

If an image lies close to the local minimum or maximum and both adjacent images are respectively higher or lower in energy, the tangent is computed by the weighted average of the vectors towards the two neighboring images. The modification guarantees a smooth switch between the two tangents $\hat{\tau}_i^+$ and $\hat{\tau}_i^-$, which, otherwise, can drastically change

the convergence direction. The estimate of the tangent becomes

$$\tau_i = \begin{cases} \hat{\tau}_i^+ \Delta E_i^{\max} + \hat{\tau}_i^- \Delta E_i^{\min} & \text{if } E_{i+1} > E_{i-1} \\ \hat{\tau}_i^+ \Delta E_i^{\min} + \hat{\tau}_i^- \Delta E_i^{\max} & \text{if } E_{i+1} < E_{i-1} \end{cases} \tag{2.45}$$

with

$$\Delta E_i^{\max} = \max\left(\left|E_{i+1} - E_i\right|, \left|E_{i-1} - E_i\right|\right) \tag{2.46}$$

$$\Delta E_i^{\min} = \min\left(\left|E_{i+1} - E_i\right|, \left|E_{i-1} - E_i\right|\right) \quad . \tag{2.47}$$

Finally, the tangent vector in equation (2.45) needs to be renormalized by $\hat{\tau}_i = \tau_i / \left|\tau_i\right|$. The elastic band converges towards the MEP by minimizing the effective force $\mathbf{F}_i^{\text{NEB}}$ of each image using an optimization algorithm such as, for instance, the projected velocity Verlet algorithm[135] or the fast inertial relaxation engine (FIRE) algorithm.[140] A drawback of that procedure is that none of the images could even land close to the saddle point. The transition state energy must be estimated by interpolation *a posteriori*, which may yield poor estimates of the activation barrier. The climbing image scheme (CI-NEB)[136] tackles the problem by repeatedly activating within the regular NEB procedure. When activated, the force effecting the image with the highest energy $\mathbf{F}_{i_{\max}}^{\text{CI}}$ changes to

$$\begin{aligned} \mathbf{F}_{i_{\max}}^{\text{CI}} &= \mathbf{F}_{i_{\max}} - 2\mathbf{F}_{i_{\max}}|_{\parallel} \\ &= \mathbf{F}_{i_{\max}} + 2\nabla E(\mathbf{R}_{i_{\max}}) \cdot \hat{\tau}_{i_{\max}} \hat{\tau}_{i_{\max}} \\ &= \mathbf{F}_{i_{\max}}|_{\perp} - \mathbf{F}_{i_{\max}}|_{\parallel} \quad . \end{aligned} \tag{2.48}$$

Qualitatively, the image moves up the PES along the elastic band while relaxing perpendicular to the band without considering the spring force during that scheme. As long as the climbing image NEB method converges, the climbing image will also converge towards the saddle point. An implementation of the NEB method can be found in the *ATOMIC SIMULATION ENVIRONMENT*[141] (ASE), which provides Python modules compatible with a large variety of common quantum chemical programs.

2.2.4 Energy Decomposition Analysis

[142, 143]

Interaction energies are an important quantity to determine physical and chemical properties of molecular and intermolecular systems. They can be simply computed as a difference between the total energy of the supermolecule and the total energies of the monomers or fragments deriving from size-consistent methods. Further insights in their contributions can help to understand the consequences of chemical modifications on the interaction strength. Early applications in describing the interaction between atoms goes way back to W. Heitler and F. London in 1927,[144] but first the energy decomposition analysis (EDA), developed by K. Morokuma and K. Kitaura[145,146] as well as T. Ziegler and A. Rauk[147] in the 1970th, provides a powerful method to bridge the gap between quantum mechanics and a conceptually simple interpretation of chemical bonds.[143]

Many variants of the energy decomposition analysis have been developed, which can be applied on *ab initio* Hartree-Fock, MP2, and DFT methods. In **paper B**, the decomposition procedure of P. Su and H. Li[142] is used, which is implemented in the *TURBOMOLE*[148] program package. The total interaction energy ΔE_{int} is separated into various terms such as the electrostatic ΔE_{elstat}, exchange ΔE_{ex}, repulsion ΔE_{rep} and polarization energies ΔE_{pol}. The latter is often described as orbital relaxation term and the exchange and repulsion contributions are both together labeled as Pauli repulsion. In the following we briefly describe the procedure for Kohn-Sham DFT methods, where the interaction energy $\Delta E_{\text{int}}^{\text{KS}}$ is additionally complemented by a dispersion contribution ΔE_{disp}:

$$\Delta E_{\text{int}}^{\text{KS}} = \Delta E_{\text{elstat}} + \Delta E_{\text{ex}} + \Delta E_{\text{rep}} + \Delta E_{\text{pol}} + \Delta E_{\text{disp}} \quad . \tag{2.49}$$

Although the procedure is formulated for open shell systems, we will focus on a qualitative description of electronic closed shell systems are considered for the supermolecule $\mathcal{S}$ and its monomers or fragments $\mathcal{M}$. The Kohn-Sham energy E_X^{KS} of and arbitrary system $\mathcal{A}$ can be written as

$$E_A^{\text{KS}} = \sum_{i \in \mathcal{A}}^{n_{\mathcal{A}}} h_i^{\mathcal{A}} + \frac{1}{2} \sum_{i \in \mathcal{A}}^{n_{\mathcal{A}}} \sum_{j \in \mathcal{A}}^{n_{\mathcal{A}}} \langle \varphi_i \varphi_i | \varphi_j \varphi_j \rangle + E_X \left[\rho_{\mathcal{A}} \right] + E_C \left[\rho_{\mathcal{A}} \right] + V_{\text{nuc-nuc}}^{\mathcal{A}} \quad , \tag{2.50}$$

where $h_i^{\mathcal{A}}$ are the one-electron integrals containing the electronic kinetic energy and the

Coulomb potential for the nuclear configuration of an arbitrary system $\mathcal{A}$, respectively defined in equation (2.22) and (2.23). The sum goes over all $n_\mathcal{A}$ Kohn-Sham orbitals and respective one-electron densities, which are energetically optimized to the respective system $i, j \in \mathcal{A}$. The second term describes the Coulomb repulsion of equation (2.24) and can alternatively expressed as

$$
\begin{aligned}
\sum_{i \in \mathcal{A}}^{n_\mathcal{A}} \sum_{j \in \mathcal{A}}^{n_\mathcal{A}} \langle \varphi_i \varphi_i | \varphi_j \varphi_j \rangle &= \sum_{i \in \mathcal{A}}^{n_\mathcal{A}} \sum_{j \in \mathcal{A}}^{n_\mathcal{A}} \int \int \varphi_i(\vec{r}) \varphi_i(\vec{r}) \frac{1}{|\vec{r} - \vec{r}'|} \varphi_j(\vec{r}') \varphi_j(\vec{r}') \mathrm{d}\vec{r} \mathrm{d}\vec{r}' \\
&= \int \int \frac{1}{|\vec{r} - \vec{r}'|} \rho_\mathcal{A}(\vec{r}) \rho_\mathcal{A}(\vec{r}') \mathrm{d}\vec{r} \mathrm{d}\vec{r}' \quad ,
\end{aligned}
\tag{2.51}
$$

where $\rho_\mathcal{A}$ is the energetically optimized total electron density of system $\mathcal{A}$. The elements $(\mathbf{S}_\mathcal{A})_{ij}$ of the overlap matrix $\mathbf{S}_\mathcal{A}$ for the Kohn-Sham orbitals of system $\mathcal{A}$ are defined as

$$
(\mathbf{S}_\mathcal{A})_{ij} = \int \varphi_i(\vec{r}) \varphi_j(\vec{r}) \mathrm{d}\vec{r} \quad ,
\tag{2.52}
$$

and result into an identity matrix for orthonormalized Kohn-Sham orbitals φ_i. E_X and E_C are the exchange and correlation functionals depending on the electron density $\rho_\mathcal{A}$

$$
\rho_\mathcal{A} = \sum_{i \in \mathcal{A}} \int \varphi_i(\vec{r}) \varphi_i(\vec{r}) \mathrm{d}\vec{r} \quad ,
\tag{2.53}
$$

and $V_{\mathrm{nuc-nuc}}^{\mathcal{A}}$ is the nuclear repulsion of the nuclear configuration in system $\mathcal{A}$. For the sake of further simplicity, the dependence of the Kohn-Sham orbitals and the electron density on the electron and nuclear coordinates will be further omitted.

For an arbitrary number of fragments, the Kohn-Sham interaction energy between the supermolecule $\mathcal{S}$ and its monomers $\mathcal{M}$ is defined as

$$
\Delta E_{\mathrm{int}}^{\mathrm{KS}} = E_\mathcal{S}^{\mathrm{KS}} - \sum_\mathcal{M} E_\mathcal{M}^{\mathrm{KS}} \quad .
\tag{2.54}
$$

In the initial step, the quasi-classical Coulomb interaction between the frozen electron densities of the fragments at the equilibrium position of the supermolecule defines the

electrostatic contribution ΔE_{elstat} with

$$
\begin{aligned}
\Delta E_{\text{elstat}} = \sum_{i \in \mathcal{M}}^{n_{\mathcal{S}}} h_i^{\mathcal{S}} &+ \frac{1}{2} \sum_{i \in \mathcal{M}}^{n_{\mathcal{S}}} \sum_{j \in \mathcal{M}}^{n_{\mathcal{S}}} \langle \varphi_i \varphi_i | \varphi_j \varphi_j \rangle + V_{\text{nuc-nuc}}^{\mathcal{S}} \\
&- \sum_{\mathcal{M}} \left[\sum_{i \in \mathcal{M}}^{n_{\mathcal{M}}} h_i^{\mathcal{M}} + \frac{1}{2} \sum_{i \in \mathcal{M}}^{n_{\mathcal{M}}} \sum_{j \in \mathcal{M}}^{n_{\mathcal{M}}} \langle \varphi_i \varphi_i | \varphi_j \varphi_j \rangle + V_{\text{nuc-nuc}}^{\mathcal{M}} \right] \quad .
\end{aligned}
\tag{2.55}
$$

The first three terms contain the kinetic energy of the electrons and the respective Coulomb interactions between the nuclei of the supermolecule $\mathcal{S}$ and the $n_{\mathcal{S}}$ Kohn-Sham orbitals, which are optimized to the fragments $i, j \in \mathcal{M}$, as for a non-interacting system. The second part describe the same information but only within the fragments themselves. The Kohn-Sham exchange interaction ΔE_{ex} is defined as

$$
\Delta E_{\text{ex}} = E_X \left[\sum_{\mathcal{M}} \rho_{\mathcal{M}} \right] - \sum_{\mathcal{M}} E_X \left[\rho_{\mathcal{M}} \right]
\tag{2.56}
$$

and is generally not zero since the exchange functional depends non-linearly on the electron density. The Kohn-Sham repulsion energy ΔE_{rep} can be obtained by the difference of the following auxiliary energy expressions

$$
E_{\mathcal{S}}^{(1)} = \sum_{i \in \mathcal{M}}^{n_{\mathcal{S}}} h_i^{\mathcal{S}} + \frac{1}{2} \sum_{i \in \mathcal{M}}^{n_{\mathcal{S}}} \sum_{j \in \mathcal{M}}^{n_{\mathcal{S}}} \langle \varphi_i \varphi_i | \varphi_j \varphi_j \rangle + E_X \left[\sum_{\mathcal{M}} \rho_{\mathcal{M}} \right] + \sum_{\mathcal{M}} E_C \left[\rho_{\mathcal{M}} \right] + V_{\text{nuc-nuc}}^{\mathcal{S}}
\tag{2.57}
$$

and

$$
\begin{aligned}
E_{\mathcal{S}}^{(2)} = \sum_{i \in \mathcal{M}}^{n_{\mathcal{S}}} \sum_{j \in \mathcal{M}}^{n_{\mathcal{S}}} h_{ij}^{\mathcal{S}} \left(\mathbf{S}^{-1} \right)_{ij} &+ \frac{1}{2} \sum_{i \in \mathcal{M}}^{n_{\mathcal{S}}} \sum_{j \in \mathcal{M}}^{n_{\mathcal{S}}} \sum_{k \in \mathcal{M}}^{n_{\mathcal{S}}} \sum_{l \in \mathcal{M}}^{n_{\mathcal{S}}} \langle \varphi_i \varphi_j | \varphi_k \varphi_l \rangle \times \left(\mathbf{S}^{-1} \right)_{ij} \left(\mathbf{S}^{-1} \right)_{kl} \\
&+ E_X \left[\rho_{\mathcal{S}}^* \right] + \sum_{\mathcal{M}} E_C \left[\rho_{\mathcal{M}} \right] + V_{\text{nuc-nuc}}^{\mathcal{S}} \quad .
\end{aligned}
\tag{2.58}
$$

Even if the Kohn-Sham orbitals $i, j, k, l \in \mathcal{M}$ are orthonormal to each other within the fragments, this is not necessarily true for the orbitals between the fragments. Thus, the overlap matrix $\mathbf{S}$ and its inverse $\mathbf{S}^{-1}$ are no identity matrices and the electron density $\rho_{\mathcal{S}}^*$ arises from the orthonormalized Kohn-Sham orbitals of the fragments by:

$$
\rho_{\mathcal{S}}^* = \sum_{i \in \mathcal{M}}^{n_{\mathcal{S}}} \sum_{j \in \mathcal{M}}^{n_{\mathcal{S}}} \varphi_i \varphi_j \left(\mathbf{S}^{-1} \right)_{ij} \quad .
\tag{2.59}
$$

Finally, the contribution of the repulsion energy ΔE_{rep} to the interaction energy is computed by

$$\Delta E_{\text{rep}} = E_{\mathcal{S}}^{(2)} - E_{\mathcal{S}}^{(1)} \quad . \tag{2.60}$$

While the exchange energy is negative, the positive repulsion energy dominates and together they can be interpreted as the energy necessary to regain the antisymmetry or Pauli principle, when the fragments with frozen Kohn-Sham orbitals form the supermolecule.

The polarization energy ΔE_{pol} can be obtained by the energy expression in equation (2.58) using the Kohn-Sham orbitals of the fragments and the equivalent expression using the optimized Kohn-Sham orbitals of the supermolecule $i, j \in \mathcal{S}$

$$E_{\mathcal{S}}^{(3)} = \sum_{i \in \mathcal{S}}^{n_{\mathcal{S}}} h_i^{\mathcal{S}} + \frac{1}{2} \sum_{i \in \mathcal{S}}^{n_{\mathcal{S}}} \sum_{j \in \mathcal{S}}^{n_{\mathcal{S}}} \langle \varphi_i \varphi_i | \varphi_j \varphi_j \rangle + E_X [\rho_{\mathcal{S}}] + \sum_{\mathcal{M}} E_C [\rho_{\mathcal{M}}] + V_{\text{nuc-nuc}}^{\mathcal{S}} \quad , \tag{2.61}$$

where the overlap matrix and its inverse become again the identity matrix. The polarization contribution is now computed by

$$\Delta E_{\text{pol}} = E_{\mathcal{S}}^{(3)} - E_{\mathcal{S}}^{(2)} \tag{2.62}$$

and is always negative. It shows the energy gain by the energetically optimization of the Kohn-Sham orbitals starting from the combination within the respective fragments, as the alternative term "orbital relaxation energy" proclaims. The remaining energy difference between $E_{\mathcal{S}}^{(3)}$ and the total energy of the supermolecule $E_{\mathcal{S}}^{\text{KS}}$ defines the dispersion energy ΔE_{disp}

$$\Delta E_{\text{disp}} = E_{\mathcal{S}}^{\text{KS}} - E_{\mathcal{S}}^{(3)} = E_C [\rho_{\mathcal{S}}] - \sum_{\mathcal{M}} E_C [\rho_{\mathcal{M}}] \quad . \tag{2.63}$$

As mentioned above, the evaluation of the interaction contribution can give insight into the nature of the chemical bond or explains the difference in interaction strength between similar bond types. For example, the ratio of the electrostatic and the polarization contribution is a useful quantity to distinguish the bonding character as covalent or more ionic.

2.3 Gas-Surface Dynamics

The previous sections capture the solution of the electronic Schrödinger equation for a fixed nuclear configuration and for surface systems in particular. It gives the possibility to determine potential energy minimum structures by scanning over different nuclear configurations and to compute a minimum energy path connecting two nuclear configurations or potential minima. Nonetheless, static information are not necessarily sufficient to understand surface processes, which can only be provided by performing dynamical simulations. The potential energy landscape for the dynamics can be either provided by *ab initio* calculation or a force field fitted to a set of reference points. While the first way is computationally rather expensive but quite accurate within the limit of the applied electronic structure method, the latter one can be extremely fast. However, an accurate reproduction of reference potential data is not a trivial task and depends on the flexibility of the force field and its proper parametrization. Additionally, the comparison of classical dynamic simulations to experimental results also requires an accurate mapping of the initial quantum states into a distribution of classical trajectories and its evaluation back into final quantum states after the simulation reaches the end.

2.3.1 Molecular Dynamics Simulation - Quasi-Classical Trajectories

[149–151]

The trajectories of atoms in a potential field $V(\mathbf{R})$ are determined by the solution of Newton's equation of motion

$$M_A \frac{\partial^2}{\partial t^2} \vec{R}_A = -\frac{\partial}{\partial \vec{R}_A} V(\mathbf{R}) \tag{2.64}$$

for each atom A individually. M_A and $\vec{R}_A$ are the mass and position of atom A and the potential $V(\mathbf{R})$ depends on the positions of all atoms $\mathbf{R}$. The potential energy surface, or PES, is equivalent to $\epsilon_\lambda(\mathbf{R})$ of equation (2.7), usually representing the electronic ground state energy of the quantum system.

Newton's equation of motion can be numerical solved by integration schemes like Runge-Kutta or the rather simple Verlet integration scheme.[152] The Verlet algorithm derives

the new position of an atom after a chosen time step Δt from the Taylor expansion of the trajectory $\vec{R}_A(t)$

$$
\begin{aligned}
\vec{R}_A(t_0 + \Delta t) &= \vec{R}_A(t_0) + \Delta t \left.\frac{d\vec{R}_A}{dt}\right|_{t_0} + \frac{\Delta t^2}{2}\left.\frac{d^2\vec{R}_A}{dt^2}\right|_{t_0} + \frac{\Delta t^3}{6}\left.\frac{d^3\vec{R}_A}{dt^3}\right|_{t_0} + \dots \\
&= \vec{R}_A(t_0) + \Delta t\, \vec{v}_A(t_0) + \frac{\Delta t^2}{2}\frac{\vec{F}_A(t_0)}{M_A} + \frac{\Delta t^3}{6}\left.\frac{d^3\vec{R}_A}{dt^3}\right|_{t_0} + \dots \quad ,
\end{aligned}
\tag{2.65}
$$

where $\vec{v}_A$ is the velocity of atom A and $\vec{F}_A$ is the force acting on it. Analogously, the position can be determined at a previous time with

$$
\vec{R}_A(t_0 - \Delta t) = \vec{R}_A(t_0) - \Delta t\, \vec{v}_A(t_0) + \frac{\Delta t^2}{2}\frac{\vec{F}_A(t_0)}{M_A} - \frac{\Delta t^3}{6}\left.\frac{d^3\vec{R}_A}{dt^3}\right|_{t_0} + \dots \quad .
\tag{2.66}
$$

The addition of equation (2.65) and (2.66) and the truncation after the term of third order yields

$$
\vec{R}_A(t_0 + \Delta t) = 2\vec{R}_A(t_0) - \vec{R}_A(t_0 - \Delta t) + \Delta t^2 \frac{\vec{F}_A(t_0)}{M_A} + \mathcal{O}(\Delta t^4) \quad .
\tag{2.67}
$$

The reliability of the numerical integration can be easily monitored by the deviation of the total energy, which should be constant along the trajectory. While the potential energy is a function of the actual nuclear configuration $\mathbf{R}$, the kinetic energy is determined by the velocity, which cancels out in equation (2.67). Anyways, the velocity of the atoms can be estimated by

$$
\vec{v}_A(t_0) = \frac{\vec{R}_A(t_0 + \Delta t) - \vec{R}_A(t_0 - \Delta t)}{2\Delta t} + \mathcal{O}(\Delta t^2) \quad .
\tag{2.68}
$$

The low accuracy and the use of the time step prior to the actual one is avoided in the related velocity Verlet algorithm,[153] where the positions and velocities of the atoms can be computed by

$$
\vec{R}_A(t_0 + \Delta t) = \vec{R}_A(t_0) + \Delta t \vec{v}_A(t_0) + \frac{\Delta t^2}{2}\frac{\vec{F}_A(t_0)}{M_A}
\tag{2.69}
$$

and

$$
\vec{v}_A(t_0 + \Delta t) = \vec{v}_A(t_0) + \Delta t \frac{\vec{F}_A(t_0 + \Delta t) + \vec{F}_A(t_0)}{2M_A} \quad .
\tag{2.70}
$$

The length of the time step Δt is a compromise between the numerical error and the

computational costs. A shorter time step means more accuracy but also more iterations for a given time interval. The larger the time span the larger is the error, which might accumulate.

The quasi-classical MD approach is a frequently used method to simulate atom level dynamics and mechanisms of chemical reactions between gas molecules[154] among themselves or gas molecules with solid surfaces.[93] It applies quasi-classical initial conditions on the reactants for the trajectories in a way, that the internal energy corresponds to a specific energy eigenvalue of a defined ro-vibrational quantum state. The initial point in the phase-space is randomly chosen, while conserving the internal energy, and the trajectories are propagated with standard classical mechanics. In comparison, initial classical quantum states do not conserve the exact ro-vibrational eigenvalue but are classically distributed over the energy to represent its uncertainty as well.

QCT method becomes more reliable with a larger number of calculated trajectories. The Ehrenfest theorem[155] states, that the quantum mechanical expectation values of the position $\langle \mathbf{x} \rangle$ and momentum $\langle \mathbf{p} \rangle$ satisfy the classical equation of motion for the averaged potential $\langle V(\mathbf{x}) \rangle$. The classical mechanics however are directed by the potential $V(\langle \mathbf{x} \rangle)$ at the averaged position, which makes it more valid for a small spread of the nuclear wave function in $\langle \mathbf{x} \rangle$. That becomes the case for systems with heavier atoms and higher energies in each degree of freedom in accordance to the de Broglie wavelength, but only as long as the Born-Oppenheimer approximation is still valid. Furthermore, classical mechanics lacks in the description of classical forbidden paths like tunneling effects. This deficiency has a larger impact, if the total energy of the reactants becomes close to the reaction barriers. Thus, QCT methods will probably misestimate small reaction or transition probabilities.[149]

2.3.2 Force Field Parameterization

[151, 156]

Molecular dynamics simulation need a continuous description of the PES and its gradients for a particular nuclear configuration at any time. The evaluation of the energy and gradients with *ab initio* methods is still so expansive, that the simulation of a sufficient

number of trajectories for a statistical evaluation is computationally heavily demanding. Analytical representations of a potential energy surface, however, can provide the potential values and gradients extremely fast, especially by using an analytical expression for the evaluation of the gradient, as well. In computational chemistry, such analytical forms of the potential are called force fields (FF) and bases mostly on atom-pair interactions, which prohibit them from describing bond breaking and formation. Bond order potentials[157,158] (REBO-FF) or reactive force fields[159] (ReaxFF) are ongoing developments for describing chemical reactions. They commonly include the chemical environment like distances and angles to surrounding atoms to evaluate the bond strength between two atoms. For gas-surface systems, especially with diatomic gas molecules, the potential can be alternatively described as a function of the angular orientation, the bond distance and the position of the COM in relation to the surface.[160,161] If the number of degrees of freedom (DoF) increases, the analytical form of force fields can become very complicated. Optimal force fields should provide a huge flexibility to accurately reproduce the *ab initio* reference data set, but should preferably use only a limited number of parameters to keep controllability. Further, they should ensure a reliable extrapolation to nuclear configuration, which are not covered by the reference data. Alternatively, neural networks can principally fit any real-valued, continuous function to any desired accuracy and got a lot of attention by researchers in recent years[162,163]. However, since the form of neural networks has no physical meaning, the extrapolation of the potential to nuclear configuration beyond the reference data set is highly unreliable.

The work in **paper C** makes use of the full-dimensional REBO-FF by H. F. Busnengo and coworkers[156] to compute the potential for gas-surface systems. Here, the potential V is computed as a sum of atom-pair contributions E_r and non-bonding contributions E_{nb}

$$V = E_r + E_{nb} \quad . \tag{2.71}$$

The atom-pair interactions are basically a sum of pair potentials V^{rep} and V^{att}, where the attractive pair potential is weighted by a symmetrised bond order term $\bar{b}_{ij}^{\alpha\beta}$ that describes the effect of the chemical environment around the atom pair i and j of species α and β, respectively.

$$E_r = \sum_{\alpha=1}^{n} \sum_{\beta=1,\alpha>\beta}^{n} \sum_{i=1}^{N_\alpha} \sum_{\substack{j=1,(j>i, \\ if \ \alpha=\beta)}}^{N_\beta} \left[V_{\alpha\beta}^{rep}\left(r_{ij}^{\alpha\beta}\right) - \bar{b}_{ij}^{\alpha\beta} V_{\alpha\beta}^{att}\left(r_{ij}^{\alpha\beta}\right) \right] \tag{2.72}$$

In general, the Greek letters (α, β, γ) denote the atom species, n is the total number of species and N corresponds to the number of atoms per species. $r_{ij}^{\alpha\beta}$ is the distance between atom i of species α and atom j of species β.

$$V_{\alpha\beta}^{rep} = A_{\alpha\beta} f_{\alpha\beta}\left(r_{ij}^{\alpha\beta}\right)\left(1 + \frac{B_{\alpha\beta}}{r_{ij}^{\alpha\beta}}\right)\exp\left(-\sigma_{\alpha\beta} r_{ij}^{\alpha\beta}\right) \tag{2.73}$$

$$V_{\alpha\beta}^{att} = C_{\alpha\beta} f_{\alpha\beta}\left(r_{ij}^{\alpha\beta}\right)\exp\left(-\omega_{\alpha\beta} r_{ij}^{\alpha\beta}\right) \tag{2.74}$$

$A_{\alpha\beta}$, $B_{\alpha\beta}$, $C_{\alpha\beta}$, $\sigma_{\alpha\beta}$ and $\omega_{\alpha\beta}$ are the fit parameters describing the two-body interaction between atoms of species α and β. The interaction is limited to a bond distance up to certain cutoff values $r_{s1}^{\alpha\beta}$ and $r_{s2}^{\alpha\beta}$ by the cutoff function $f_{\alpha\beta}\left(r_{ij}^{\alpha\beta}\right)$. The cutoff function smoothly disables the interaction energy between the lower limit $r_{s1}^{\alpha\beta}$ and the upper limit $r_{s2}^{\alpha\beta}$.

$$f_{\alpha\beta}\left(r_{ij}^{\alpha\beta}\right) = \begin{cases} 1 & r_{ij}^{\alpha\beta} \leq r_{s1}^{\alpha\beta} \\ \frac{1}{2}\left(1 + \cos\left[\pi\left(r_{ij}^{\alpha\beta} - r_{s1}^{\alpha\beta}\right)/\left(r_{s2}^{\alpha\beta} - r_{s1}^{\alpha\beta}\right)\right]\right) & r_{s1}^{\alpha\beta} < r_{ij}^{\alpha\beta} \leq r_{s2}^{\alpha\beta} \\ 0 & r_{ij}^{\alpha\beta} > r_{s1}^{\alpha\beta} \end{cases} \tag{2.75}$$

The symmetrised bond order term $\bar{b}_{ij}^{\alpha\beta}$ evaluates the influence of each surrounding atom within the cutoff-range of the attractive bond interaction as a function of the distance to both atoms ($r_{ik}^{\alpha\gamma}$, $r_{jk}^{\beta\gamma}$) and the respective angle (θ_{ijk}, θ_{jik}). The arithmetic mean of the single bond order terms $b_{ij}^{\alpha\beta}$ and $b_{ji}^{\beta\alpha}$ forms $\bar{b}_{ij}^{\alpha\beta}$

$$\bar{b}_{ij}^{\alpha\beta} = \frac{1}{2}\left(b_{ij}^{\alpha\beta} + b_{ji}^{\beta\alpha}\right) \quad, \tag{2.76}$$

with

$$b_{ij}^{\alpha\beta} = \left(1 + \sum_{\gamma=1}^{n} \sum_{\substack{k=1 \\ (k\neq i,\ if\ \gamma=\alpha; \\ k\neq j,\ if\ \gamma=\beta)}}^{N_\gamma} f_{\alpha\beta}\left(r_{ik}^{\alpha\gamma}\right) g_{\alpha\beta\gamma}\left(\cos\theta_{ijk}\right)\exp\left(-\lambda_{\alpha\beta\gamma}\left(r_{ik}^{\alpha\gamma} - r_{ij}^{\alpha\beta}\right)\right)\right)^{-\frac{1}{2}} . \tag{2.77}$$

The angle dependency $g_{\alpha\beta\gamma}\left(\cos\theta_{ijk}\right)$ of the bond order terms can be described by any suitable function like a polynomial expression or a linear combination of Legendre polynomials. The long-range interaction between gas molecules and the surface is implied

by the non-bonding contribution E_{nb}, which is independent of the atomic species and only depends on the height z of the atoms to the surface.

$$E_{nb}(z) = f_{nb}(z)\left(c_0 - \frac{c_1}{z^2}\right) \tag{2.78}$$

The non-binding potential is defined by the parameter c_0 and c_1 and becomes smoothly activated by the non-bonding cutoff function $f_{nb}(z)$, the complementary version of the cutoff function for the atom-pair potential in equation (2.75).

$$f_{nb}(z) = \begin{cases} 0 & z \leq Z_1 \\ \frac{1}{2}\left(1 - \cos\left[\pi\left(z - Z_1\right)/\left(Z_2 - Z_1\right)\right]\right) & Z_1 < z \leq Z_2 \\ 1 & z > Z_2 \end{cases} \tag{2.79}$$

Usually, the parameters are fitted by the method of least squares, where they are varied to minimise the deviation d^2 between the potential values provided by the force field and the reference data. It is quantified by

$$d^2 = \sum_{m=1}^{N_{\text{data}}} w_m (V_m^{\text{ref}} - V_m^{\text{FF}})^2 \quad , \tag{2.80}$$

where N_{data} denotes to the size of the reference data set containing the reference potential values V_m^{ref}. V_m^{FF} are the potential values of the force field and w_m is a weighting factor that allows to attribute more importance to reference data within the lower energy region. Instead of potential values, the deviation can be alternatively computed using the components of a force. The accuracy of the force field is finally measured by the root mean square deviation ΔV defined by

$$\Delta V = \sqrt{\frac{d^2}{N_{\text{data}}}} \quad . \tag{2.81}$$

It has proved convenient for a computational purposes to first determine parameters for smaller system and adopt them as either initial values or fixed values for the parameterization of the force field towards larger systems.

2.3.3 Initial conditions

[93, 150, 164]

The quasi-classical distribution of initial states over a large number of trajectories is important to allow direct comparison between molecular beam experiments and respective quasi-classical or Monte-Carlo MD simulations. Experiments provide molecular beam parameters that allow reconstructing the distribution of the initial velocity and the ro-vibrational distribution of the beam molecules. In the following, only the case of diatomic beam molecules scattering on a surface is treated. The quasi-classical distribution of the initial states for poly-atomic molecules can be found elsewhere (see, e.g., reference [150, 164]).

Initially, the energy eigenvalues of the ro-vibrational states $E_{\nu,j}$ can be, once, calculated analytically by using the harmonic approximation or Morse potential for the elongation of the diatomic bond length around its equilibrium distance and the quantum mechanical solution of a rigid rotator for the rotation of the molecule. Alternatively, the eigenvalues can be numerically determined by discrete variable representation (DVR) methods, for instance, to solve the TISE for the diatomic system with the Hamiltonian

$$\hat{H}_j = -\frac{1}{2\mu}\frac{\partial^2}{\partial r^2} + V_{\text{eff}}^j(r) \quad , \tag{2.82}$$

where r is the bond distance and μ the respective reduced mass of the molecule. The effective potential $V_{\text{eff}}^j(r)$

$$V_{\text{eff}}^j(r) = V_{\text{gas}}(r) + \frac{1}{2\mu r^2}j(j+1) \tag{2.83}$$

contains the gas-phase potential and the rotational energy for a given rotational quantum number j, which both depend on the bond distance r. The population distribution of the ro-vibrational state in molecular beam experiments depends on the nozzle temperature T_n and can be either taken from experimentally determined population distributions or determined accordingly to the Boltzmann probability $f_{\nu,j}(T_n)$

$$f_{\nu,j}(T_n) = (2j+1)\frac{\mathrm{e}^{-(E_{\nu,j}-E_{0,0})/(k_B T_n)}}{Z(T_n)} \quad , \tag{2.84}$$

where $Z(T_n)$ is the partition function and k_B is the Boltzmann constant, which has the value of 1.0 in atomic units by definition. The effective temperature of the molecular beam might be also not equally distributed over the vibrational and rotational states in dependence of the molecular beam technique. Thus, the exponential function of the distribution function (2.84) will split into a product of two exponential functions for both type of degrees of freedom, which will also affect the partition function. The initial velocity can be easily translated to an initial momentum of the centre of mass, where the direction depends on the incident angle of the molecular beam. The distribution and the width of the initial velocity strongly depend on the beam technique and must be provided by the experiment.

The initial bond length, orientation and respective momentum are randomly sampled for each trajectory in accordance to the quantum numbers. A quantum mechanical sampling of the phase-space for the bond elongation can be provided by the Wigner quasi-probability.[165] In a classical sampling, the phase-space is chosen by energy conversation. Within the harmonic approximation, each point in the phase-space corresponds to the respective energy of the vibrational state ν and has the same weight, which is not necessarily the case for arbitrary diatomic potentials. Alternatively, the initial elongation and respective momentum can be determined by choosing a random point of time $t = [0, t_f]$ within one full vibrational period t_f of the diatomic molecule, that moves on the potential $V_{\mathrm{eff}}^j(r)$ with the respective ro-vibrational energy $E_{\nu,j}$.

The initial orientation of the rotational angular momentum vector $\mathbf{L}$ for the diatomic molecule perpendicular to the bond axis is rather simple. For the rotational excited states $j > 0$, the angle β between $\mathbf{L}$ and the system-specific symmetry axis z is given by the relation

$$\cos(\beta) = \frac{m_j}{\sqrt{j(j+1)}}, \tag{2.85}$$

where m_j is the component of the angular momentum along the z axis. For the scattering of a molecule on a surface, the z axis point along the same direction as the surface normal. The azimuthal component $\alpha \in [0, 2\pi]$ of $\mathbf{L}$ and the angular orientation $\gamma \in [0, 2\pi]$ of the molecule in the plane perpendicular to $\mathbf{L}$ is randomly chosen. A coordinate transformation maps the configuration $\{\alpha, \beta, \gamma\}$ onto the corresponding $\{\theta, \phi\}$, where θ describes the polar angle between the bond axis of the diatomic molecule and the surface normal along z, ϕ represents the respective azimuthal angle perpendicular to z. If the gas molecule is in the rotational ground state $j = 0$ with no initial rotational momentum, the angular

probability distribution in θ simplifies to a $\sin(\theta)$ distribution and $\phi \in [0, 2\pi]$ is randomly chosen. The initial total angular momentum $\mathbf{L}$ is given by

$$\mathbf{L} = \sqrt{j(j+1)} \quad , \tag{2.86}$$

which can be decomposed for the case of a linear molecule to

$$\mathrm{L}_\theta = \sqrt{j(j+1) - \frac{m_j}{\sin^2(\theta)}} \tag{2.87}$$

and

$$|\mathrm{L}_\phi| = |\mathrm{L}_\mathrm{z}| = m_j \quad . \tag{2.88}$$

For polyatomic molecules, except spherical ones, the rotational eigenstates must not longer be degenerate in m_j. Thus, the ro-vibrational eigenvalues $E_{\nu,j}$ becomes a function of m_j as well. A detailed description of this case is beyond the scope of the present work.

2.3.4 Evaluation and Binning

[154, 166]

Once the propagation of a trajectory is completed and the outcome is identified, it is from interest to extract the relative translational energy between the reactants, their respective internal energies and the scattering angle between the incoming and outgoing velocity or momentum vectors.

The determination of the final translation energies in gas-surface simulations is straight forward without regarding their relative movement to each another, due to the usual immense mass difference between the gas molecule and surface system. Computationally, this is done by fixing atom positions of the surface slab in the first place. The final translational energy E'_trans of the gas molecule $\mathcal{G}$ can be determined by its outgoing total momentum $\mathbf{p}'_\mathcal{G}$

$$\mathbf{p}'_\mathcal{G} = \sum_{A \in \mathcal{G}}^{N_\mathcal{G}} \mathbf{p}'_A \tag{2.89}$$

with

$$E'_{\text{trans}} = \frac{\mathbf{p}'^2_{\mathcal{G}}}{2M_{\mathcal{G}}} \quad , \tag{2.90}$$

where $M_{\mathcal{G}}$ is the total mass and $N_{\mathcal{G}}$ the number of gas molecule atoms. The scattering angle α from an incoming total momentum vector $\mathbf{p}_{\mathcal{G}}$ can be determined by

$$\alpha = \arccos\left(\frac{\mathbf{p}_{\mathcal{G}} \cdot \mathbf{p}'_{\mathcal{G}}}{|\mathbf{p}_{\mathcal{G}}||\mathbf{p}'_{\mathcal{G}}|}\right) \quad . \tag{2.91}$$

The calculation of the internal energy $E_{\mathcal{G}} = T_{\mathcal{G}} + V_{\mathcal{G}}$ requires the relative atom positions $\mathbf{x}_{\text{rel}}$ and momentum $\mathbf{p}_{\text{rel}}$ in regards to the position $\mathbf{x}_{\mathcal{G}}$ and momentum $\mathbf{p}_{\mathcal{G}}$ of the COM as reference. In the following treatment, we do not differentiate between initial and final state, due to the applicability of this evaluation at any time during the simulation.

$$\mathbf{x}_{\text{rel},A} = \mathbf{x}_A - \mathbf{x}_{\mathcal{G}} \tag{2.92}$$

$$\mathbf{p}_{\text{rel},A} = \mathbf{p}_A - \mathbf{p}_{\mathcal{G}} \tag{2.93}$$

The internal kinetic energy $T_{\mathcal{G}}$ is given by the sum of the relative kinetic energies

$$T_{\mathcal{G}} = \sum_{A\in\mathcal{G}}^{N_{\mathcal{G}}} \frac{(\mathbf{p}_{\text{rel},A})^2}{2M_A} \tag{2.94}$$

where M_A is the mass of atom A. The internal potential energy $V_{\mathcal{G}}$ is determined by the potential energy function or, in particular for a diatomic molecule, by $V_{\text{gas}}(r)$ and the atom distance r.

The prediction of state-resolved properties from quasi-classical dynamic simulations requires the reconversion of the internal properties of the reactants into a set of quantum numbers. It is appropriate for diatomic molecules to determine the rotational quantum numbers j and m_j first via the classical total angular momentum L of the molecule

$$L = \sum_{A\in\mathcal{G}}^{N_{\mathcal{G}}} \mathbf{x}_{\text{rel},A} \times \mathbf{p}_{\text{rel},A} \tag{2.95}$$

and the relations of equation (2.86) and (2.88). Due to the classical propagation, the quantum numbers are no integer any longer and are recovered by rounding to the closest integer value. The vibrational quantum number is determined by comparing the internal energy $E_{\mathcal{G}}$ of the diatomic molecule with the eigenvalues $E_{\nu,j}$ of the previously assigned

rotational quantum state j. The closest match determines the vibrational quantum number ν.

The standard quasi-classical trajectory studies uses the histogram binning technique, where the probability of a particular quantum state $P(n)$ is

$$P(n) = \frac{N(n)}{N} \quad . \tag{2.96}$$

N is the total number of trajectories and $N(n)$ is the number of trajectories in quantum state n, associated with any of the quantum numbers ν, j or m_j. The Gaussian binning method, provided by Bonnet and coworkers,[167,168] is an alternative more accurate binning technique but requires a larger number of trajectories for an efficient application. Since it was not used in the present thesis, we will not discuss the details any further.

Chapter 3

Publications

The following chapter contains the scientific papers published in the context of this thesis. For each publication, the contributions by the individual authors are outlined.

Paper A

"How surface reparation prevents catalytic oxidation of carbon monoxide on atomic gold at defective magnesium oxide surfaces"

K. Töpfer and J. C. Tremblay
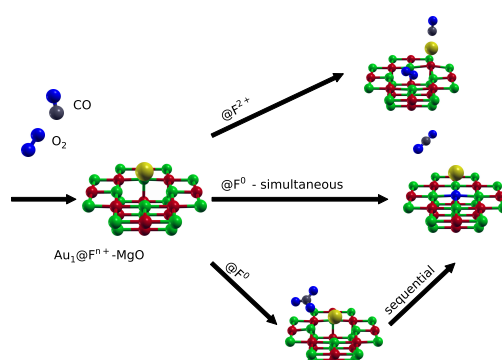
Figure 3.1: Graphical Abstract.[A] (©2016 Royal Society of Chemistry)

Author contributions

The idea was conceived by Jean Christophe Tremblay. I performed all quantum chemistry simulations. Both authors contributed to the analysis of the data. The manuscript was written by myself with significant input from Jean Christophe Tremblay.

Paper B

"First-Principle Investigations of the Interaction between CO and O_2 with Group 11 Atoms on a Defect-Free MgO(001) Surface"

K. Töpfer and J. C. Tremblay
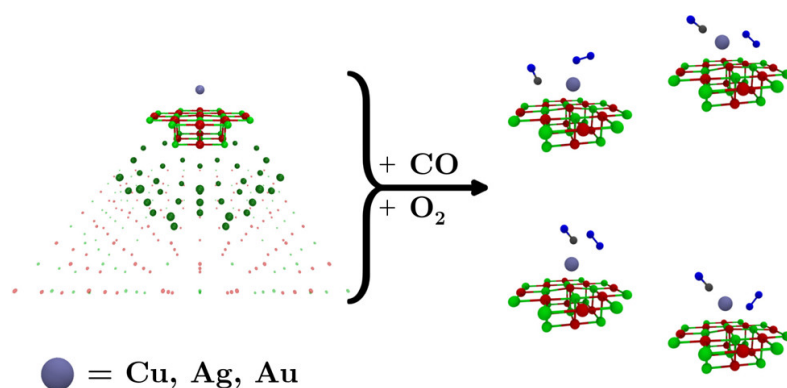
Figure 3.2: Graphical Abstract.[B] (©2018 American Chemical Society)

Author contributions

The idea was conceived by Jean Christophe Tremblay and myself. I performed all quantum chemistry simulations. Both authors contributed to the analysis of the data. The manuscript was written by myself with significant input from Jean Christophe Tremblay.

Paper C

"Energy Transfers in a Weakly Coupled Gas-Surface System: The Scattering of CO from MgO(001)"

K. Töpfer, G. Füchsel and J. C. Tremblay

submitted, **2019**
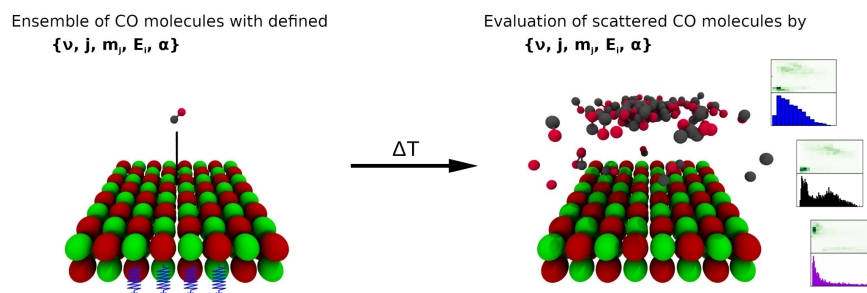
Figure 3.3: Graphical Abstract.[C]

Author contributions

The dynamical scattering simulations of CO on a clean MgO(001) surface is a step towards the dynamic simulations of gas molecules with a supported gold atom, where the basics are done in the previous work[A,B]. I have implemented the REBO-FF[156] and wrote a program to fit the parameters to reference data calculated by myself using the computational setup in paper B[B]. I expanded a MD simulation program originating from the work of Jean Christophe Tremblay and implemented a scheme for quasi-classical initial conditions and the evaluation of the trajectories based on the work of Gernot Füchsel[93] . I have performed the MD simulations for different initial conditions under the supervision of Gernot Füchsel. The results are discussed by all three contributors. The majority of the manuscript and all the figures are done by myself in collaboration with Jean Christophe Tremblay and Gernot Füchsel.

ARTICLE TYPE

Energy Transfers in a Weakly Coupled Gas-Surface System: The Scattering of CO from MgO(001)

Kai Töpfer*[1] | Gernot Füchsel[1] | Jean Christophe Tremblay†[2]

[1]Institut für Physikalische und Theoretische Chemie, Freie Universität Berlin, Arnimallee 22, 14195 Berlin, Germany

[2]Laboratoire de Physique et Chimie Théoriques, CNRS/Université de Lorraine, UMR 7019, 1 Bd Arago, 57070 Metz, France

Correspondence
*K. Töpfer, Email: kai.toepfer@fu-berlin.de,
†J.C. Tremblay,
Email: tremblay1@univ-lorraine.fr

Abstract

In this work, we investigate the non-reactive scattering of CO from a MgO surface theoretically by performing quasi-classical dynamics simulations. We shed light on the role of the incidence energy, the initial ro-vibrational state of impinging CO and the effect of surface atom motion on the scattering behavior of the molecules. Our results rely on a high-dimensional potential energy surface which we fitted using the reactive bond order force field of Busnengo and coworkers to reproduce reference energy data obtained from new cluster embedded density functional theory calculations. According to our calculations, the interaction of CO with MgO(001) is weak and characterized by a shallow adsorption minimum of about $170\,\text{meV}$ when CO approaches an Mg ion. The analysis of the computed time of flight spectra reveals two different scattering channels, that is, scattering processes associated with short and long scattering times. This behavior becomes particularly noticeable at low incidence energies, thus, yielding traces of the shape of the interaction potential between CO and the two species of surface atoms. In agreement with other CO + surface systems, we also find that the scattering process is strongly influenced by the anisotropy of the potential for CO impinging in upward or downward directions. Further, the evaluation of state-to-state scattering shows that the process is mainly translationally inelastic for impacts of CO in downwards alignment, whereas the translationally elastic regime dominates for impacts of upward CO. This observation is in accordance with the Baule model. The distinct scattering features are significant at low incidence energies when surface atom motion is included in the simulations. This suggests that the modelling of energy transfer processes is very important to describe the dynamics of the system.

KEYWORDS:
Force Field, Diatom-Surface Scattering, Molecular dynamics

1 | INTRODUCTION

Reactions of atoms and molecules catalysed at surfaces constitute a substantial amount of chemical reactions performed in chemical industry and, thus, make up an important economic factor in modern societies.[1] Investigations on elementary processes in heterogeneous catalysis such as making and breaking bonds have therefore a long tradition in surface science. Particularly,

molecular beam (MB) scattering experiments are a powerful technique to study the reaction dynamics at the gas-solid interface[2,3], because they allow to investigate the dependence of early reaction steps in a chemical reaction on the applied reaction conditions and this can be done in a well-defined manner. Reactive and non-reactive scattering experiments performed on gas-surface systems yield details about the reaction mechanism, topological features of the gas-surface interaction potential and help to better understand energy transfer processes which may occur in collision events. For instance, it is well known that reactions of late barrier systems associated with reaction barriers closer to the product states are more efficient when vibrational energy is added initially to the molecule rather than translation energy. The opposite effect is found for reactions of early barrier systems, associated with reaction barriers closer to the reactant state. The importance of the initial ro-vibrational state of the incident molecule on its reactivity has often been investigated on systems including diatomic molecules.[4,5,6] Corresponding work on polyatomic molecules has considerably intensified over the past two decades, because correlations between reactivity and initial ro-vibrational state are then more complicated.[7,8] Further, sticking probability curves recorded as functions of the incidence translational energy often clearly indicate whether a barrier to reaction exists and, if it does, the value of the effective activation energy can be determined. State-to-state scattering experiments performed at non-reactive conditions additionally raise the possibility to screen the topology of the potential energy surface (PES) and to measure energy transfer processes.[9] The latter may occur between molecule and surface, but can also be a result of internal vibrational energy redistribution (IVR) in the molecular degrees of freedom (DOF) only, particularly if there is a large mass mismatch between molecular projectile and surface atoms. Energy conversions due to IVR are ruled by the (electronic ground state) PES and conserves the total energy of the molecule. Energy transfer processes between molecule and surface, however, are often associated with energy losses in the scattered particle, and can be mediated by two different dissipative channels, phononic and electronic. While the phononic channel is relatively well understood and commonly involved in systems with large gas-to-surface mass ratios, the electronic channel is less common and typically limited to low band-gap materials and metal catalysts.[10] Prominent examples of gas-surface systems exposing considerable electronically non-adiabatic effects are, for instance, the NO + Au(111)[11] and the H + Au(111) systems[12]. The presence of dissipative channels may lead to a reduced reactivity. However, such a correlation is not always found, particularly when energy losses occur in a molecular DOF that is not aligned with the reaction coordinate.[13]

Besides the specific choice of the "external" reaction condition that can be made to enhance the reactivity, reactions are also found to be structure-sensitive. In such cases, the catalytic activity of a catalysts does not only depend on the specific material but also on the surface structure and the size of the nanoparticle. Structure-reactivity correlations were already established earlier[14] and suggested that reactions often occur at edges and corners of nanoparticles. A later work of Zambelli et al.[15] revealed the importance of surface imperfections for the dissociation of NO on Ru(0001), as this reaction was found to occur predominantly over A- and B-type steps of the Ru surface. Since then overwhelming experimental evidence was gathered which supports the general view that steps, kinks, and vacancies on surfaces constitute special active sites in heterogeneous catalysis, and observations made to the contrary may be regarded as anomalous[16]. The promotion effect of edges is exploited in the design of supported metal nanoparticles and single metal atom catalysts[17,18]. The interaction between the native catalyst and the support material is often crucial for the catalytic activity. For instance, single Au atoms deposited on an MgO support have been found to be very efficient in the hydrogenation reaction of ethene, while Au_n clusters with n≫1 were significantly less efficient. MgO-supported Au_8 clusters were also observed to be catalytically more active in the oxidation of CO when the MgO(001) film was rich on F-centers, that is, rich on oxygen defects[19]. This is believed to be related to a charge transfer process occurring between the native catalyst and the MgO support and which effect diminishes for defect-free MgO. Additionally, it might also well be that the electronic interactions between support and metal matters for the geometric structure of the cluster, which then would interfere with the catalytic activity of the system. The examples given above already outline the operational performance of MgO to act as a high-surface support material in heterogeneous catalysis. Not only the possibility for charge transfer processes are of interest for the use of MgO, but also the large variety of MgO structures tailored by different preparation methods is important for its application as support.[20,21]

The oxidation of CO is an extensively studied reaction and used to convert toxic CO into comparably harmless CO_2. Gold nanoparticles supported by MgO have been reported to be efficient in catalysing this reaction, even at rather extreme conditions at temperatures down to -70°C.[22] Although the reaction mechanism is not yet fully understood due to the complexity of the structures and the Au/MgO interaction, it is assumed that the reaction proceeds over an unusual Langmuir-Hinshelwood mechanism, because adsorption of oxygen on Au clusters requires a charge transfer mechanism as enabled by MgO supports.[21,23,24] On the other hand, the MgO support appears chemically inert for oxygen and CO adsorption, and CO appears to have only weak interactions with (001) and (111) facets of MgO, see ref. 25 and references therein. From previous molecular beam experiments performed on non-reactive scattering of CO from a bare MgO(001) surface[26], a quasi-elastic scattering process was determined

which appeared to be evident for a weak CO-MgO interaction. The angular scattering distribution assumed a cosinus-like dependence[27] and its shape was not much affected by an increase of the surface temperature from room temperature up to $T_s = 400°C$. This suggested low residence times of CO on the surface due to weak CO-MgO interactions. This is in accordance with heat of adsorption measurements which have revealed a weak CO-MgO(001) attraction with contributions arising possibly from dipole-polar surface interactions.[28]

From temperature programmed desorption experiments different CO-MgO(100) absolute binding energies were extracted. In ref. 29 a value of $E_{ads} = 0.14$ eV was reported, whereas a value of 0.4 eV was given in ref. 30. The situation on the theoretical side is very similar. Early ab initio calculations performed at the Hartree-Fock level of theory computed a binding energy of $E_{ads} = 0.4$ eV[31]. With density functional theory energy values from 0 to 0.282 eV were obtained, see ref. 32 and references therein. The reproduction of experimental values by electronic structure calculations is difficult due to a number of reasons already outlined in ref. 33, including the fact that experiments itself have uncertainties.

The above experimental and theoretical efforts made to understand the elementary interaction of CO with MgO(001) emphasizes its importance for the description of the more complex CO oxidation reaction on Au clusters supported by MgO. In this work, we present the first detailed theoretical dynamics investigation on the non-reactive scattering of CO from an ideal MgO(001) surface. The interaction potential is represented by a high-dimensional PES adopting a force field ansatz which we fitted to *ab initio* energy points obtained from cluster embedded calculations and the B3LYP functional[34,35] in accordance with our previous work.[36] We are interested in determining energy transfer processes from the CO molecule to a MgO(001) surface, angular scattering distributions, the importance of surface atom motion and that of the impact site for scattering properties.

The work is organized as follows. In the next section, we present methods and models. This includes the PES construction and the reference *ab initio* data to which the PES is fitted, as well as details about the classical molecular dynamics simulations. In the Results section, we characterize important features of the PES, and properties of scattered molecules from the rigid surface compared with a scattering process on a non-rigid surface. Finally, we summarize the results in the Conclusion section and give a brief outlook to future research.

2 | METHODS AND MODELS

In this work we simulate the scattering dynamics of CO on a defect-free MgO(001) surface by means of quasi-classical molecular dynamics (MD) simulation on a pre-computed potential energy surface. We investigate the scattering behaviour at normal incidence for different incident energies and assess the impact of rigid versus movable surface ions on energy transfer processes and internal energy redistribution. The interaction of the molecule with the surface is described in full-dimension, including surface atom motion, using a reactive bond order force field (REBO-FF) adapted for the work by Busnengo and coworkers.[37] Fig. 1 shows the coordinates used to describe the system dynamics: the cartesian positions of the surface ions subject to periodic boundary conditions in the surface plane, the cartesian coordinates of the CO center of mass (COM), the internal CO bond length R, and the polar and azimuth angles Θ and Φ. In the following, we will summarize the detail of the models and methods used throughout this work.

2.1 | Potential Energy Surface

Here, we use a modified version of the full-dimensional PES for gas-surface interaction proposed by Busnengo and coworkers[37], which is based on the reactive empirical bond order potential by Brenner *et al.*[38] The REBO-FF expresses the electronic structure as the sum of repulsive and attractive pairwise atomic interactions, with the chemical environment around the bond treated as three-body terms, the so-called bond-order term. All pairwise interactions are weighted by a smooth cutoff function depending on the distance between the atom pair. An additive non-binding contribution further improves the description of the long range Coulomb force. The simple form of the REBO-FF renders evaluation of the PES efficient, which is important for MD simulations.

In the present work, we modify the original form of the bond-order term, which is written as a sum of Legendre polynomials for the angular dependency and a distance-dependent term with proper r^{-6} dispersive asymptotic behaviour. For a given system, the two-body parameters and the bond-order term of the REBO-FF are fitted to reproduce a set of *ab initio* calculations at different geometries (see next section). This is done here by fitting a first set of parameters for the two-body interaction of the
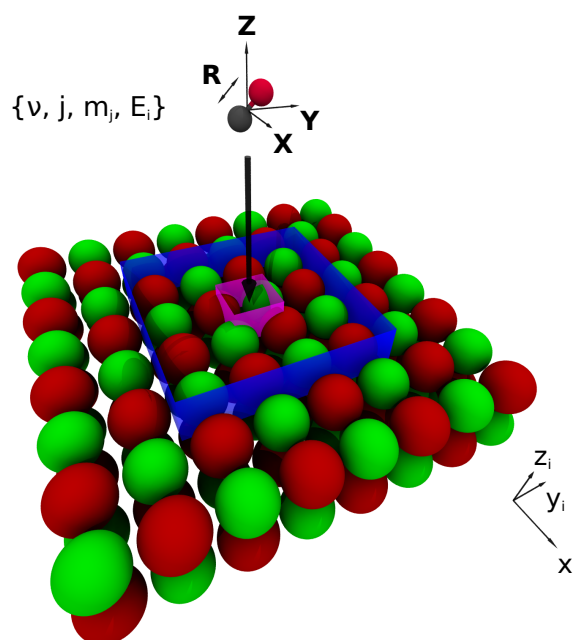
FIGURE 1 Schematic representation of a CO molecule (red and black beads) approaching a MgO(001) surface (green and red beads). The CO configuration is described by the cartesian position of its center of mass ($\{X, Y, Z\}$), the internal bond length (R), the polar angle Θ relative to the surface normal (not shown), the azimuthal angle Φ. The surface is described by a first layer of 16 movable ions with cartesian positions $\{x_i, y_i, z_i\}$ (area within the blue box), embedded in a MgO(001) cluster with periodic boundary conditions. The initial conditions for CO are defined by the initial kinetic energy E_i, as well as a quasi-classical ensemble corresponding to the ro-vibrational quantum numbers $\{v, j, m_j\}$. The molecule is scattered at normal incidence in the surface area defined by the purple box.

individual atoms of the molecule with the surface ions. These parameters serve as initial values for fitting sequentially the three-body and two-body terms for the full molecular interaction with the surface. For the interaction of the atoms of the molecule with those of the surface ions, the pairwise potential is damped in the range from 6.0 Å to 8.4 Å. This accounts for the long-range Coulomb interactions. The parameters for the intramolecular interaction of CO are further constrained to reproduce the experimental anharmonic vibrational spectrum[39] with a weighting of 2:1 favoring the reproduction of ab initio points. The interaction among surface ions is simplified to include only the two-body terms. The Coulomb interaction between surface ions with the same charge is simplified to its repulsive part only. The interaction among the surface ions are smoothly damped in the region from 3.0 Å to 4.7 Å. The detail of these modifications can be found in the supplementary material.

As a result of the fitting procedure described above, the PES remains below the chemical accuracy threshold (root mean square error: ≤ 1 kcal/mol) up to an energy of 1.2 eV above the minimum. The PES reproduces all topological features of the reference data, such as the two local adsorption minima atop a Mg^{2+} ion for CO pointing upwards ($E_{ads} = 0.17$ eV) or downwards ($E_{ads} = 0.08$ eV). The experimental adsorption energy for CO on a bulk MgO(001) surface[29] ($E_{ads}^{(exp)} = 0.14$ eV) is also found to be close to the value computed with the fitted REBO-FF.

2.2 | Reference ab initio data set

The reference data set used to fit the parameters of the REBO-FF is calculated at the density functional theory level using the B3LYP hybrid functional[34,35], with the interaction with the surface computed using the periodic electrostatic embedded cluster method (PEECM).[40] The different structures represented in the data set are generated using the Atomic Simulation Environment.[41] Gas phase carbon monoxide is described by a 6-311+G* basis set of triple zeta quality and the potential path is sampled by 120 reference points of different bond lengths between [0.8, 9] Å. The MgO(001) surface is simulated by a $Mg_{25}O_{21}$ cluster centered around a Mg^{2+} ion, embedded into a periodic array of point charges. Mg^{2+} and O^{2-} ions of the substrate are

described using 6-311G and 6-31+G basis sets, respectively. Using a lattice constant of $L = 4.212\,\text{Å}$ results in a vertical ionic potential of the cluster ($IP_{\text{cluster}} = 6.65\,\text{eV}$) close to the experimental value of $IP_{\text{exp}} = 7.110\,\text{eV}$.[42] The potential for the surface ions is sampled by moving two adjacent Mg^{2+} and O^{2-} ions within the cluster in all three cartesian directions by up to $0.4\,\text{Å}$ around the equilibrium geometry, amounting to 210 different configurations. The combined system of CO and MgO(001) is sampled at the high-symmetry points in the surface plane ($\{X, Y\}$ (Mg^{2+}, O^{2-}, bridge, hollow). The molecule-surface height is sampled on the range $Z \in [2.0, 15]\,\text{Å}$, and the internal vibration from $r \in [1.0, 1.4]\,\text{Å}$. The orientation was varied from $\Theta \in [0, 180°]$ in 30° steps, and the azimuthal angle Φ fixed at either 0 or 45°. All configurations with electronic energy larger than 5 eV above the global PES minimum where systematically discarded, amounting to a total of 1500 reference points. A similar sampling strategy along the $\{X, Y, Z\}$ coordinates is used for the interaction of single C and O atoms on a MgO(001) cluster, leading to about 150 reference points in each case. All electronic structure calculations are performed using the TURBOMOLE 7.1 program package.[43,44,45]

2.3 | Dissipative molecular dynamics

The scattering of CO from MgO(001) is simulated by MD simulation using a full-dimensional analytic PES of the REBO-FF form, including motion of selected surface atoms. Periodic boundary conditions are applied along the directions parallel to the surface. In the dynamics, the surface is represented by a 4x4x1 slab of length $16.848\,\text{Å}$, which is twice as long as the cutoff limit in the REBO-FF potential ($8.4\,\text{Å}$). This prevents any double counting of molecule-surface interactions due to periodic boundary conditions. To reduced computational cost, only the top layer ions within the area of the central 2x2 unit cell (16 ions in total) are allowed to move. To simulate energy dissipation to the substrate phonons, the momentum p of the movable surface ions is damped at each time step,

$$p' = p \cdot \exp\left(-\tau_\alpha \cdot \Delta t\right) \tag{1}$$

The damping rates for Mg^{2+} ($\tau_{\text{Mg}} = 2.237\,\text{ps}$) and O^{2-} ($\tau_{\text{O}} = 2.670\,\text{ps}$) are obtained by fitting the dynamics of a displaced ion in a freely moving slab to a damped harmonic oscillator (see supplementary material for detail). The equations of motion are integrated numerically using the velocity-Verlet algorithm with a time step of $\Delta t = 0.05\,\text{fs}$. The maximal total energy deviation for simulation with a rigid surface remains below 1 meV during the whole propagation.

The system is prepared in a series of initial conditions representing different initial translational energies (or impact energy, E_i) for CO are sampled ($E_i = [0.05\,\text{eV}, 0.10\,\text{eV}, 0.30\,\text{eV}, 0.50\,\text{eV}]$). For each impact energy, at least 10'000 trajectories are used to sample the quasi-classical initial conditions for a chosen ro-vibrational state of CO. The probe molecule always starts at a height of $9.0\,\text{Å}$ and with momentum at normal incidence directed towards the surface. The surface temperature is set to $T_s = 0\,\text{K}$, without zero-point energy (ZPE), by optimizing the ion positions to the minimum of the REBO-FF. All sampled trajectories are distributed above the movable surface ions within the small purple area shown in Fig. 1 .

In all simulations, the impinging CO has an initial internal energy, E_{v,j,m_j}, associated with the ro-vibrational quantum state defined by the vibrational quantum number v, the rotational momentum quantum number j and the rotational angular momentum quantum number m_j. The energies are defined by the ro-vibrational Hamilton operator of a diatomic molecule for a given j as

$$\hat{H}_j(R) = -\frac{\hbar^2}{2\mu}\frac{d^2}{dR^2} + V_{\text{eff}}^j(R) \tag{2}$$

where μ is the reduced mass and R the bond distance of CO. The effective potential, V_{eff}, contains the vibrational potential energy in the gas phase and a rotational contribution

$$V_{\text{eff}}^j(R) = V_{\text{gas}}(R) + \frac{\hbar^2}{2\mu R^2}j(j+1) \tag{3}$$

The ro-vibrational energy states are obtained by diagonalizing the Hamiltonian matrix, which is represented a basis of 128 sinc-DVR functions[46] in the interval $r \in [0.69, 2.12]\,\text{Å}$. While the quantum numbers $\{v, j, m_j\}$ remain fixed for a selected state, the initial bond length R is determined by randomly choosing a time t_R within half of the vibrational period of CO and using the respective bond length $R(t_R)$. The initial angular orientation of CO with initial rotational momentum $j > 0$ corresponds to the angular distribution $P_{j,m_j}(\Theta, \Phi)$ as described elsewhere.[13] In the rotational ground state $j = 0$, CO is distributed according to a $\sin(\Theta)$ distribution and randomly along Φ.

To analyse the dynamics, we resort to energy binning to associate a quantum mechanically ro-vibrational state to the classical momentum of a given trajectory. A trajectory is considered as scattered if the CO molecule reaches the initial height of $9.0\,\text{Å}$ and has an outgoing momentum with respect to the surface ($p_z(\text{CO}) > 0$). If this condition is not fulfilled by the final propagation

time T_f, the molecule is considered trapped. In all simulations, T_f is chosen such that CO would cover at least 80 Å in free space with the given initial translational energy E_i. At the first turning point (first bounce on the surface) and at the end of each propagation, the classical angular momentum L of CO is first used to determine an approximate rotational quantum number j according to

$$\left|L_\Theta\right| = \hbar\sqrt{j(j+1)} \tag{4}$$

assuming $m_j = 0$. The rotational angular momentum quantum number m_j can then be extracted by using the projection of the angular momentum along the surface normal using the formula

$$L_\Phi = \hbar m_j \tag{5}$$

Rounding to the nearest integer the approximate values obtained from Eqs. (4) and (5) allows to bin the classical momentum into a ro-vibrational state with definite quantum numbers $\{j, m_j\}$. The vibrational quantum number is then chosen by comparing the internal energy of CO with the calculated ro-vibrational energy states of the Hamiltonian Eq. (2) at the given rotational state j. The closest ro-vibrational energy state determines the vibrational quantum number v. At the incident energies investigated in this work, the weak interaction of CO with MgO(001) is found to be insufficient to excite CO from its initial vibrational ground state.

3 | RESULTS AND EVALUATION

3.1 | Potential Energy Surface Topology

Figs. 2 and 3 show selected 2D cuts of the PES that can be used to rationalize the scattering behaviour of CO at different surface sites and incident energies E_i. The interaction energy between the CO molecule and a MgO(001) surface is mostly determined by the electrostatic interaction between the molecular dipole and the surface ions. CO only exhibits a small dipole moment in the gas phase, which is barely affected by the vicinity of the surface. Consequently, the magnitude of the interaction remains well below that of covalent bonds, and the typical molecule-surface distance in the interaction region is found between a chemisorption and physisorption. From a dynamical point of view, collisions at incident energies comparable to the potential depth allow to probe the PES topology more efficiently, leaving more time to the projectile to approach the surface in a favourable orientation and inducing significant vibrational and rotational energy redistribution. Because the CO-MgO(001) interaction is so weak, the topological effects will disappear rapidly as the initial velocity of the scatterer increases. Figure 2 reveals a larger corrugation of the potential along angle Θ with CO placed atop O^{2-} (bottom left panel) and the bridge site (top right panel) than atop Mg^{2+} (top left panel). The position of the PES minimum atop O^{2-} is also tilted by about 60°, with the hollow site (bottom right panel) representing an intermediate case. These findings imply that a higher rotational force will be felt by CO molecules scattering from an O^{2-} ion at the surface and away for the Mg^{2+} ion.

For CO in the upright position, i.e., with C closer to the surface, the molecule is found in its global potential energy minimum atop the Mg^{2+} ions, while it remains far from the surface above O^{2-} ions. This will affect the time of flight before collisions occur at each ionic sites. In the downward conformation, a shallow potential minimum is found atop the Mg^{2+} and at the bridge site. This can be understood from the REBO-FF parameters, which predict a stronger interaction between C and Mg^{2+} ions. This leads to a preference for a Mg^{2+}–C–O alignment, which explains that the PES minimum at the bridge site is found at about 35° with the oxygen pointing away ($\Phi = 0°$). This defines a broad flat potential valley around Mg^{2+} that will tend to attract CO at low impinging energies and confers a stronger degree of alignment to the scattered molecules.

The right panel in Fig. 3 shows the potential surface of CO at different heights in Z along the 1D path in the XY-plane. The path is chosen to sample all important high-symmetry points along the surface, going from Mg^{2+} over the bridge site to O^{2-} and via the hollow site back to Mg^{2+}. It is sketched as a dashed line in the top left panel. The potential cut shows a strong corrugation when CO stands upright (top right panel). At $\Theta = 45°$, the PES minimum shifts towards the bridge position, favoring the linear arrangement between Mg^{2+}–C–O. It is interesting to note that the well depth remains almost unchanged. This is indicative of a relatively flat topology around Mg^{2+} ions, as long as the preferred orientation can be adopted. This is likely to favor trapping upon scattering at low incident energy, as the molecule will be attracted towards the most stable adsorption minimum.

Also, the large lateral force applied on impinging CO molecules should lead to a broader distribution of the scattering angles for the molecules scattering from regions belonging to Mg^{2+} ions. This is not what is observed, as will be shown below. The comparably deep potential wells for CO with upright orientation allows the favourable realignment at low impact energy and thus gaining rotational momentum but lowering the effective lateral force. For CO at $\Theta > 90°$, the interaction energy with the
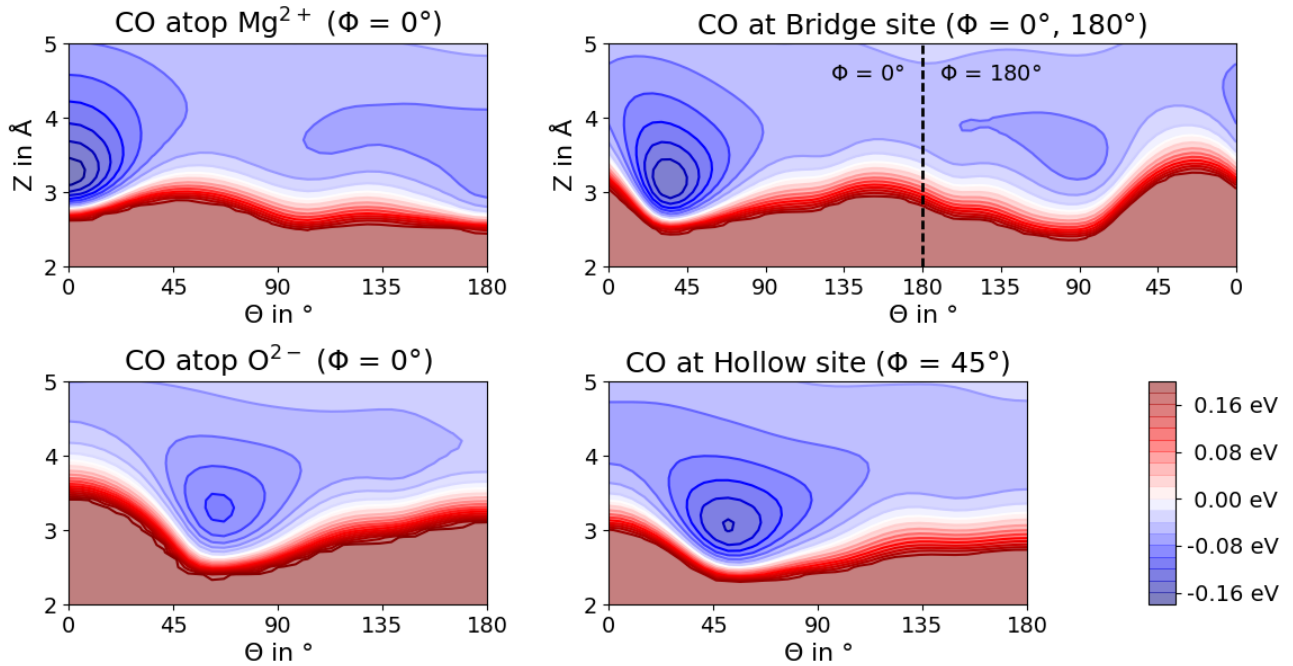
FIGURE 2 Potential energy surface cuts in the $Z\Theta$-plane. The center of mass of CO is placed atop Mg^{2+} (top left panel) or O^{2-} (bottom left panel), at the bridge site (top right panel), and at the hollow site (bottom right panel). The azimuthal angle points towards the neighbouring ion ($\Phi = 0°$, and $\Phi = 45°$ at the hollow site) of the closest ion ($\Phi = 180°$). The CO bond length R is optimized at each point.

surface is too weak to favour such adiabatic reorientation. For all impact sites, the potential energy surface is too flat to influence the dynamics at larger incident energies and the large lateral force applied on impinging CO molecules should lead to a broader distribution of the scattering angles for the molecules scattering from regions belonging to Mg^{2+} ions.

On the contrary, the PES is almost flat in the XY-plane when the CO lies parallel to the surface, with some small degree of corrugation when the molecule points downwards. As a consequence, trajectories scattering from O^{2-} ions should show a narrower distribution of scattering angles. CO impinging at around $\Theta = 90°$ shows a moderate rotational gradient around Θ at all high symmetry points in Fig. 2 . The translational motion normal to the surface will probably be converted into a larger rotational excitation, that additionally couples with the lateral movement and results in a broader scattering angles distribution.

3.2 | Scattering from a Rigid Surface

In this section, we aim at understanding the role of the potential topology on the product distribution of the CO/MgO(001) scattering process. Figure 4 shows the translational energy loss (top panels), the rotational excitation probability (central panels), and the scattering angle distribution (bottom panels) for the normal incidence scattering of CO initially in the ro-vibrational ground state ($v = 0, j = 0$) from a rigid surface. Simulations for CO($v = 0, j = 1$) show similar trends and will not be discussed in detail (see supplementary information for detail). As expected, the translational energy loss increases smoothly with higher rotational excitation. No vibrational excitation is possible due to the very weak molecule-surface interaction and the low initial translational energy, which is much lower than the CO internal stretch mode vibration ($\sim$ 2140 hc/cm). As a consequence, all translational energy is converted to rotational motion in the case of a rigid surface. This is confirmed by looking at the average translational energy loss ($\langle \Delta E_i \rangle$), which is equal to the rotational energy gain ($\langle \Delta E_j \rangle$) at all incoming energies, within the accuracy of the present computational setup. Although the translation energy loss increases as a function of the initial translational energy, its relative importance decreases. This is due to the weak interaction with the surface and the reducing contact time at higher velocities. The central panels reveal a weakly structured final rotational state distribution at low incident energies. Fitting to an ideal Boltzmann distribution yields an approximate linear relationship between incident energy and rotational temperature. The agreement with the Boltzmann fit is better at higher energies, where the small features in the rotational distributions
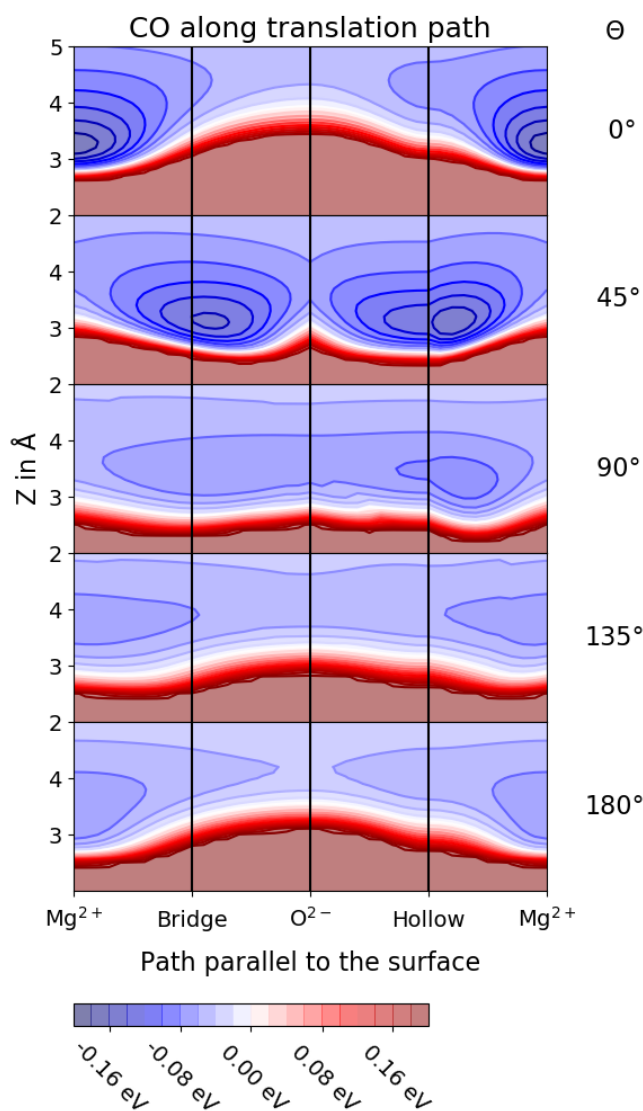
FIGURE 3 Potential energy surface along Z and a 1D path in the XY-plane of the surface for different angles Θ. The CO bond length R and the angle Φ are optimized at each reference point.

disappear. This double peak structure at the lowest incident energy is better observed in the scattering angle distribution (bottom panels). Whereas it is unimodal, smooth, and narrow at $E_i = 0.30$ eV, two peaks at $\sim 20°$ and $\sim 40°$ can be distinguished from the broad distribution at $E_i = 0.05$ eV. The distribution becomes narrower and the peaks disappears in the intermediate case at $E_i = 0.10$ eV, while the direct back scattering at small angles becomes more probable. Because of the weak molecule-substrate interaction, the effect of the potential topology on the scattering products vanishes rapidly with increasing incident energy. In particular, the very low trapping probability, $P_{trapped}$, observed on the rigid surface at $E_i = 0.05$ eV completely vanishes.

To understand the final rotational probability and scattering angle distributions, the role of the impact site and of molecular orientation is investigated. To this end, the surface is divided in areas belonging to Mg^{2+}, to O^{2-}, and to hollow sites, using the effective ionic radii by Shannon[47]. The effective ionic radii of Mg^{2+} ($r_{ionic}(Mg^{2+}) = 0.86$ Å) and O^{2-} ($r_{ionic}(O^{2-}) = 1.22$ Å) are scaled down by a factor $s = 0.993$, such that the sum of both diameters corresponds to the lattice parameter of the unit cell, $L = 4.212$ Å. The resulting ion areas are delimited in the left panel of Fig. 3 by orange and purple lines for Mg^{2+} and O^{2-}, respectively.

Fig. 5 shows rotational excitation probability and scattering angle distribution for trajectories at different impact sites, together with the angular orientation Θ of CO upon impact. At the low incident energy ($E_i = 0.05$ eV, left panels) the two peaks
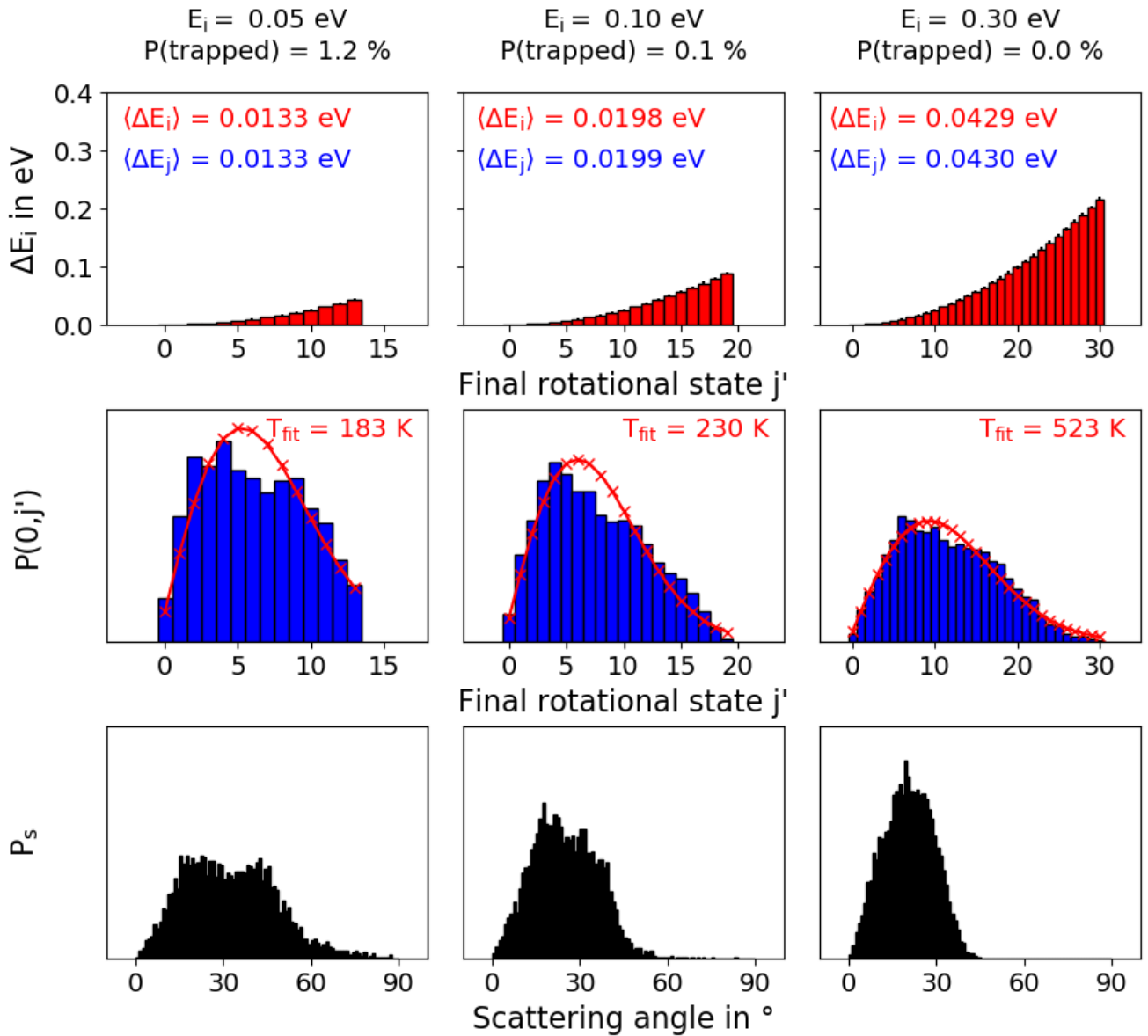
FIGURE 4 Scattering of CO($v = 0, j = 0$) from a rigid MgO(001) surface at different initial translation energies E_i. Top panels: State-resolved translational energy loss. The average translational energy loss ($\langle \Delta E_i \rangle$) and average rotational energy gain ($\langle \Delta E_j \rangle$) are given in red and blue, respectively. Central panels: Rotational excitation probability, $P(0, j')$, and best fit to a Boltzmann distribution (red line). Bottom panels: Scattering angle probability distribution.

observed in the rotational distribution in Fig. 4 originate from two different orientations of CO at the impact. This distinction is particularly clear for scattering from the Mg^{2+} ions (top left panels). The peak at lower scattering angles is caused by trajectories where CO is upright, while CO pointing downwards is mostly responsible for the peak at higher angles. Low incident energies provide a longer time for CO to adopt an energetically favorable orientation than at higher incident energies. Guiding the molecule towards the optimal Mg^{2+}–C–O alignment effectively minimizes the force along the angle Θ, as can be seen from the potential curves in Fig. 2 . This results into a lower rotational excitation and smaller scattering angles for trajectories colliding with Mg^{2+} ions than with O^{2-} ions or on hollow sites. CO pointing downwards shows a peak at larger scattering angle despite the flat potential topology (bottom right panels of Fig. 3). This might result from a more effective coupling between rotational and lateral movement, which is not visible from the figure. The different scattering angle distributions between the two CO alignments upon impact decreases at larger incident energies (top right panels). While the scattering angles of upright CO
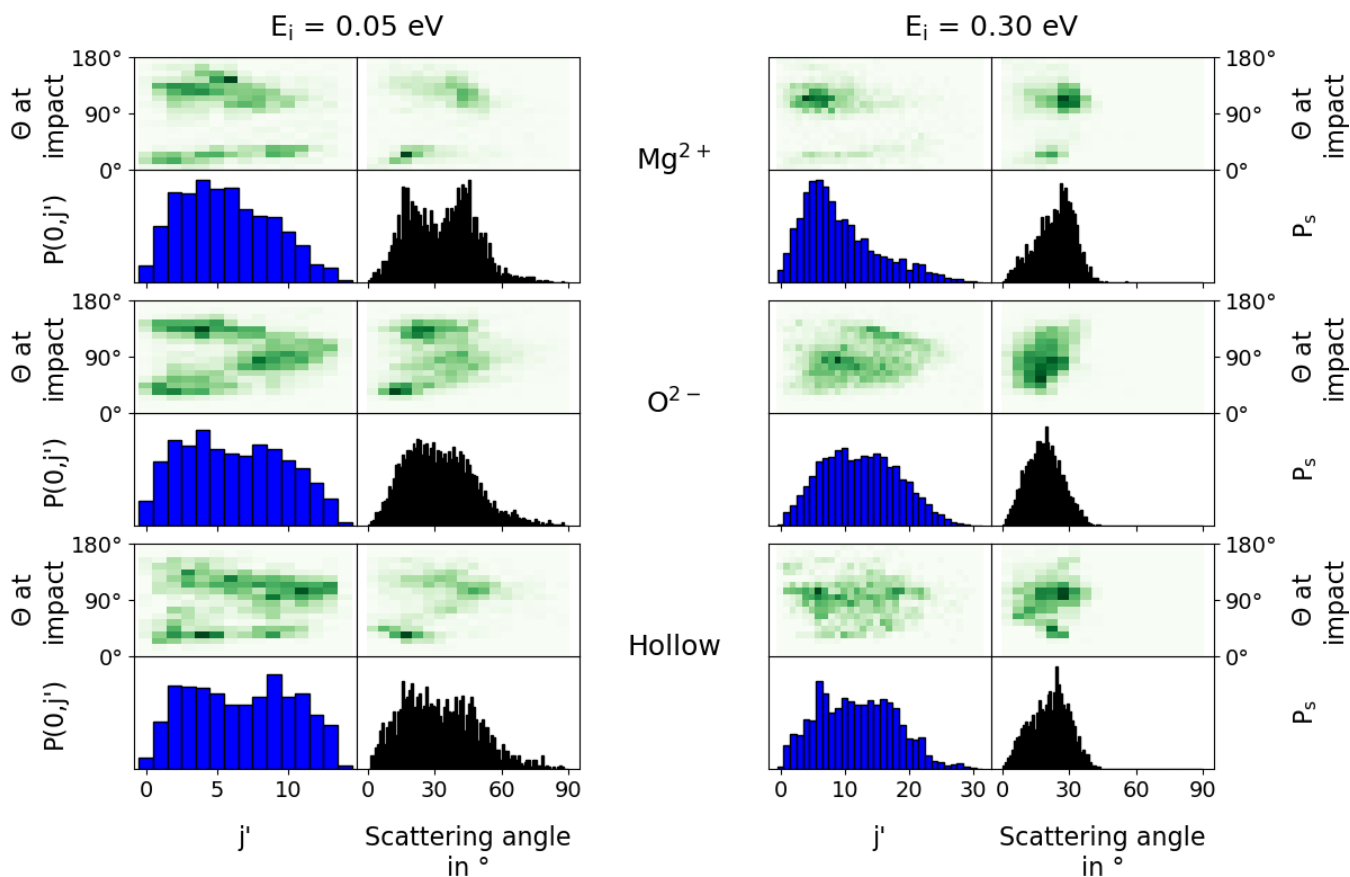
FIGURE 5 Influence of the impact site and of molecular orientation (Θ at impact) on the j-resolved rotational excitation probability ($P(0, j')$) and the scattering angle distribution P_s. CO($v = 0, j = 0$) is scattered from a rigid surface at different initial translational energies $E_i = \{0.05, 0.30\}$ eV. Results for areas belonging to Mg^{2+}, O^{2-}, and hollow sites are respectively depicted from top to bottom.

slightly increases, downward CO becomes narrower and shifts to lower scattering angles. The weak CO-MgO(001) interaction reduces the influence of surface corrugation and, with it, of the orientational gradient. It is important to note that, at the Mg^{2+} impact site, the proportion of upright to downwards collisions remains about constant (35% and 65%) at all incident energies. On the contrary, the spread of the distributions becomes much smaller as the velocity of the projectile is increased.

The trajectories at the O^{2-} impact site (central panels of Fig. 5) show a more uniform, non-thermal distribution of the rotational excitation probability ($P(0, j')$). Similar to dynamics at the Mg^{2+} impact site at low incident energies, upright CO molecules are found at the lowest scattering angles and downwards molecules scatter at higher angles. Molecules oriented parallel to the surface also tend to scatter at larger angles and to become rotationally more excited. This is a consequence of the PES topology, which shows a larger gradient along Θ at $\sim 90°$ for CO atop of O^{2-} (bottom left panel of Fig. 2). The coupling between rotational and lateral movement causes larger scattering angles despite the rather flat potential of parallel CO around O^{2-} (center right panel in Fig. 3). This is accompanied by a higher degree of rotational excitation as the molecule tries to recover the favored Mg^{2+}–C–O alignment, i.e., following the potential gradient in the hollow site (from the third to second panels in Fig. 3). At higher incident energies, these effects vanish and both the rotational excitation probability and the scattering angle distribution become narrower due to the reduced contact time with the surface.

Somewhat surprisingly, trajectories impinging at the hollow site show a similar rotational excitation probability as those at the O^{2-} impact sites, but with a broader distribution of impact angles leading to the highly excited rotational states. On the other hand, the scattering angle distribution is found between that of the two ionic sites. The azimuthal angle Φ has a large impact on the surface topology for non-perpendicular CO molecules at the hollow site. The potential character changes from strongly attractive if CO aligns towards two Mg^{2+} (i.e. $\Phi = 45°$ as shown in the bottom right panel of Fig. 2) to weakly bound when

aligning towards an O^{2-} ions (i.e. $\Phi = 135°$). A definite explanation becomes difficult with the given evaluation of the scattering results, but the potential topology at the hollow site seems to confer a strong orientation to the molecule, which is less subject to translational motion then at the O^{2-} impact site. At higher incident energy (bottom right panels), the scattering angle distribution becomes narrower and the rotational excitation probability becomes almost indistinguishable from that at the O^{2-} site. All subtle effects stemming from the PES corrugation are lost, while they are still visible at the Mg^{2+} site.

3.3 | Influence of Surface Ion Motion

In this section, the influence of movable surface ions on the energy redistribution upon scattering is discussed. Fig. 6 shows an overview of the rotational excitation probability and scattering angle distribution for different incident energies E_i. Unsurprisingly, the loss of the initial translational energy is larger for scattering on a movable surface than from a rigid one. On the other hand, the avergage rotational energy gain gets smaller than on rigid surface and amounts to about half of the translational energy loss for all incoming energies studied. The remaining translational energy goes into the surface ion motion, which reduces the energy redistribution to the CO rotation. Consequently, excitation probability of lower rotational states becomes more likely and the distribution is shifted to the left (see central panels). This observation remains valid at larger incident energies. The excitation probability distributions deviate more strongly from the ideal Boltzmann case (red curve), but the associated temperatures are much lower than in the rigid surface case. Further, a shoulder in the rotational state distributions can be observed at higher js for all initial translational energies, contrary to rigid surface scattering. Such a shoulder is not observed in the scattering angle distributions, which is also broader at low incident energies when surface ions are allowed to move. The distribution for $E_i = 0.30\,\text{eV}$ is close to the scattering angle distribution on a rigid surface. This is possibly due to the diminishing contact time and the long lifetime of surface phonons, as can be inferred from the ion damping rate in Eq.(1). Interestingly, the trapping probability (P_{trapped}) is only significant at very low impinging energies ($E_i = 0.05\,\text{eV}$). While it is also increased at $E_i = 0.10\,\text{eV}$ compared with rigid surface simulations, energy loss to phonons seems to be too inefficient to significantly enhance trapping. This result can again be understood from the damping rates in the cluster. They operate on the few picosecond regime, which is much longer than the contact time upon scattering. Note that the trapping probabilities should be taken with caution, since they are computed classically and neglect the zero-point energy of the system.

To shed light on the origin of the double peak structures, the left panels of Fig. 7 show the rotational excitation probability and the scattering angle distribution for different impact sites at the surface. The probabilities are further decomposed according to the CO orientation Θ upon impact. Only the results at the lowest incident energy are shown since the interaction time is longer and the trends become clearer. As opposed to Fig. 5 the scattering angle distribution (black) at the Mg^{2+} impact site exhibits an intense and narrow peak at small angles. According to the impact angle (green colormap), it is associated with CO approaching the surface in an upright orientation. This is associated with a rotational state distribution (blue) that is markedly skewed towards low js, with an important dip at $j' = 1$. This strong localization can be explained as follows: as CO approaches the surface at low incident velocities, it is dragged towards the Mg^{2+} surface ion, which is pushed below the first surface layer upon impact. This constrains the motion of the CO projectile by creating a stronger confinement potential than on a rigid surface. This cone-shaped potential prevents deviation of the scattered products from normal incidence. It further restricts rotational motion and confers a large degree of orientation to the scattered molecules. Since $j = 0$ is associated with a spherical orientation distribution, it explains the much lower population observed in this outgoing state. The lower adsorption minimum and broader potential cone for CO pointing downwards lead to a lower degree of localization. Consequently, the associated rotational excitation probability and scattering angle distribution behave more thermally. Simulations at higher incident energies behave similarly and will not be detailed here (see supplementary material).

The trajectories scattering around the O^{2-} impact site (central left panels) also exhibit rotational cooling as compared to simulations on the rigid surface. Upright CO is more strongly represented at low js. As on the rigid surface, rotational excitation is lower for downward CO upon impact, while a parallel alignment results into larger values in j. The scattering angle distribution correlates well with the optimal Mg^{2+}–C–O alignment, corresponding to the minimum structure at the bridge site (see Fig. 3). For this case the potential shows a low corrugation along the angle Θ and the motion parallel to the surface. As it is also observed at the Mg^{2+} site, surface ion motion leads to a more efficient reorientation of CO towards the energetic minimum structures. This subsequently increases the probability of excitation to low rotational states and small scattering angles. The influence of the impact orientation on the rotational transition probability and scattering angle distribution remains otherwise qualitatively similar to the rigid surface simulations. The same observation can be made for the remaining trajectories around the hollow site. The general trends are thus strongly dominated by the topology of the potential, despite the low interaction energy.
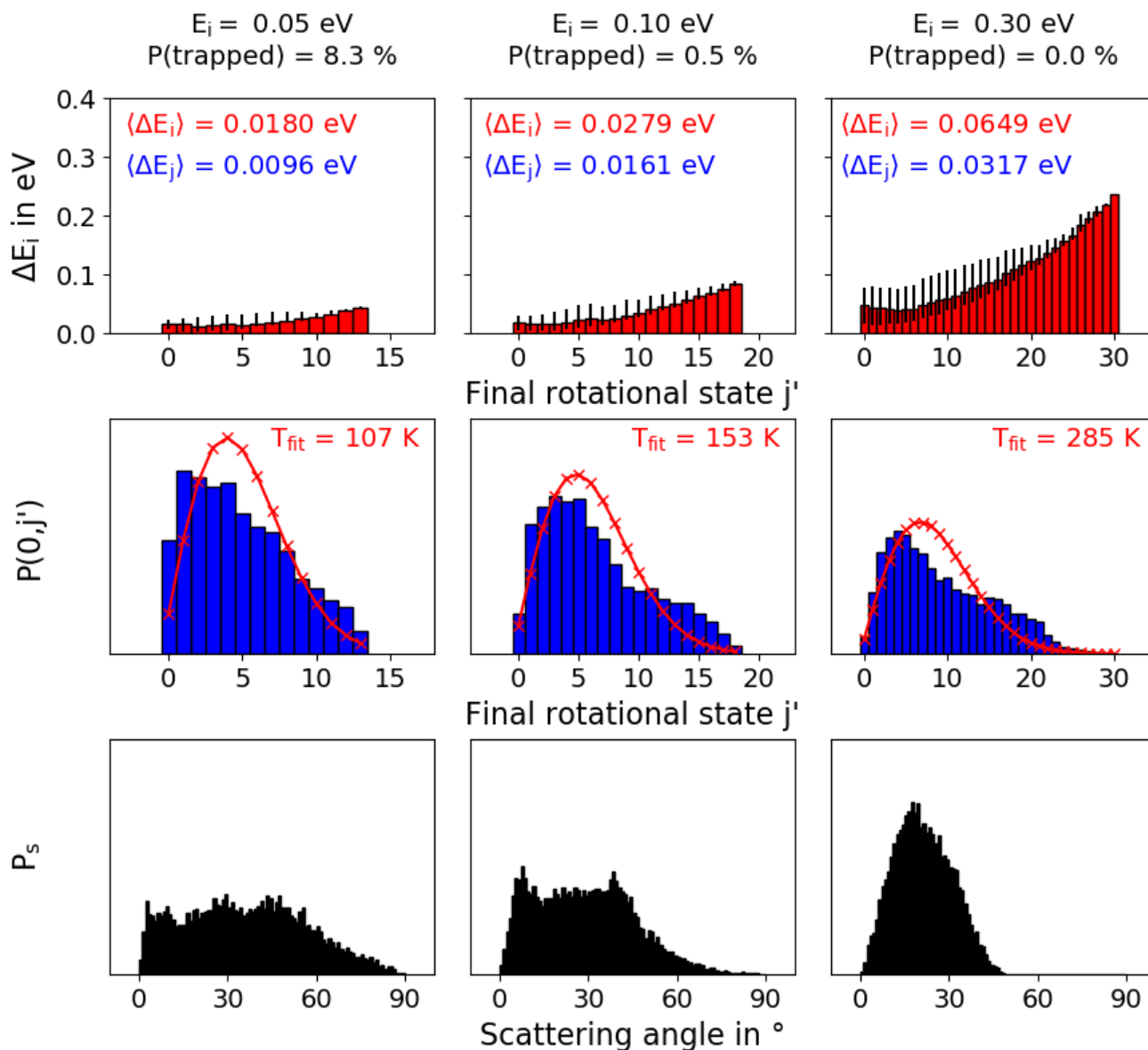
FIGURE 6 Scattering of $CO(v = 0, j = 0)$ from a MgO(001) surface including surface atom motion at different initial translation energies E_i. Top panels: State-resolved translational energy loss. The average translational energy loss ($\langle \Delta E_i \rangle$) and average rotational energy gain ($\langle \Delta E_j \rangle$) are given in red and blue, respectively. The standard deviation for the binning is shown as black bars. Central panels: Rotational excitation probability, $P(0, j')$, and best fit to a Boltzmann distribution (red line). Bottom panels: Scattering angle probability distribution.

Further information about the energy transfer to the surface can be obtained from the time of flight (ToF) spectra, which are inversely proportional to the translation kinetic energy of the scattered molecules. It is shown in the central and right panels of Fig. 7 (purple), along with the position of the Z turning point upon impact (Z_T, brown). The ToF spectra reveal an important loss of translational energy when CO molecules hit the surface pointing upwards. This observation holds for all simulated incident energies and impact areas, and it is a signature of internal energy redistribution. Scatterers adopting another orientation upon impact are less thwarted in their motion and retain more kinetic energy in the exit channel. Consequently, they should be observed first in a ToF spectrum. While all impact sites have a relatively similar profiles, with a larger peak at high velocities (short times), the separation between upright and downwards orientations is larger for collision at the Mg^{2+} site. This confirms that scattering in the downwards orientation is a more direct and more adiabatic process.
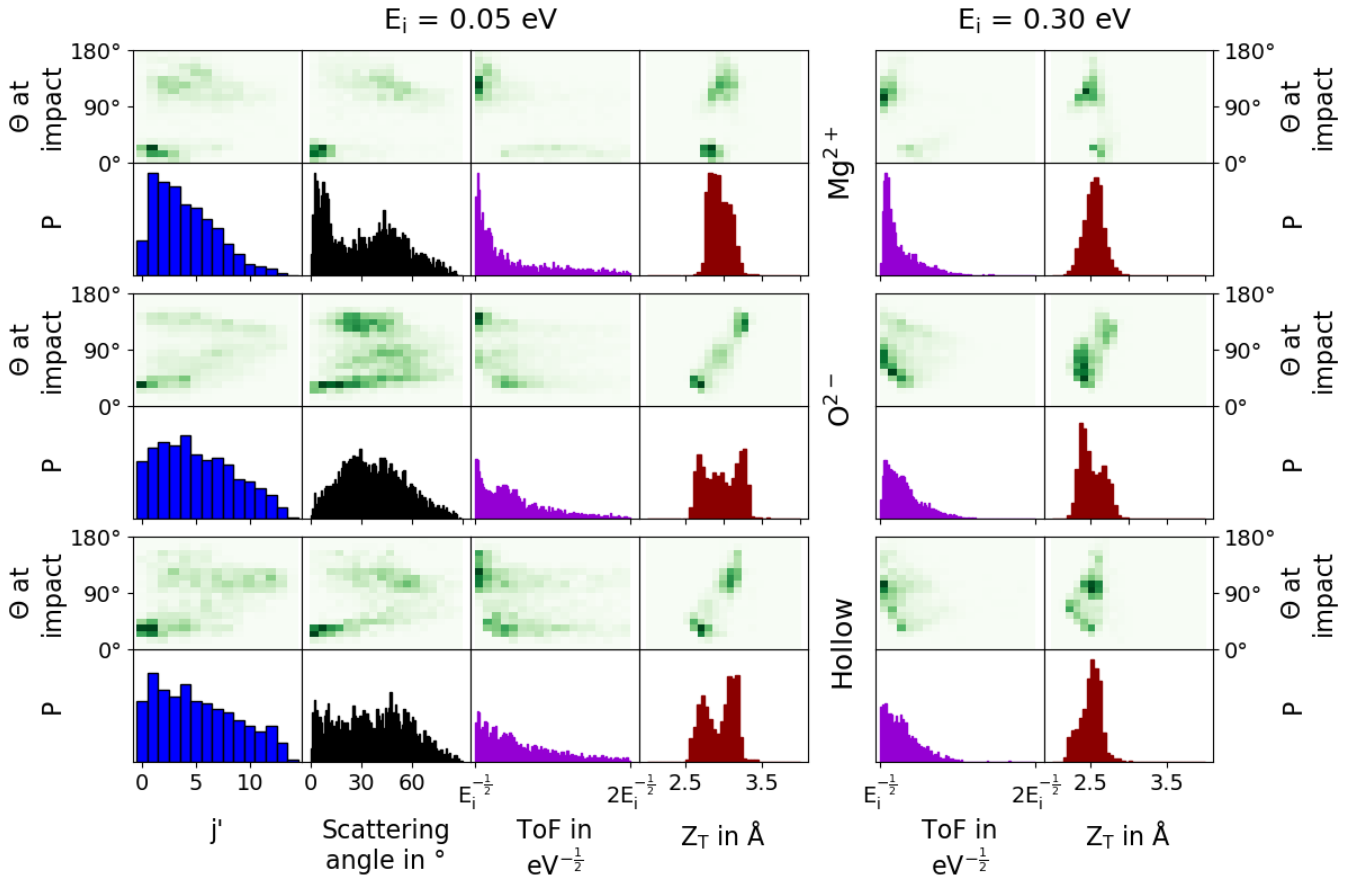
FIGURE 7 Site-resolved scattering of CO($v = 0, j = 0$) from a surface with movable surface ions. Left panels: Rotational excitation probability and scattering angle distribution at different impact sites. (top: Mg^{2+}, centre: O^{2-}, bottom: hollow) for an incident translational energy of $E_i = 0.05$ eV. The decomposition according to the CO orientation Θ is shown in the green density maps. Central and left panels: Time of flight spectra (ToF, purple) and position of the Z turning point upon impact (Z_T) at different incident energies ($E_i = \{0.05, 0.30\}$ eV).

At low incidence energies, the turning point Z_T indicates that scattering happens further away from the surface for the downwards orientation, while late scattering is observed for CO molecules incoming in an upright orientation. This can be understood from the topological feature of the PES (see Fig. 2). CO reaches a more repulsive potential later at lower distances Z from the surface around hollow and O^{2-} impact sites when it is pointing approximately upwards. Assuming an optimal orientation ($\Theta < 90°$), they go through a potential minimum valley with a late repulsive potential. Further, impinging molecules in a downward orientation ($\Theta > 90°$) have no potential minimum and reach the repulsive wall of the PES at higher Z distances from the surface, which amounts to a second peak in the distributions. This trend is reversed at higher incident energies (right panels) for trajectories impinging at the Mg^{2+} site, when CO has less time to achieve an optimal orientation. While the distribution of orientations upon impact becomes narrower for the hollow and O^{2-} impact sites, the two peaks can still be distinguished at the Mg^{2+} site due to deeper minima and the associated larger forces towards perpendicular orientation. At higher incident energies, CO molecules approach closer to the surface without significantly transferring energy to the long-lived phonons due to the reduced contact time and the weak interaction with the surface. The molecules thus fly above the interaction potential and reach, almost undisturbed in their initial orientation, the repulsive potential wall. The latter is found to be slightly closer to the surface for CO in the downwards orientation. The low turning point and later scattering of CO molecules in the upright orientation is in contradiction with experimental findings in other systems, where a narrow scattering is observed for early scattering trajectories [48]. We attribute this difference to the fact that MgO(001) presents two types of surface ions, and that the mass ratio between projectile and the surface atoms is close to unity. The latter will become important when considering energy transfer to the phonons and the perturbation of the surface ions at the impact.

Translational energy transfer from the impinging molecule to the surface depends on the mass of the projectile and the impact site. In the Baule limit[49], translational energy loss Δ is cast as a function of the adsorption energy and of the mass ratio $\mu = m_{ads}/M_{site}$ between the molecule and associated the surface atom

$$\Delta = \frac{4\mu}{(1+\mu)^2}\left(E_i + E_{ads} - \frac{1}{2}k_B T_s\right) \tag{6}$$

The prefactor for the collisions at the O^{2-} site is slightly smaller than on Mg^{2+} (0.926 vs. 0.995). At low incident energy, this can be compensated by the small adsorption energy in the different conformations. For CO on MgO(001), stable adsorption minima are observed on Mg^{2+} in both the upright (0.17 eV) and downward (0.06 eV) orientations. CO atop O^{2-} adopts a meta-stable adsorption state (0.09 eV) by keeping the favorably angled Mg^{2+}–C–O alignment. For CO in the upright orientation impinging on the Mg^{2+} site, Eq. (6) predicts the largest translational energy loss ($\Delta_{Mg-CO} = 0.21$ eV at $E_i = 0.05$ eV, and $\Delta_{Mg-CO} = 0.46$ eV at $E_i = 0.30$ eV). The ToF spectrum reveals that the energy loss for CO molecules adopting an upright orientation is much larger than for the downward orientation. The reduced mass being equal, this finding is in agreement with the higher adsorption energy for the upright orientation. At low incident energy, the Baule model further predicts a slightly larger translational energy loss at the O^{2-} site ($\Delta_{O-CO} = 0.13$ eV) than for CO molecules impinging downwards at the Mg^{2+} site ($\Delta_{Mg-CO} = 0.12$ eV). This effect is visible in the broader rotational distribution and in the longer ToF at the O^{2-} site (see left and central panels of Fig. 7). As the incident energies E_i increases, these differences rapidly become smaller, as the contribution of the adsorption energy in Eq. (6) diminishes and the trends are almost reversed due to the larger prefactor for the collision on Mg^{2+}. ($\Delta_{O-CO} = 0.361$ eV vs. $\Delta_{Mg-CO} = 0.358$ eV at $E_i = 0.3$ eV). Similar findings are made by Yamada and coworkers from scattering experiments of CO on LiF(001).[50] LiF has the same rock salt surface structure as MgO but lower ionic charges and shows a comparably weak gas-surface potential. They conclude, that scattering with the oxygen atom of CO experience a more elastic scattering, where the scattering induces only a small transfer of translational energy to the surface. Scattering of upwards oriented CO results more often in trapping and multiple collisions. The latter is in agreement with our simulations, which reveal a large translational energy loss for upwards CO, independently of the impact site.

4 | CONCLUSION

This works reports on simulations of state-resolved CO scattering from an ionic MgO(001) surface at normal incidence, as a case study for weakly interacting gas-surface system. A new global potential energy surface for the CO/MgO(001) system is adjusted to a modified reactive bond order force field form, which is parameterized to new reference energy values from periodic cluster embedding DFT-calculations. The shallow adsorption minimum of perpendicular CO atop a Mg^{2+} ion is close to the experimentally observed result. The optimized force field is highly accurate, capturing the subtleties of the weak gas-surface interaction up to potential energies of 1.2 eV above the potential minimum. The impact of energy transfer to the surface phonons on the scattering behaviour of impinging CO is investigated by further parametrizing the force field to include surface ion motion. Irreversible dissipation of the surface energy is included by damping the motion of the surface atoms, which are found to have relatively long lifetimes on the order of the picoseconds.

The scattering behaviour of CO molecules is found to depend strongly on the orientation of CO upon impact, especially for collisions around Mg^{2+}. An energetically more optimal Mg^{2+}–C–O alignment results in lower rotational excitation and smaller scattering angles. Parallel and downwards CO molecules shows larger rotational excitation and higher scattering angles. Energy transfer to the surface ions increases the probability of lower rotational excitation and smaller scattering angles, which correlates with the additional translational energy loss of CO towards the surface. This allows the thwarted CO molecules to adopt an energetically more optimal alignment during impact, leading to an even narrower distribution at lower final rotational states and scattering angles. At incident energies larger than the adsorption depth, energy transfer to the surface becomes less efficient and scattering behaves as though on a rigid surface.

The observed energy transfer is well predicted by the Baule model, as a subtle interplay between weak adsorption and energy transfer efficiency factors. While the mass ratio between CO and both surface ion types have a minor influence on the energy transfer rate, the potential depth for the different impact orientations mainly determines the energy transfer rate. The case of CO scattering from MgO(001), a surface with similar mass ratios for different impact sites, shows the importance of the potential energy topology on the scattering behaviour. An energetically optimal impact orientation amounts to late scattering with larger CO energy loss, lower rotational excitation, and smaller scattering angles. Early scattering for other orientations results in a larger energy transfer towards rotational and lateral movements. The findings demonstrate that the CO scattering from MgO(001) at

low incidence energies would provide a rich, yet challenging test systems for experimental measurements of weakly interacting gas-surface systems.

5 | ACKNOWLEDGEMENTS

References

1. Chorkendorff I, Niemantsverdriet JW. *Concepts of Modern Catalysis and Kinetics*. Wiley-VCH. 3rd ed. 2017.

2. Comsa G. Surface Scattering of Thermal Energy He Beams: From the Proof of the Wave Nature of Atoms to a Versatile and Efficient Surface Probe. *Surf. Sci.* 1994; 300: 77–91. doi: https://doi.org/10.1016/0039-6028(94)90647-5

3. Libuda J, Freund HJ. Molecular Beam Experiments on Model Catalysts. *Surf. Sci. Rep.* 2005; 57(7): 157–298. doi: https://doi.org/10.1016/j.surfrep.2005.03.002

4. Kleyn AW. Molecular Beams and Chemical Dynamics at Surfaces. *Chem. Soc. Rev.* 2003; 32: 87–95. doi: 10.1039/B105760J

5. Gerber RB. Molecular Scattering from Surfaces: Theoretical Methods and Results. *Chem. Rev.* 1987; 87(1): 29–79. doi: 10.1021/cr00077a003

6. Kroes GJ, Díaz C. Quantum and classical dynamics of reactive scattering of H_2 from metal surfaces. *Chem. Soc. Rev.* 2016; 45: 3658–3700. doi: 10.1039/C5CS00336A

7. Chadwick H, Beck RD. Quantum State-Resolved Studies of Chemisorption Reactions. *Ann. Rev. Phys. Chem.* 2017; 68(1): 39-61. doi: 10.1146/annurev-physchem-052516-044910

8. Jiang B, Yang M, Xie D, Guo H. Quantum Dynamics of Polyatomic Dissociative Chemisorption on Transition Metal Surfaces: Mode Specificity and Bond Selectivity. *Chem. Soc. Rev.* 2016; 45: 3621–3640. doi: 10.1039/C5CS00360A

9. Wodtke AM. Electronically non-adiabatic influences in surface chemistry and dynamics. *Chem. Soc. Rev.* 2016; 45: 3641–3657. doi: 10.1039/C6CS00078A

10. Golibrzuch K, Bartels N, Auerbach DJ, Wodtke AM. The Dynamics of Molecular Interactions and Chemical Reactions at Metal Surfaces: Testing the Foundations of Theory. *Annual Review of Physical Chemistry* 2015; 66(1): 399–425. doi: 10.1146/annurev-physchem-040214-121958

11. Huang Y, Rettner CT, Auerbach DJ, Wodtke AM. Vibrational Promotion of Electron Transfer. *Science* 2000; 290(5489): 111–114. doi: 10.1126/science.290.5489.111

12. Bünermann O, Jiang H, Dorenkamp Y, et al. Electron-Hole Pair Excitation Determines the Mechanism of Hydrogen Atom Adsorption. *Science* 2015; 350(6266): 1346–1349. doi: 10.1126/science.aad4972

13. Füchsel G, Cueto dM, Díaz C, Kroes GJ. Enigmatic HCl + Au(111) Reaction: A Puzzle for Theory and Experiment. *J. Phys. Chem. C* 2016; 120(45): 25760-25779. doi: 10.1021/acs.jpcc.6b07453

14. Somorjai GA, Carrazza J. Structure Sensitivity of Catalytic Reactions. *Ind. Eng. Chem. Fundam.* 1986; 25(1): 63–69. doi: 10.1021/i100021a009

15. Zambelli T, Wintterlin J, Trost J, Ertl G. Identification of the "Active Sites" of a Surface-Catalyzed Reaction. *Science* 1996; 273(5282): 1688–1690. doi: 10.1126/science.273.5282.1688

16. Füchsel G, Cao K, Er S, et al. Anomalous Dependence of the Reactivity on the Presence of Steps: Dissociation of D_2 on Cu(211). *J. Phys. Chem. Lett.* 2018; 9(1): 170–175. doi: 10.1021/acs.jpclett.7b03097

17. Bell AT. The Impact of Nanoscience on Heterogeneous Catalysis. *Science* 2003; 299(5613): 1688–1691. doi: 10.1126/science.1083671

18. Liu L, Corma A. Metal Catalysts for Heterogeneous Catalysis: From Single Atoms to Nanoclusters and Nanoparticles. *Chem. Rev.* 2018; 118(10): 4981–5079. doi: 10.1021/acs.chemrev.7b00776

19. Yoon B, Häkkinen H, Landman U, et al. Charging Effects on Bonding and Catalyzed Oxidation of CO on Au_8 Clusters on MgO. *Science* 2005; 307(5708): 403–407. doi: 10.1126/science.1104168

20. Hernández WY, Aliç F, Navarro-Jaen S, et al. Structural and Catalytic Properties of Au/MgO-type Catalysts Prepared in Aqueous or Methanol Phase: Application in the CO Oxidation Reaction. *J. Mater. Sci.* 2017; 52: 4727–4741. doi: 10.1007/s10853-016-0715-9

21. Julkapli NM, Bagheri S. Magnesium Oxide as a Heterogeneous Catalyst Support. *Rev in Inorg. Chem.* 2015; 36(1): 1–41. doi: doi:10.1515/revic-2015-0010

22. Haruta M. Size- and Support-Dependency in the Catalysis of Gold. *Catal. Today* 1997; 36(1): 153–166. Copper, Silver and Gold in Catalysisdoi: 10.1016/S0920-5861(96)00208-8

23. Stamatakis M, Christiansen MA, Vlachos DG, Mpourmpakis G. Multiscale Modeling Reveals Poisoning Mechanisms of MgO-Supported Au Clusters in CO Oxidation. *Nano Lett.* 2012; 12(7): 3621–3626. PMID: 22668206doi: 10.1021/nl301318b

24. Pacchioni G, Freund HJ. Electron Transfer at Oxide Surfaces. The MgO Paradigm: from Defects to Ultrathin Films. *Chem. Rev.* 2013; 113(6): 4035–4072. PMID: 23116191doi: 10.1021/cr3002017

25. Duriez C, Chapon C, Henry CR, Rickard JM. Structural Characterization of MgO(100) Surfaces. *Surf. Sci.* 1990; 230(1): 123–136. doi: 10.1016/0039-6028(90)90021-Y

26. Henry CR, Chapon C, Duriez C. Precursor State in the Chemisorption of CO on Supported Palladium Clusters. *J. Chem. Phys.* 1991; 95(1): 700–705. doi: 10.1063/1.461419

27. Henry CR, Chapon C, Duriez C. *Physics and Chemistry of Small Clusters*. 158. ch. Molecular Beam Relaxation Spectroscopy Applied to Adsorption Kinetics on Small Supported Catalyst Particles: 795–800; NATO ASI Series (Plenum Press, New York) . 1987.

28. Furuyama S, Fujii H, Kawamura M, Morimoto T. Physisorption of Nitric Oxide, Carbon Monoxide, Nitrogen, and Oxygen by Magnesium Oxide Powder. *J. Phys. Chem.* 1978; 82(9): 1028–1032. doi: 10.1021/j100498a014

29. Wichtendahl R, Rodriguez-Rodrigo M, Härtel U, Kuhlenbeck H, Freund HJ. Thermodesorption of CO and NO from Vacuum-Cleaved NiO(100) and MgO(100). *Phys. Status Solidi A* 1999; 173(1): 93–100. doi: 10.1002/(SICI)1521-396X(199905)173:1<93::AID-PSSA93>3.0.CO;2-4

30. Jian-Wei H, Estrada CA, Corneille JS, Ming-Cheng W, Goodman DW. CO Adsorption on Ultrathin MgO films Grown on a Mo(100) Surface: An IRAS Study. *Surf. Sci.* 1992; 261(1): 164–170. doi: 10.1016/0039-6028(92)90228-X

31. Colbourn EA, Mackrodt WC. A Theoretical Study of CO Chemisorption at {001} Surfaces of Non-defective and Doped MgO. *Surf. Sci.* 1984; 143(2): 391–410. doi: 10.1016/0039-6028(84)90549-1

32. Quintanar C, Caballero R, Castaño VM. Adsorption of CO on the Rumpled MgO(100), MgO(100):Ni, and MgO(100):Cr Surfaces: A Density Functional Approach. *Int. J. Quantum Chem.* 2005; 102(5): 820–828. doi: 10.1002/qua.20462

33. Illas F, Pacchioni G, Pelmenschikov A, et al. Comment on âĂIJFirst-Principles Determination of the Bonding Mechanism and Adsorption Energy for CO/MgO(001)âĂİ [Chem. Phys. Lett. 290 (1998) 255]. *Chem. Phys. Lett.* 1999; 306(3): 202–204. doi: 10.1016/S0009-2614(99)00410-8

34. Becke AD. Density Functional Thermochemistry. III. The Role of Exact Exchange. *J. Chem. Phys.* 1993; 98(7): 5648–5652. doi: 10.1063/1.464913

35. Lee C, Yang W, Parr RG. Development of the Colle-Salvetti Correlation-Energy Formula into a Functional of the Electron Density. *Phys. Rev. B* 1988; 37: 785–789. doi: 10.1103/PhysRevB.37.785

36. Töpfer K, Tremblay JC. First-Principle Investigations of the Interaction between CO and O_2 with Group 11 Atoms on a Defect-Free MgO(001) Surface. *J. Phys. Chem. A* 2018; 122(8): 2307–2317. PMID: 29389129doi: 10.1021/acs.jpca.8b00647

37. Xiao Y, Dong W, Busnengo HF. Reactive Force Fields for Surface Chemical Reactions: A Case Study with Hydrogen Dissociation on Pd surfaces. *J. Chem. Phys.* 2010; 132(1): 014704. doi: 10.1063/1.3265854

38. Brenner DW, Shenderova OA, Harrison JA, Stuart SJ, Ni B, Sinnott SB. A Second-Generation Reactive Empirical Bond Order (REBO) Potential Energy Expression for Hydrocarbons. *J. Phys. Condens. Matter* 2002; 14(4): 783–802. doi: 10.1088/0953-8984/14/4/312

39. CRC Handbook . *CRC Handbook of Chemistry and Physics, 85th Edition*. CRC Press. 85 ed. 2004.

40. Burow AM, Sierka M, Döbler J, Sauer J. Point Defects in CaF2 and CeO2 Investigated by the Periodic Electrostatic Embedded Cluster Method. *J. Chem. Phys.* 2009; 130(17): 174710. doi: 10.1063/1.3123527

41. Bahn SR, Jacobsen KW. An Object-Oriented Scripting Interface to a Legacy Electronic Structure Code. *Comput. Sci. Eng.* 2002; 4(3): 56–66. doi: 10.1109/5992.998641

42. Heo S, Cho E, Lee HI, et al. Band Gap and Defect States of MgO Thin Films Investigated Using Reflection Electron Energy Loss Spectroscopy. *AIP Adv.* 2015; 5(7): 077167. doi: 10.1063/1.4927547

43. Ahlrichs R, Bär M, Häser M, Horn H, Kölmel C. Electronic Structure Calculations on Workstation Computers: The Program System Turbomole. *Chem. Phys. Lett.* 1989; 162(3): 165–169. doi: 10.1016/0009-2614(89)85118-8

44. Treutler O, Ahlrichs R. Efficient Molecular Numerical Integration Schemes. *J. Chem. Phys.* 1995; 102(1): 346–354. doi: 10.1063/1.469408

45. Von Arnim M, Ahlrichs R. Performance of Parallel TURBOMOLE for Density Functional Calculations. *J. Comput. Chem.* 1998; 19(15): 1746–1757. doi: 10.1002/(SICI)1096-987X(19981130)19:15<1746::AID-JCC7>3.0.CO;2-N

46. Colbert DT, Miller WH. A novel discrete variable representation for quantum mechanical reactive scattering via the S-matrix Kohn method. *J. Chem. Phys.* 1992; 96(3): 1982–1991.

47. Shannon RD. Revised effective ionic radii and systematic studies of interatomic distances in halides and chalcogenides. *Acta Crystallogr. A* 1976; 32(5): 751–767. doi: 10.1107/S0567739476001551

48. Lončarić I, Füchsel G, Juaristi JI, Saalfrank P. Strong Anisotropic Interaction Controls Unusual Sticking and Scattering of CO at Ru(0001). *Phys. Rev. Lett.* 2017; 119: 146101. doi: 10.1103/PhysRevLett.119.146101

49. Groß A. *Theoretical Surface Science - A Microscopic Perspective*. Berlin Heidelberg: Springer Science. 2. ed. 2009.

50. Kondo T, Kato HS, Yamada T, Yamamoto S, Kawai M. Rainbow scattering of CO and N2 from LiF(001). *J. Chem. Phys.* 2005; 122(24): 244713. doi: 10.1063/1.1944729

Chapter 4

Summary

This chapter provides an overview of the results published in the papers presented in the previous chapter and shed light on their importance in the context of surface science. Our work can be classified into the field of heterogeneous single-atom catalysis, which focus on the catalytic potential of dispersed single atoms maximizing the efficiency of expensive and limited materials. Heterogeneous single-atom catalysis is a field of research that got increasing attention in the last years also due to improved possibilities in experimental synthesis and spectroscopy of such surface systems.[5,6,9,11–13] We have chosen a system that was found to be catalytically inactive to determine if it was possible to activate it by light, thereby opening the new field of single-atom photocatalysis.[169] Our efforts focused on mechanistic investigations to characterise the critical points of the potential energy surface responsible for this lack of reactivity. This was followed by model simulations of photoinduced dynamics, which revealed the necessity of full dimensional description due to the systems flexibility. This lead to the development of high-dimensional force fields for the catalytic system. We then proposed performing simple scattering experiments and spectroscopic measurements to evaluate the quality of the potential energy surface provided by the force field and probe the weak molecular interactions with the substrate. Despite not reaching the final goal of investigating single-atom photocatalysis, significant progress has been made on many fronts.

Paper A treated explicitly the reason, why single-atom catalysis of gold on a defective MgO(001) surface does not work, as it was already known from experiment.[33] The experiments show a limited catalytic activity for supported clusters containing 3 to 7 gold atoms and high activity for larger ones. The missing protection of the colour centre

by a single gold atom and dimer from the reparation by oxygen insertion was assumed to be the reason for the lack of catalytic activity. They might be not able to inhibit the insertion of atomic or molecular oxygen. Our calculation confirmed this hypothesis and provided the possible processes that lead to recovering a defect-free MgO(001) surface. Our simulations further quantified the associated reaction energies and activation barriers, allowing to identify the most likely mechanisms.

We considered each of the three possible charged colour centres F^0, F^{1+} and F^{2+} on a flat MgO(001) surface terrace. The neutrally charged F^0 is by far the most frequent one on a flat MgO(001) surface.[170] It has been shown, that the F^0 colour centre is also the most active in terms of adsorption strength to CO and O_2 and for the bond activation of the O_2. The single positively charged colour centre F^{1+} shows no binding interaction. This is in accordance to experiments of small neutral and negatively charged gold cluster in the gas phase,[171] where small gold clusters with an odd number of electrons show a larger interaction strength with O_2. A single gold atom with an odd number of electrons (79 e⁻) in combination with a F^{1+} colour centre behaves as a closed shell system. The high polarization of double positively charged F^{2+} colour centres has a long-range effect on the surrounding surface. This could not be fully covered by our periodic electrostatic embedding, where the position of the charges are fixed. Thus, it leads to a larger deviation from our predictions of the adsorption strength compared with previous work by Pacchioni and coworkers,[65] who have used a polarizable shell model. This allows for back-interaction of the cluster with the surrounding point charges. Despite the limitations in our theoretical description, our findings should be relevant to catalysis for the following two reasons: These two types of colour centres (F^{1+} and F^{2+}) represent a small minority of occurring vacancies on MgO(001) substrates and can become neutrally charged colour centres (F^0) by trapping further electrons.[170] Hence, the accurate description of the chemical processes happening on the neutral colour centre F^0 can be seen as the most important one.

The accurate description of the F^0 colour centre is demonstrated by good agreements for the ionization potential of the defect site and the adsorption strength of CO on $Au_1@F^0$-MgO(001) with previous theoretical work. In general our investigations reveal the trend, that CO energetically adsorbs more strongly on a positively charged gold atom while O_2 prefers negatively charged gold atoms. This appears as a negative property of the system at first glance since both reactants are not similarly stable on the gold atom for different charged states. On the other hand, both CO and O_2 can be co-adsorbed

on positively up to negatively charged gold atoms to form multiple and metastable states.[172,173] It is this metastability that usually confers catalytic potential to a given system.
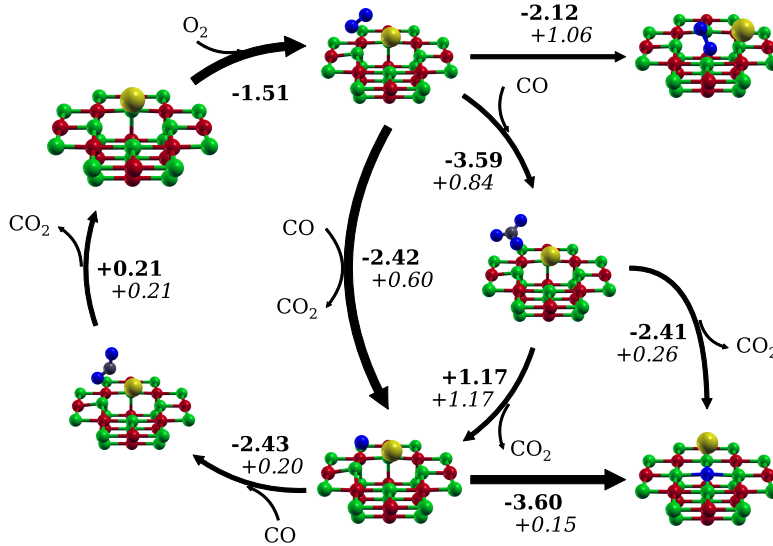

Figure 4.1: Catalytic cycle for the oxidation of CO on $Au_1@F^0$-Mg(001) and possible termination reactions determined from NEB calculations. Bold arrows denote the most likely reaction paths. The reaction energy is calculated as the difference between initial and final state used in the NEB calculation, corrected for the adsorption energy of the reactants. Potential difference (bold) and activation energies (italic) are given in eV.

The chemistry of a single gold atom adsorbed on a F^0 colour centre of a MgO(001) surface shows a large variety when subject to a mixed atmosphere of CO and O_2 gas, as it is illustrated in figure 4.1. The large adsorption strength of a single gold atom on the neutrally charged colour centre (2.64 eV) prevents the immediate insertion of molecular oxygen into the vacancy by a large energy barrier (1.06 eV). In the unlikely event this might happen, the additional two electrons located in the colour centre will strongly weaken the oxygen bond and enable the CO_2 formation from an incoming CO molecule. In general, lower energy barriers are found for the sequential dissociation-reparation reaction (0.60 eV) and the formation of a carbonate intermediate (0.84 eV).

The energy barrier for the formation of the carbonate state is the larger of the two. It is followed by the dissociation of CO_2 while the remaining oxygen atom moves into the vacancy and restores the clean MgO(001) surface. The reconstruction of a defect-free

MgO(001) is an important contribution for the low reaction barrier as it can be seen, that a sequential dissociation and reparation process have a much higher energy barrier. Such carbonate states are also reported for larger gold clusters in other theoretical works and are supposed to act as a catalyst poison due to the high activation barrier for the dissociation of CO_2.[64,174] Noteworthy is also the small angle between the plane of the carbonate intermediate and the surface plane which is not observed for defect-free MgO(001) surfaces. CO and O_2 could also form a carbonate state on defect-free Au_1@MgO(001) systems, where a perpendicularly aligned CO_3 plane is energetically favoured. The change from a perpendicular orientation on a bulk MgO(001) surface to a more parallel one on electron rich surfaces as seen around F^0-MgO(001) or at thin MgO(001) films on metal support was also reported previously.[175]

In the case of a direct dissociation of CO_2 without the formation of a carbonate state a single oxygen atom remains next to the gold atom atop a Mg^{2+} ion. The insertion process has such a small energy barrier, that the reparation of the vacancy cannot be inhibited. At the end the colour centre is consumed after the formation of one CO_2 molecule. The oxidation process on a gold atom supported by a defect-free MgO(001) will have a much higher reaction barrier such that the formation of further CO_2 molecules is kinetically hindered.

Colour centres on MgO(001) surfaces are created under harsh conditions by electron bombardment.[170] The strong Coulomb interaction between the doubly charged ions of the MgO substrate prevents any vacancy formation following a „chemical“ approach. This statement might seem obvious, but it was reported that the catalytic oxidation of CO on a single gold atom supported by CeO_2(111) surfaces proceeds via the formation of an oxygen vacancy.[16] For the present system, the reparation of the vacancy remains energetically favourable for larger gold cluster. The larger cluster size and the stronger, more rigid binding to the surface will kinetically inhibit the reparation process.

The major contribution of the colour centre is the provision of additional electron density to weaken the bond within adsorbed O_2. This electron transfer can also be observed for ultra-thin MgO(001) surfaces deposited on a metal support like Mo(001) or Ag(001). It is even stated that the O_2 bond is sufficiently weakened for the oxidation of CO by an ultra-thin MgO(001)/Ag(001) surface alone without a metal adatom.[176] The activation barriers for the CO oxidation on a single gold atom supported by defect-free bulk MgO(001) surfaces are too high to be reached thermally. The temperature is restricted by

the diffusion barrier of a single gold atom, which is experimentally determined between 0.2 eV and 0.3 eV.[57,177] The conglomeration of gold atoms to larger clusters however is estimated to have a reaction barrier twice as large as the diffusion barrier. The height of the diffusion barrier is in agreement with EPR experiments[178] where the resonance signal of gold's unpaired $6s^1$ electron changes as a function of the temperature. They observed a narrowing of the signal at 85 K and the decrease of the signal intensity above 125 K. At 85 K gold atoms are able to overcome the diffusion barrier and begin to rearrange on the MgO(001) surface, minimizing their repulsive interaction against each other probably due to spin-spin interactions between the single gold atoms. The rearrangement into a more dispersed coverage on the surface yields a narrower EPR signal due to weaker disturbance by spin-spin interactions. This also explains the additional barrier for the conglomeration towards larger gold nano-clusters, as seen by the vanishing of the signal at higher temperatures. Using our calculation setup the diffusion barrier of a single gold atom is well reproduced at 0.27 eV. From the results presented in **paper A**, it becomes clear that single-atom catalysis on gold cannot take place on defective MgO(001) surfaces.

Paper B covers the interaction of CO and O_2 with group 11 metal atoms on a defect-free bulk MgO(001) surface. Defect-free MgO(001) surfaces are less favourable for the adsorption of metal adatoms but they represent the only possible route for single-atom catalysis and its photocatalysis analogue. We extend our investigation to copper and silver atoms to gain deeper insights in the interaction of $ns^1(n-1)d^{10}$ transition metals. In general, group 11 transition metals show a stronger affinity for O_2 than CO. While CO is adsorbed the strongest on copper (0.65 eV) and weakest on the silver atom (0.18 eV), O_2 shows a generally stronger adsorption but keeps the same order, binding strongest to the copper atom (1.70 eV) and weakest to silver (0.91 eV). The large increase in adsorption strength from CO to O_2 for the three metal types becomes clearer from energy decomposition analysis. The different ratios of the electrostatic and orbital-relaxation contributions indicate a stronger ionic bond character of the CO-Cu@MgO(001) interaction, while CO on Au@MgO(001) is bonded more covalently, which is in accordance to copper's larger polarizability than gold's.[179,180] The contributions for the CO-Ag@MgO(001) interaction energy are much smaller than for those of the other metals. That correlates with the larger atomic radii of silver than for copper or gold[181] and implies a softer, more diffuse bond. In contrast to CO, O_2 has an electronic triplet ground state which causes the large differences in the adsorption behaviour. While CO is only slightly tilted on the metal atom to have a non-zero overlap between the ns^1

electron of the metal and the π orbitals of CO, O_2 is strongly tilted to maximise the overlap of one of its π^* molecular orbitals with the ns^1 orbital of the metal atom. Due to the different spin state of the π^* molecular orbitals and the ns^1 metal electron their overlap does not affect Pauli repulsion as it can be seen at the lower exchange-repulsion contributions for the supported metal-O_2 bonds than the metal-CO bonds. An exception is the O_2-Ag@MgO(001) system, where the exchange-repulsion contribution is higher because of the much shorter equilibrium bond length between the silver atom and O_2 than silver and CO. The adsorption strength between the supported silver atom and O_2 is larger by a factor of five as between silver and CO. For gold and copper, it increases only by a factor of two and three, respectively.

The strong bonding of O_2 to the metal atom leads to a longer O_2 bond of an adsorbed oxygen molecule with more than > 1.3 Å as compared to the equilibrium bond length of O_2 in the gas phase with 1.208 Å.[182] Such behaviour fits to the calculated atomic charges showing a large polarization by a strongly positively charged metal centre and negatively charged oxygen atoms, caused by the electron transfer from the metal to the anti-bonding π^* orbitals of O_2.
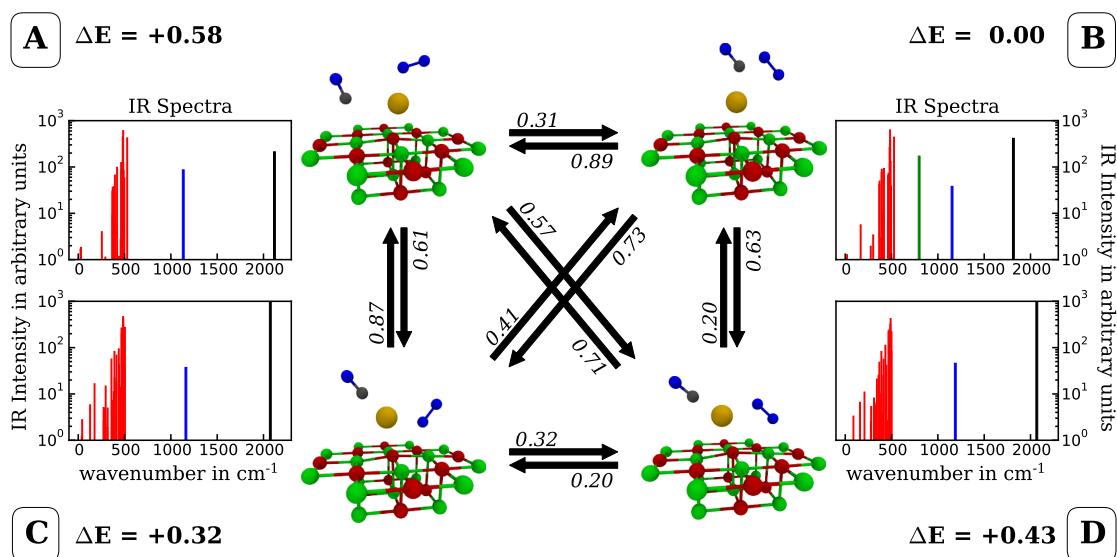

Figure 4.2: Different conformers for the co-adsorbed CO and O_2 on Au@MgO(001). The total energy ΔE and activation barriers for the conformer conversion (italic) are given in eV. The peaks in the IR spectra belong to calculated vibrational modes of the respective conformers.

Figure 4.2 shows four stable conformers of CO and O_2 on a single supported gold atom, all representing local minimum structures. These conformation are found for the co-

adsorption on silver and copper atoms as well but at different relative energies and having different activation barriers for the conformer conversions. If O_2 is already adsorbed atop the metal atom, the interaction with CO is rather weak and most energetically favourable atop one Mg^{2+} ion next to the metal atom. If CO is adsorbed atop the metal atom, O_2 can take several stable adsorption sites as it is shown with conformer **B**, **C** and **D**. Except for conformer **A**, the adsorption energies for CO and O_2 are higher than in the case of the adsorption of single molecules, showing an important cooperative effect between both gas molecules and the metal atom. This is further underlined by the adsorption sites of O_2 in the conformers **C** and **D**, which become a local minimum by placing a CO molecule on the opposite side of the metal atom. In the absence of CO, O_2 converges towards the conformation of a single adsorbed O_2 molecule during the structure optimization. The cooperative effect can be also understood by energy decomposition analysis. It reveals an increased energy gain for the orbital relaxation if CO is co-adsorbed, resulting into a potential minimum for O_2 at this adsorption sites. Conformation **B** can also be found in the gas phase structure for CO and O_2 on a gold atom and presents a good precursor state for a CO_2 formation reaction.[172]

While conformation **B** is the most stable on the gold atom, the energy of the conformers **B**, **C** and **D** are quite close in range within 0.05 eV on the supported silver atom. On supported copper atoms, conformers **C** and **D** are the energetically most stable ones and conformation **B** is about 0.41 eV higher in energy. The activation barriers for the conversion between the conformers are the lowest in the copper system and the highest for gold but would probably still allow the conversion towards the respective energetically lowest conformation.
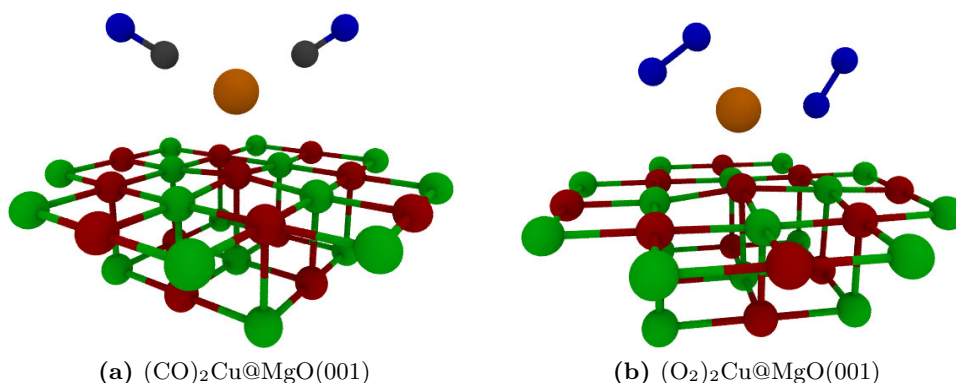

(a) $(CO)_2Cu@MgO(001)$ **(b)** $(O_2)_2Cu@MgO(001)$

Figure 4.3: Most stable confomers for respectively two co-adsorbed (a) CO or (b) O_2 molecules on Cu@MgO(001).

We have also considered the co-adsorption of two CO or O_2 molecules instead. Gold and silver atoms are not capable of adsorbing two molecules simultaneously with comparable strength, as for the mixed adsorption case. The energetically most stable co-adsorbed situation is either the first CO or O_2 molecule adsorbed atop and the second one next to the metal atom on a Mg^{2+} ion. Figure 4.3 shows stable configurations on the supported copper atom, where either two CO or O_2 molecules are strongly adsorbed. Two CO molecules energetically prefer to form a trigonal planar configuration with the copper atom and the underlying O^{2-} ion, where the plane is perpendicular to the surface. The adsorption energy of a second CO molecule (0.52 eV) is about 1 eV lower in energy than the adsorption of a O_2 molecule (1.56 eV), if we regard the respective most stable conformation **D** for mixed co-adsorption on the supported copper atom. Two O_2 molecules take the positions as O_2 in conformers **C** and **D** on the opposing site of the copper atom. The adsorption of a second O_2 molecule yields no energy gain (≈ 0 eV), while a CO molecule shows an adsorption strength of 0.49 eV. Regarding the adsorption energies, these homomolecular co-adsorbed conformations are energetically less stable than the mixed co-adsorbed conformers on the copper atom, but they could still be kinetically stable as the energy barriers for substitution reaction are not determined.

Figure 4.2 further present the calculated IR spectra of the four shown conformers. The red peaks correspond to the lower fingerprint spectra while the blue and black peak denotes the intensity and frequency of the O_2 and CO stretch vibrations, respectively. For all given conformers, the frequency of the O_2 stretch vibration remains almost unchanged around 1160 ± 30 cm^{-1}. That is about -380 cm^{-1} below the O_2 gas phase vibration frequency of 1580 cm^{-1}.[183] The red-shift in the co-adsorbed case is lower than in the single adsorption of O_2 on the supported gold atom with -450 cm^{-1} but still high and relatively constant over all the given characteristic conformations. Regarding the frequency shift in CO, it shows an even larger red-shift by -380 cm^{-1} of its stretch frequency in conformer **B** than in its optimised single-adsorbed structure. The red-shift is much weaker in all other shown conformers, due to either a larger distance to the gold atom as in conformer **A**, or an almost linear alignment to the gold atom as in conformer **C** and **D**. As mentioned above, a linear alignment will not support the π-back donation from the golds $6s^1$ orbital to the anti-bonding π^* molecular orbitals of CO, which is the origin of the C-O bond weakening and decreases the frequency of the stretch vibration. The green peak in conformer **B** belongs to the OC-O_2 vibration corresponding to the reaction path which leads to the formation of CO_2. The minimum energy path for the CO_2 formation are determined by NEB calculations and results into reaction barriers of

1.19 eV on the supported gold atom. This is clearly thermally unaccessible regarding the energy barriers for diffusion and conglomeration of single gold atoms to larger nano-cluster. The analogous reaction barrier on supported copper and silver atoms are lower in energy with 0.65 eV and 0.72 eV, respectively. However, the calculated diffusion barrier for silver on MgO(001) of 0.15 eV and the slightly higher conglomeration barrier will not prevent any aggregation of the silver atom. Further, the initial conformation **B** on supported copper atoms is energetically much less stable and unlikely to be populated in practice. For the sake of completeness, the calculation yields a barrier of 0.44 eV for the diffusion of a single copper atom atop MgO(001), comparable to the reaction barrier for CO_2 formation.

As for the gold atom on a defective F^0-MgO(001) surface there exists an energetically highly stable carbonate structure for the defect-free system as well, with the qualitative difference that the CO_3 plane lies perpendicular to the surface. If the carbonate state would be formed on a supported gold atom, the dissociation of CO_2 would be also very unlikely within the possible reaction conditions, as it was also found for larger gold clusters.[64,174] In any case, this issue would unlikely to be observed in practice due to the high reaction barrier for the formation of the carbonate state. The activation barrier is of the same order of magnitude as the reaction barrier for the CO_2 formation starting from conformer **B** of figure 4.2. This makes also sense in the way, that if a single gold atom on a defect-free MgO(001) surface is not capable of weakening the O_2 bond as much as necessary to lower the activation barrier for the bond breaking, why should it be any different for the formation a carbonate specie. First NEB calculations confirm a large reaction barrier larger than > 1 eV. Hence, further investigations of this reaction path were not pursued.

A promising strategy to initialise CO_2 formation starting from conformer **B** is the specific excitation of vibration by light. Pumping energy selectively along one bond could allow to bypass the thermal activation barrier and favour the photocatalytic reaction over the diffusion and aggregation of metal clusters. The well isolated vibrational mode of the OC-O_2 fragment on the supported gold atom seems to be a suitable target for a specific excitation with infrared light. The excitation process can be simulated by quantum dynamical methods, which first needs a potential energy surface representative of the system. Due to the complexity of quantum dynamical methods, only a reduced number of dimensions can be studied. The potential should thus contain the most important degrees of freedom. Intuitively, that are the distances between the carbon atom and

the closest oxygen atom of O_2 as well as the O_2 bond. Both dimensions would cover the CO_2 formation and the O_2 bond breaking, respectively. Unfortunately, a proper potential energy surface covering the catalytic oxidation of CO by O_2 on a supported gold atom crucially depends on more than these two degrees of freedom. The reaction barrier highly correlates with the position of the second oxygen atom of O_2, which should remain adsorbed to the gold atom after CO_2 leaves. If the oxygen stays unbound and isolated, the reaction barrier will be dramatically higher in energy. On the other hand, the adsorption of the remaining oxygen atom is energetically not favourable if the carbon atom stays close to the gold. Thus, the reaction path can be summarised as the simultaneous (1) bond formation between the carbon atom and the closest oxygen atom of O_2, (2) bond breaking of O_2, (3) adsorption of the remaining oxygen atom of O_2 to the gold atom and (4) desorption of the C atom by the desorption of the formed CO_2 molecule. At least four degrees of freedom are required to minimally describe the seemingly easy process of CO_2 formation. The description of the strongly correlated motion of atoms is not a trivial task. The quantum dynamics simulation on 1-dimensional potentials does not need any consideration of the coupling between the degrees of freedom and the coupling of motions on a 2-dimensional potentials is trivial. It becomes complicated for three dimensions but still feasible by using, for example, Jacobi coordinates, and extremely hard for more than that. This exponential scaling of the numerical cost of quantum dynamical methods is known as the „curse of dimensionality".
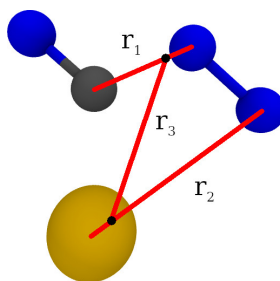

Figure 4.4: Sketch of adsorbed CO and O_2 molecules on a gold atom in the gas phase. The red lines denote the chosen Jacobi coordinates r_1, r_2 and r_3 to describe the relative movement within the system. The position of the oxygen atom of CO is relaxed for each configuration defined by the three Jacobi coordinates. The black dots mark the centre of masses on the respective coordinates r_1 and r_2.

One cost effective way to tackle the quantum dynamics of a multidimensional system is by using the multi-configuration time-dependent Hartree (MCTDH) method.[184,185] We attempted to describe the reaction by a three dimensional potential surface using Jacobi coordinates as shown in figure 4.4. It is to mention, that coordinate r_1 in figure

4.4 is further simplified by originating from the carbon atom and not the centre of mass of the CO molecule. A set of 3-dimensional reference data, reduced from a 5-dimensional adiabatic potential energy scan of the CO and O_2 on a single gold atom in the gas phase, was used to fit a model potential energy surface for the system. The gas phase system also sustains similar initial co-adsorbed states like conformer **B** of the co-adsorbed state, and comparable reaction paths are also observed. In the framework of an internship, we have fitted a three-dimensional potential energy function and performed dynamic simulations with different initial conditions using the MCTDH method. The simulations revealed the possibility of CO_2 formation at a sufficient levels of vibrational excitation. However, the reduced dimension potential energy surface was found to only reproduce qualitatively the *ab initio* data due to strong intermode coupling. The potential energy surface is not able to cover all the necessary degrees of freedom of the real system.

The unfavourable scaling of quantum dynamical simulation methods and the limitation of the reduced-dimension model bread the need for a suitable approach for describing the system. Here, we thus proposed to define a global full-dimensional force field for the reaction and perform quasi-classical molecular dynamics simulations for various processes involved in the catalytic cycle. Such a force field must be able to cover the O_2 bond breaking and the formation of CO_2, respectively. A reactive bond order force field (REBO-FF) is often represented as a sum of two-body interaction potentials describing the bonds, affected by three-body terms describing the chemical environment of these bonds. We have chosen the REBO-FF proposed by H. F. Busnengo and coworkers and fitted the parameters of the force field following a stepwise procedure from smaller systems to the larger and more complicated ones. During the process we modify the form of the three-body terms, which consider the influence of the chemical environment atom-wisely on the interaction between two atoms as a function of their distance and angle. The description of the interaction between CO and a clean MgO(001) surface was achieved with a high accuracy, up to more than 1 eV above the global potential minima. The dissociation limit of CO on a MgO(001) surface is experimentally found to be about 0.14 eV.[82] The determination of the adsorption energy and accurate modelling by quantum mechanical methods have taken a decade due to the difficulties in describing weak interaction strengths.[84,85,186,187] Our final parameter fit of the REBO-FF are able to reproduce the correct minimum conformation of CO adsorbed perpendicularly atop a Mg^{2+} ion with a potential minimum of 0.17 eV. As the next step towards the full-dimensional force field for the catalytic reactions the interaction potential of CO around a single gold atom supported by the MgO(001) surface was fitted using the REBO

form. However, the accuracy was not sufficient enough to describe the molecule in the entry channel and at higher energies above the global minimum of the potential energy surface. This is due to the rigidity of the REBO-FF functional form, which only contain up to three-body interactions. Future refinements of the potential energy surface will require a more sophisticated form for the chemical environment, which can be achieved using machine learning strategies such as deep neural networks.[188–191] Nevertheless, to unravel intermode coupling in the vicinity of the surface, high-dimensional vibrational spectroscopic analysis of CO on the clean MgO(001) surface and on the deposited adatom has been performed. The results are preliminary and the method is beyond the scope of the present thesis. Thus, discussion of the effect of the surface nanostructuring on vibrational modes will be postponed to later. As a preview, it appears that the frustrated rotations, the translations, and the surface mode (the CO-surface motion) are strongly mixed in the vicinity of the adatom. These could be directly probed experimentally to reveal the nature of the molecule-surface interaction.

In order to assess the quality of the REBO-FF for the CO-MgO(001) interaction, we investigated the scattering of CO from the surface, simulating state-of-the-art molecular beam experiments. Since the interaction of CO with MgO(001) is very weak, the simulations provide a stringent test for the force field.

In many scattering simulations of diatomic molecules on a periodic surface the potential energy surface is described using spherical coordinates for the internal degrees of freedom of the molecule, and the distance of its centre of mass to the surface. It further uses the two-dimensional periodicity parallel to the surface, which must be accounted for during molecular dynamics simulation. This prevents the consideration of the surface atom movement which are important to dissipate collisional energy. Our force field is based on two-body interactions weighted by the surrounding atoms and is not bound to a perfect periodicity of the surface structure during the simulation. It is thus to include surface atom movement in the molecular dynamics simulations of CO scattering from a defect-free MgO(001) surface. The impact on the scattering simulations is expected to be large due to the similar masses of CO and the surface atoms. it is known that coupling to surface phonons decreases for large mass differences between surface atoms and incident molecules. Similar effects have been observed in scattering experiments of light gas molecules on heavy metal surfaces.[192–194] Further, in grazing incidence diffraction experiments with incident energies in the range of kilo electron volt,[195] reduced coupling to surface phonons is also observed. All these phonon couplings can be

included in our simulations, which render our prediction of state-to-state scattering more accurate.

Another type of coupling that could affect the scattering simulations, whose impact is strongly debated in the literature,[196] is the electronic friction due to the creation of electron-hole pair in the substrate by non-adiabatic interactions with fast moving molecules. Electronic friction acts a damping force on the movement of the gas molecules, which is strong in the vicinity metallic substrates with energetically close electronic states.[197] In recent years, the theoretical computation of the friction coefficients[198,199] and the impact on slow and vibrationally cold gas molecules[200–202] have been hotly discussed. The clean MgO(001) surface, in contrast, has a bandgap of about 7.1 eV.[203,204] it will experience negligible electronic friction, especially for low incident energies used to probe the weak interaction with the surface.
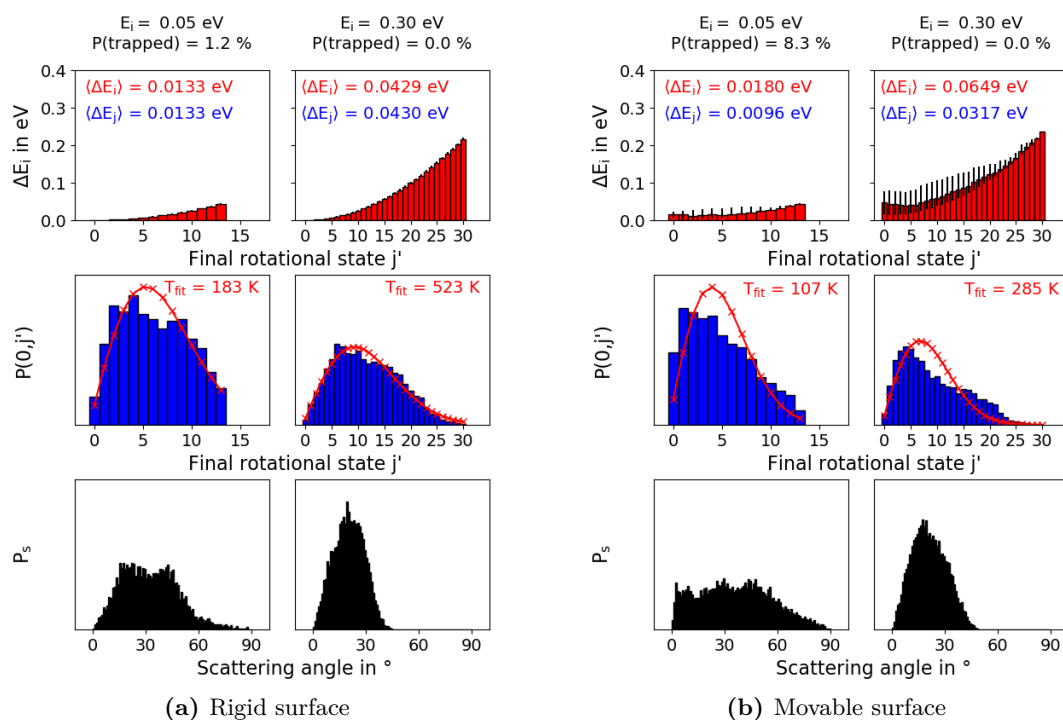

Figure 4.5: Scattering of $CO(\nu = 0, j = 0)$ from a (a) rigid and (b) movable MgO(001) surface at different initial translation energies $E_i = 0.05, 0.30$ eV. Top panels: State-resolved translational energy loss. The average translational energy loss ($\langle \Delta E_i \rangle$) and average rotational energy gain ($\langle \Delta E_j \rangle$) are given in red and blue, respectively. Central panels: Rotational excitation probability, $P(0, j')$, and best fit to a Boltzmann distribution (red line). Bottom panels: Scattering angle probability distribution P_S.

Paper C shows the results for the molecular dynamics simulations of CO scattering on a clean MgO(001) surface. We focused on the state-to-state scattered products for the molecules initially prepared in the first lowest ro-vibrational states ($\nu = 0$, $j = 0, 1$), at different initial translation energies for CO impinging at normal incidence. The results show the importance of the energy transfer from the impinging CO molecule to the surface atoms and the anisotropy of the potential for the upwards and downwards orientations of CO relative to the surface.

Figure 4.5 shows the translational energy loss, the rotational excitation probability, and the scattering angle distribution for scattered CO molecules initially in the ro-vibrational ground state ($\nu = 0$, $j = 0$) on either rigid or movable MgO(001) surfaces. The energy transfer to the surface leads to a larger expectation value for the translational energy loss $\langle \Delta E_i \rangle$ and, consequently, a larger trapping probability for the lower impact energies. We further observe a lower excitation probability to higher rotational states. While the distribution of the rotational excitation probability becomes closer to a Boltzmann distribution for higher impact energies, the distribution on a movable surface still shows a larger deviation from the thermal behaviour. It is to mention, that no vibrational excitation has been seen for all trajectories with the covered impact energies. The scattering angles on a rigid surface reveals a tighter distribution than on the movable one. The two peaks at $20°$ and $40°$ in the scattering angle distribution on the rigid surface and the lowest impact energy can be also found at the movable surface but with a larger spread around $10°$ and $50°$. As we can see in figure 4.6, these peaks originate from different alignment of CO during the impact. In general, the results of CO scattering on a rigid and movable surface become closer at higher impact energies, especially for the scattering angle distribution. The rotational excitation probabilities converge as well but in a slower pace. The decreasing impact of energy transfer to surface phonons is in agreement with the experimental observation mentioned above.

Figure 4.6 shows the rotational excitation probability and the scattering angle distribution for scattered CO molecule in the ro-vibrational ground state ($\nu = 0$, $j = 0$) broken down by impact site around Mg^{2+}, O^{2-} and at hollow sites. The two peaks in the scattering angle distribution for small impact energies are caused by CO scattered from Mg^{2+}. When CO hits the surface in an upwards orientation with the carbon atom first ($\Theta = 0°$), CO gets a smaller deviation from its initial normal incidence (or small scattering angle). Alternatively, when CO hits the surface downwards with the oxygen atom first ($\Theta = 180°$), it scatters at larger angles. This behaviour can be observed for
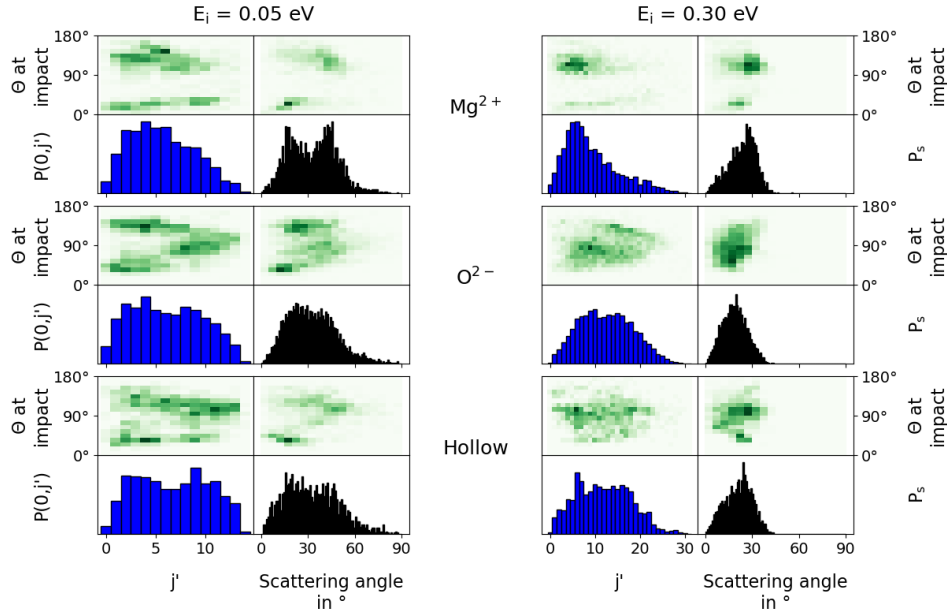
(a) Rigid surface
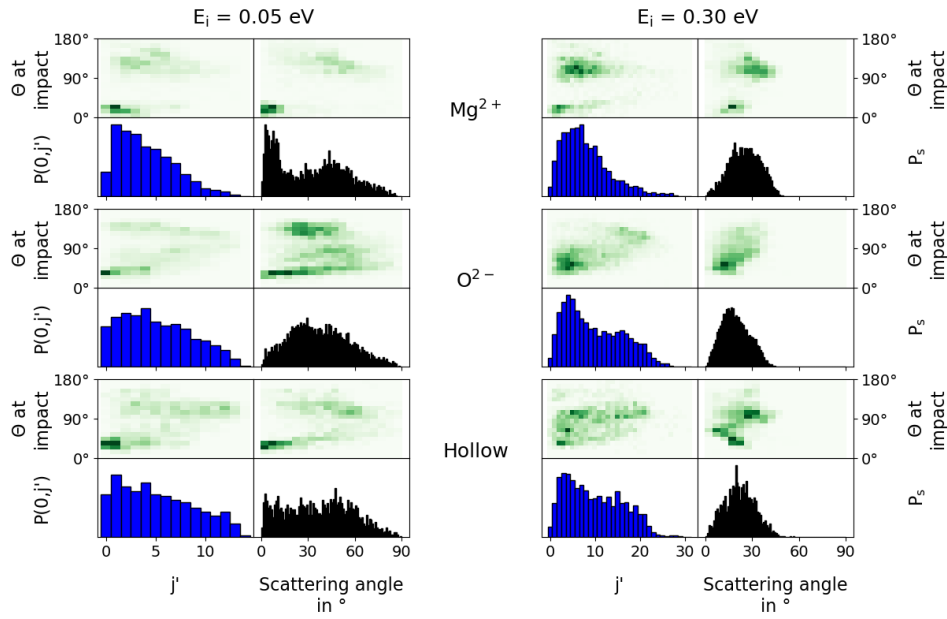
(b) Movable surface

Figure 4.6: Influence of the impact site and of molecular orientation on the j-resolved rotational excitation probability $(P(0, j'))$ and the scattering angle distribution P_S. $CO(\nu = 0, j = 0)$ is scattered from a rigid surface at different initial translational energies $E_i = 0.05, 0.30$ eV. Results for areas belonging to Mg^{2+}, O^{2-}, and hollow sites are respectively depicted from top to bottom.

99

CO scattered on O^{2-} and hollow sites as well, but less pronounced. The perpendicular alignment of the CO molecule at the impact, especially around Mg^{2+}, is caused by the strong repulsive interaction between the carbon atom of CO and the O^{2-} ions. The interaction between the oxygen atom of CO and the O^{2-} is also repulsive but weaker in comparison. This correlates with the topology of the potential energy surface. As a consequence, CO has a higher probability of hitting the surface in its downwards alignment, as the analysis of the trajectories has shown. The rotational excitation probability on a rigid surface is thermally distributed for CO scattered on Mg^{2+} and more uniformly distributed elsewhere. When the energy transfer to movable surface atoms is allowed by rendering the surface movability, we can observe a general decrease for the probability of higher rotational excitation. More interesting is the strong correlation of low rotational excitation with CO hitting the surface in an upward alignment, around $\Theta \sim 0°$. A more upward alignment also leads to a larger loss of translational energy as observed in the time of flight spectra (not shown here). These observations are in agreement with the extended Baule limit model,[151] that provides a simple relation to estimate the energy loss Δ by a scattered molecule from a surface. As equation (4.1) shows, the energy loss depends on the mass ratio between gas molecule and surface atoms, $\mu = M_{\mathrm{gas}}/M_{\mathrm{site}}$, and the sum of the adsorption E_{ads} and impact energy E_i, corrected by the thermal energy which is $T_{\mathrm{surf}} = 0$ K in our simulations.

$$\Delta = \frac{4\mu}{(1+\mu)^2}\left(E_i + E_{\mathrm{ads}} - \frac{1}{2}k_B T_{\mathrm{surf}}\right) \tag{4.1}$$

CO shows a larger adsorption energy for CO on Mg^{2+} in an upward orientation than in its downward orientation (0.17 eV and 0.06 eV in accordance with the REBO-FF, respectively). Thus, upward CO is supposed to exhibit a higher energy transfer to the surface. That correlates with the higher translational energy loss and lower rotational energy gain observed in the MD simulations. The observation also holds for CO scattering on O^{2-} and the hollow site because of lower potential energy for tilted CO when the C atom points towards the Mg^{2+} ion. That also explains the large peak of CO molecules having a $\Theta = 45°$ alignment during the impact around O^{2-} and the hollow site. The opposite Mg^{2+}-O-C alignment has a negligible, attractive interaction strength that will not favour the energy transfer towards the surface. The influence of the interaction strength between CO and surface decreases with larger impact energies, as the Baule model predicts. The already weak interaction strength becomes marginal for higher values of the impact energy E_i, which dominates the sum in equation (4.1). This is in agreement with the observations made at higher impact energies for CO.

An initial small rotational momentum of CO does not qualitatively change the outcome of the scattering. When CO has a rotational moment solely along the Θ angle, as it is the case in the initial ro-vibrational state $\nu = 0$, $j = 1$ and $m_j = 0$, the probability of an impact in a downward orientation of CO increases and results in a larger, narrower peak for low scattering angles at low impact energies. CO in the initial ro-vibrational state $\nu = 0$, $j = 1$ and $m_j = \pm 1$ has an additional initial rotational momentum along the Φ angle, and the peak in the distribution at smaller scattering angles becomes broader. Differences in the rotational excitation probability can be observed but they are too small and randomly distributed to see a clear and distinct pattern. Again, the differences become vanishingly small for larger impact energies.

The literature we have seen so far does not provide any comparable experiments or simulations of CO scattering on a bulk MgO(001) surface. MgO(001) is an experimentally frequently used support material due to its easy preparation and stability, but scattering experiments on MgO(001) are widely done with noble gas atoms and hydrogen molecules.[205–210] An interesting comparison can be made with the scattering experiments of CO and N_2 on a LiF(001) surface by T. Yamada and coworkers.[211] They reported an anisotropic scattering behaviour of CO similar to the one showed here. LiF and MgO are comparable in their the rock-salt structure and large bandgap, which qualifies both as insulators. As on MgO(001), the energetically lowest adsorption configuration is upwards, with CO perpendicular atop of the Li^+ cation. An even weaker adsorption strength of about 0.085 eV[212] is found probably due to the lower ionic charges. They found, similar to our simulation results, different scattering behaviour of CO in dependence of their impact orientation. The scattering with the oxygen atom of CO experience a more elastic scattering like that of a heavy sphere, where the scattering induces only a small transfer of translational energy to the surface. The scattering of upwards oriented CO results more often in trapping and multiple collisions. This finding is in agreement with the large translational energy loss for upwards CO independently of the impact site as we have observed in our simulations.

Our scattering simulations extend the general understanding of weak molecule-surface interactions. First, the results are comparable to other findings from CO scattering on ionic surfaces of insulators, where the weak interaction is mostly caused by electrostatic interactions between the ionic surface and the molecules polarizability. The state-resolved analysis provides deep insight in the correlation between gas-surface interaction and scattering results, which are in agreement with established energy transfer models such

as the Baule limit model. Our results offer a prediction of the systems behaviour, which should be compared with experiments. This system is perfectly suited for both state-to-state scattering and molecular beam experiments due to the great stability of MgO(001) surfaces in mixed atmospheres. It is to note that simulations of molecular beam experiments would require a different definition of initial conditions (temperature, velocity), which is well within the possibilities of the current computational setup.

The theoretical framework of the embedded MgO(001) surface cluster is versatile and can be used for the description of other surface processes. For example, as we have already done for the simulation of the diffusion of single group 11 metal atoms on MgO(001), only a few changes were necessary to further simulate the diffusion of diatomic metal clusters. The calculated electron densities during these diffusion processes are used as a reference for the improvement of imaging techniques, which we propose to use for probing the dynamics with high energy, space, and time resolution. In collaboration with G. Dixit from IIT Bombay, we investigated ideas to use a low-pass Fourier filter to visualise the valence electron density from time-dependent X-ray scattering signals. X-ray diffraction is an important visualization technique that is usually used to determine the atomic, molecular crystal structures. Recent developments in the field of high-intensity free-electron lasers[213–215] have increased the time and space resolutions of X-ray techniques, allowing to probe chemical reactions on the femtosecond timescale by measuring time-delayed snapshots of the electron density. This techniques already allows to resolve the three-dimensional atomic structure of single biological macromolecules without the need for crystallization.[216,217] Typically, only a few valence electrons participate in bond breaking and formation reactions but the X-ray scattering signal is strongly dominated by the core electron density. Thus, advanced data-processing methods are needed to separate the information of the valence electrons from the strong background of the highly localised core electrons. According to the Heisenberg uncertainty relation, the strong localization of the core electrons in space leads to a broad distribution in momentum space, while the more delocalised valence electrons shows a narrow distribution at low momentum values. We thus tried using a low-pass Fourier filter to remove the contribution of electrons with high kinetic energy, corresponding to core electrons, and enhance the contribution of the valence electrons in the recovered electron density pictures. The method was already used in former projects to image the flow of valence electrons during a pericyclic reaction of semibullvalene in the gas phase.[218] Alternative approaches to tackle the image-processing problem by using wavelet decomposition have been proposed.[219] Following a novel combination of the two approaches, we have investigated time-resolved

imaging of a copper dimer diffusion dynamics on MgO(001) using the computational setup described in the first two papers of this thesis. The question is the applicability of this method to surface processes including atoms with larger differences in their atomic numbers and electron densities. Preliminary results have demonstrated the capabilities of this new method, which will be published soon. It opens a new avenue to probe and observe heterogeneous catalytic reactions directly as they unfold. Owing to its conceptual simplicity, it will possibly become an important technique in surface science to map bond formation and breaking on their natural timescale!

Bibliography

[1] I. Chorkendorff and J. Niemantsverdriet, *Concepts of Modern Catalysis and Kinetics*, 3rd (Wiley, 2017) (cit. on p. 1).

[2] R. Ye, T. J. Hurlburt, K. Sabyrov, S. Alayoglu, and G. A. Somorjai, "Molecular catalysis science: Perspective on unifying the fields of catalysis", Proc. Natl. Acad. Sci. USA **113**, 5159–5166 (2016) (cit. on p. 1).

[3] A. Wang, J. Li, and T. Zhang, "Heterogeneous single-atom catalysis", Nat. Rev. Chem. **2**, 65–81 (2018) (cit. on p. 1).

[4] M. Flytzani-Stephanopoulos and B. C. Gates, "Atomically Dispersed Supported Metal Catalysts", Annu Rev Chem Biomol Eng **3**, 545–574 (2012) (cit. on p. 1).

[5] X. F. Yang, A. Wang, B. Qiao, J. Li, J. Liu, and T. Zhang, "Single-Atom Catalysts: A New Frontier in Heterogeneous Catalysis", Acc. Chem. Res. **46**, 1740–1748 (2013) (cit. on pp. 1, 83).

[6] F. Li, Y. Li, X. C. Zeng, and Z. Chen, "Exploration of High-Performance Single-Atom Catalysts on Support M1/FeOx for CO Oxidation via Computational Study", ACS Catal. **5**, 544–552 (2015) (cit. on pp. 1, 83).

[7] S. Liang, C. Hao, and Y. Shi, "The Power of Single-Atom Catalysis", ChemCatChem **7**, 2559–2567 (2015) (cit. on p. 1).

[8] J. Jones, H. Xiong, A. T. DeLaRiva, E. J. Peterson, H. Pham, S. R. Challa, G. Qi, S. Oh, M. H. Wiebenga, X. I. Pereira-Hernández, Y. Wang, and A. K. Datye, "Thermally stable single-atom platinum-on-ceria catalysts via atom trapping", Science **353**, 150–154 (2016) (cit. on p. 1).

[9] J. Liu, "Catalysis by Supported Single Metal Atoms", ACS Catal. **7**, 34–59 (2017) (cit. on pp. 1, 83).

[10] H. Zhang, G. Liu, L. Shi, and J. Ye, "Single-Atom Catalysts: Emerging Multifunctional Materials in Heterogeneous Catalysis", Adv. Energy Mater. **8**, 1701343 (2018) (cit. on p. 1).

[11] Y. Chen, S. Ji, C. Chen, Q. Peng, D. Wang, and Y. Li, "Single-Atom Catalysts: Synthetic Strategies and Electrochemical Applications", Joule **2**, 1242–1264 (2018) (cit. on pp. 1, 83).

[12] G. S. Parkinson, "Single-Atom Catalysis: How Structure Influences Catalytic Performance", Catal. Lett. **149**, 1137–1146 (2019) (cit. on pp. 1, 83).

[13] N. Cheng, L. Zhang, K. Doyle-Davis, and X. Sun, "Single-Atom Catalysts: From Design to Application", Electrochem. Energy Rev. **2**, 539–573 (2019) (cit. on pp. 1, 83).

[14] B. Qiao, A. Wang, X. Yang, L. F. Allard, Z. Jiang, Y. Cui, J. Liu, J. Li, and T. Zhang, "Single-atom catalysis of CO oxidation using Pt1/FeOx", Nat. Chem. **3**, 634–641 (2011) (cit. on p. 1).

[15] S. Abbet, U. Heiz, H. Häkkinen, and U. Landman, "CO Oxidation on a Single Pd Atom Supported on Magnesia", Phys. Rev. Lett. **86**, 5950–5953 (2001) (cit. on p. 1).

[16] M. F. Camellone and S. Fabris, "Reaction Mechanisms for the CO Oxidation on Au/CeO2 Catalysts: Activity of Substitutional Au3+/Au+ Cations and Deactivation of Supported Au+ Adatoms", J. Am. Chem. Soc. **131**, 10473–10483 (2009) (cit. on pp. 1, 86).

[17] C. Papadopoulos, K. Kappis, J. Papavasiliou, J. Vakros, M. Kuśmierz, W. Gac, Y. Georgiou, Y. Deligiannakis, and G. Avgouropoulos, "Copper-promoted ceria catalysts for CO oxidation reaction", Catal. Today (2019) (cit. on p. 1).

[18] M. Moses-DeBusk, M. Yoon, L. F. Allard, D. R. Mullins, Z. Wu, X. Yang, G. Veith, G. M. Stocks, and C. K. Narula, "CO Oxidation on Supported Single Pt Atoms: Experimental and ab Initio Density Functional Studies of CO Interaction with Pt Atom on θ-Al2O3(010) Surface", J. Amer. Chem. Soc. **135**, 12634–12645 (2013) (cit. on p. 1).

[19] T. K. Ghosh and N. N. Nair, "Rh1/γ-Al2O3 Single-Atom Catalysis of O2 Activation and CO Oxidation: Mechanism, Effects of Hydration, Oxidation State, and Cluster Size", ChemCatChem **5**, 1811–1821 (2013) (cit. on p. 1).

[20] Y. Li, Z. Zhou, G. Yu, W. Chen, and Z. Chen, "CO Catalytic Oxidation on Iron-Embedded Graphene: Computational Quest for Low-Cost Nanocatalysts", The Journal of Physical Chemistry C J. Phys. Chem. C **114**, 6250–6254 (2010) (cit. on p. 1).

[21] P. Wu, P. Du, H. Zhang, and C. Cai, "Graphyne-supported single Fe atom catalysts for CO oxidation", Phys. Chem. Chem. Phys. **17**, 1441–1449 (2015) (cit. on p. 1).

[22] L. Zhang, I. A. W. Filot, Y.-Q. Su, J.-X. Liu, and E. J. M. Hensen, "Understanding the Impact of Defects on Catalytic CO Oxidation of LaFeO3-Supported Rh, Pd, and Pt Single-Atom Catalysts", J. Phys. Chem. C **123**, 7290–7298 (2019) (cit. on p. 1).

[23] Y. Zhu, K. Zhao, J. Shi, X. Ren, X. Zhao, Y. Shang, X. Xue, H. Guo, X. Duan, H. He, Z. Guo, and S. Li, "Strain Engineering of a Defect-Free, Single-Layer MoS2 Substrate for Highly Efficient Single-Atom Catalysis of CO Oxidation", ACS Appl. Mater. Interfaces **11**, 32887–32894 (2019) (cit. on p. 1).

[24] X. Zhang, H. Shi, and B.-Q. Xu, "Catalysis by Gold: Isolated Surface Au3+ Ions are Active Sites for Selective Hydrogenation of 1,3-Butadiene over Au/ZrO2 Catalysts", Angew. Chem. Int. Ed. **44**, 7132–7135 (2005) (cit. on p. 1).

[25] S. F. J. Hackett, R. M. Brydson, M. H. Gass, I. Harvey, A. D. Newman, K. Wilson, and A. F. Lee, "High-Activity, Single-Site Mesoporous Pd/Al2O3 Catalysts for Selective Aerobic Oxidation of Allylic Alcohols", Angew. Chem. Int. Ed. **46**, 8593–8596 (2007) (cit. on p. 1).

[26] J. Liu, "Advanced Electron Microscopy of Metal-Support Interactions in Supported Metal Catalysts", English (US), ChemCatChem **3**, 934–948 (2011) (cit. on p. 1).

[27] H. S. Taylor and E. F. Armstrong, "A theory of the catalytic surface", Proc. Royal Soc. Lond. **108**, 105–111 (1925) (cit. on p. 1).

[28] J. J. Rooney and G. Webb, "The importance of π-bonded intermediates in hydrocarbon reactions on transition metal catalysts", J. Catal. **3**, 488–501 (1964) (cit. on p. 2).

[29] W. R. Patterson and J. J. Rooney, "Single atom sites and hydrocarbon reaction mechanisms", Catal. Today **12**, 113–129 (1992) (cit. on p. 2).

[30] K. Asakura, H. Nagahiro, N. Ichikuni, and Y. Iwasawa, "Structure and catalytic combustion activity of atomically dispersed Pt species at MgO surface", Applied Catalysis A: General **188**, 313–324 (1999) (cit. on p. 2).

[31] A. Sanchez, S. Abbet, U. Heiz, W.-D. Schneider, H. Häkkinen, R. N. Barnett, and U. Landman, "When Gold Is Not Noble: Nanoscale Gold Catalysts", The Journal of Physical Chemistry A **103**, 9573–9578 (1999) (cit. on p. 2).

[32] H. Häkkinen, S. Abbet, A. Sanchez, U. Heiz, and U. Landman, "Structural, Electronic, and Impurity-Doping Effects in Nanoscale Chemistry: Supported Gold Nanoclusters", Angew. Chem. Int. Ed. **42**, 1297–1300 (2003) (cit. on p. 2).

[33] M. Arenz, U. Landman, and U. Heiz, "CO Combustion on Supported Gold Clusters", ChemPhysChem **7**, 1871–1879 (2006) (cit. on pp. 2, 83).

[34] T. Bernhardt, U. Heiz, and U. Landman, "Nanocatalysis", in *Nanocatalysis*, edited by U. Heiz and U. Landman (Springer Berlin Heidelberg, Berlin, Heidelberg, 2007) Chap. Chemical and Catalytic Properties of Size-Selected Free and Supported Clusters, pp. 1–191 (cit. on p. 2).

[35] G. E. Johnson, C. Wang, T. Priest, and J. Laskin, "Monodisperse Au11 Clusters Prepared by Soft Landing of Mass Selected Ions", Anal. Chem. **83**, 8069–8072 (2011) (cit. on p. 2).

[36] D. Cha and G. Parravano, "Surface reactivity of supported gold: I. Oxygen transfer between CO and CO_2", J. Catal. **18**, 200–211 (1970) (cit. on p. 2).

[37] G. C. Bond, P. A. Sermon, G. Webb, D. A. Buchanan, and P. B. Wells, "Hydrogenation over supported gold catalysts", J. Chem. Soc., Chem. Commun., 444b–445 (1973) (cit. on p. 2).

[38] H. Huber, D. McIntosh, and G. A. Ozin, "A metal atom model for the oxidation of carbon monoxide to carbon dioxide. The gold atom-carbon monoxide-dioxygen reaction and the gold atom-carbon dioxide reaction", Inorg. Chem. **16**, 975–979 (1977) (cit. on p. 2).

[39] M. Haruta, T. Kobayashi, H. Sano, and N. Yamada, "Novel Gold Catalysts for the Oxidation of Carbon Monoxide at a Temperature far below 0 Celsius", Chem. Lett. **16**, 405–408 (1987) (cit. on p. 2).

[40] M. Haruta, N. Yamada, T. Kobayashi, and S. Iijima, "Gold Catalysts Prepared by Coprecipitation for Low-Temperature Oxidation of Hydrogen and of Carbon Monoxide", J. Catal. **115**, 301–309 (1989) (cit. on p. 2).

[41] M. Haruta, "Size- and Support-Dependency in the Catalysis of Gold", Catal. Today **36**, 153–166 (1997) (cit. on p. 2).

[42] P. Pyykkö, "Theoretical Chemistry of Gold", Angew. Chem. Int. Ed. **43**, 4412–4456 (2004) (cit. on p. 2).

[43] P Pyykkö, "Theoretical chemistry of gold. II", Inorg. Chim. Acta **358**, 4113–4130 (2005) (cit. on p. 2).

[44] P. Pyykkö, "Theoretical chemistry of gold. III", Chem. Soc. Rev. **37**, 1967–1997 (2008) (cit. on p. 2).

[45] A. S. K. Hashmi and G. J. Hutchings, "Gold Catalysis - the Journey Continues", Catal. Sci. Technol. **3**, 2861 (2013) (cit. on p. 2).

[46] W. Song and E. J. M. Hensen, "A computational DFT study of CO oxidation on a Au nanorod supported on CeO2(110): on the role of the support termination", Catal. Sci. Technol. **3**, 3020–3029 (2013) (cit. on p. 2).

[47] Y. Y. Wu, N. A. Mashayekhi, and H. H. Kung, "Au-metal oxide support interface as catalytic active sites", Catal. Sci. Technol. **3**, 2881–2891 (2013) (cit. on p. 2).

[48] H. Häkkinen and U. Landman, "Gas-Phase Catalytic Oxidation of CO by Au2-", J. Am. Chem. Soc. **123**, 9704–9705 (2001) (cit. on p. 2).

[49] L. D. Socaciu, J. Hagen, T. M. Bernhardt, L. Wöste, U. Heiz, H. Häkkinen, and U. Landman, "Catalytic CO Oxidation by Free Au2-: Experiment and Theory", J. Am. Chem. Soc. **125**, 10437–10445 (2003) (cit. on p. 2).

[50] J. Hagen, L. D. Socaciu, M. Elijazyfer, U. Heiz, T. M. Bernhardt, and L. Woste, "Coadsorption of CO and O2 on Small Free Gold Cluster Anions at Cryogenic Temperatures: Model Complexes for Catalytic CO Oxidation", Phys. Chem. Chem. Phys. **4**, 1707–1709 (2002) (cit. on p. 2).

[51] T. M. Bernhardt, L. D. Socaciu-Siebert, J. Hagen, and L. Wöste, "Size and Composition Dependence in {CO} Oxidation Reaction on Small Free Gold, Silver, and Binary Silver-Gold Cluster Anions", Appl. Catal. A **291**, 170–178 (2005) (cit. on p. 2).

[52] G. Mills, M. S. Gordon, and H. Metiu, "The Adsorption of Molecular Oxygen on Neutral and Negative Aun Clusters (n=2-5)", Chem. Phys. Lett. **359**, 493–499 (2002) (cit. on p. 2).

[53] B. Yoon, H. Häkkinen, and U. Landman, "Interaction of O2 with Gold Clusters: Molecular and Dissociative Adsorption", J. Phys. Chem. A **107**, 4066–4071 (2003) (cit. on p. 2).

[54] L. M. Molina and B. Hammer, "Oxygen Adsorption at Anionic Free and Supported Au Clusters", J. Chem. Phys. **123**, 161104 (2005) (cit. on p. 2).

[55] G. Pacchioni, L. Giordano, and M. Baistrocchi, "Charging of Metal Atoms on Ultrathin MgO/Mo(100) Films", Phys. Rev. Lett. **94**, 226104 (2005) (cit. on pp. 2, 4).

[56] B. Yoon, H. Häkkinen, U. Landman, A. S. Wörz, J.-M. Antonietti, S. Abbet, K. Judai, and U. Heiz, "Charging Effects on Bonding and Catalyzed Oxidation of CO on Au8 Clusters on MgO", Science **307**, 403–407 (2005) (cit. on pp. 2, 3).

[57] A. Del Vitto, G. Pacchioni, F. Delbecq, and P. Sautet, "Au Atoms and Dimers on the MgO(100) Surface: A DFT Study of Nucleation at Defects", J. Phys. Chem. B **109**, 8040–8048 (2005) (cit. on pp. 2–4, 87).

[58] P. Frondelius, H. Häkkinen, and K. Honkala, "Adsorption of small Au clusters on MgO and MgO/Mo: the role of oxygen vacancies and the Mo-support", New J. Phys. **9**, 339 (2007) (cit. on pp. 2, 3).

[59] P. Frondelius, H. Häkkinen, and K. Honkala, "Adsorption of gold clusters on metal-supported MgO: Correlation to electron affinity of gold", Phys. Rev. B **76**, 073406 (2007) (cit. on pp. 2, 3).

[60] S. Schintke, S. Messerli, M. Pivetta, F. Patthey, L. Libioulle, M. Stengel, A. De Vita, and W.-D. Schneider, "Insulator at the Ultrathin Limit: MgO on Ag(001)", Phys. Rev. Lett. **87**, 276801 (2001) (cit. on p. 2).

[61] U. Landman, B. Yoon, C. Zhang, U. Heiz, and M. Arenz, "Factors in gold nanocatalysis: oxidation of CO in the non-scalable size regime", English, Top. Catal. **44**, 145–158 (2007) (cit. on p. 2).

[62] N. Nikbin, G. Mpourmpakis, and D. G. Vlachos, "A Combined DFT and Statistical Mechanics Study for the CO Oxidation on the Au_10^{-1} Cluster", J. Phys. Chem. C **115**, 20192–20200 (2011) (cit. on p. 2).

[63] C. Liu, Y. Tan, S. Lin, H. Li, X. Wu, L. Li, Y. Pei, and X. C. Zeng, "CO Self-Promoting Oxidation on Nanosized Gold Clusters: Triangular Au_3 Active Site and CO Induced O-O Scission", J. Am. Chem. Soc. **135**, 2583–2595 (2013) (cit. on p. 2).

[64] N. Nikbin, N. Austin, D. G. Vlachos, M. Stamatakis, and G. Mpourmpakis, "Catalysis at the sub-nanoscale: complex CO oxidation chemistry on a few Au atoms", Catal. Sci. Technol. **5**, 134–141 (2015) (cit. on pp. 2, 86, 91).

[65] M. A. Brown, F. Ringleb, Y. Fujimori, M. Sterrer, H.-J. Freund, G. Preda, and G. Pacchioni, "Initial Formation of Positively Charged Gold on MgO(001) Thin Films: Identification by Experiment and Structural Assignment by Theory", J. Phys. Chem. C **115**, 10114–10124 (2011) (cit. on pp. 3, 84).

[66] M. Amft and N. V. Skorodumova, "Catalytic Activity of Small MgO-supported Au Clusters Towards CO Oxidation: A Density Functional Study", Phys. Rev. B **81**, 195443 (2010) (cit. on p. 3).

[67] L. D. Socaciu, J. Hagen, J. Le Roux, D. Popolan, T. M. Bernhardt, L. Wöste, and v. Vajda, "Strongly Cluster Size Dependent Reaction Behavior of CO with O2 on Free Silver Cluster Anions", J. Chem. Phys. **120**, 2078–2081 (2004) (cit. on p. 3).

[68] Q. Xu and L. Jiang, "Oxidation of Carbon Monoxide on Group 11 Metal Atoms: Matrix-Isolation Infrared Spectroscopy and Density Functional Theory Study", J. Phys. Chem. A **110**, 2655–2662 (2006) (cit. on p. 4).

[69] H. Grönbeck and P. Broqvist, "CO-Induced Modification of the Metal/MgO(100) Interaction", J. Phys. Chem. B **107**, 12239–12243 (2003) (cit. on p. 4).

[70] M. Sterrer, M. Yulikov, T. Risse, H.-J. Freund, J. Carrasco, F. Illas, C. Di Valentin, L. Giordano, and G. Pacchioni, "When the Reporter Induces the Effect: Unusual IR Spectra of CO on Au1/MgO(001)/Mo(001)", Angew. Chem. Int. Ed. **45**, 2633–2635 (2006) (cit. on p. 4).

[71] B. Liang and L. Andrews, "Reactions of Laser-Ablated Ag and Au Atoms with Carbon Monoxide: Matrix Infrared Spectra and Density Functional Calculations on $Ag(CO)_n$ (n=2,3), $Au(CO)_n$ (n=1,2) and $M(CO)_n^+$ (n=1-4; M=Ag,Au)", J. Phys. Chem. A **104**, 9156–9164 (2000) (cit. on p. 4).

[72] L. Jiang and Q. Xu, "Reactions of Gold Atoms and Small Clusters with CO: Infrared Spectroscopic and Theoretical Characterization of Au_nCO (n=1-5) and $Au_n(CO)_2$ (n=1,2) in Solid Argon", J. Phys. Chem. A **109**, 1026–1032 (2005) (cit. on p. 4).

[73] N. Sheppard and N. N. Nguyen, "Advances in Infrared and Raman Spectroscopy, Vol. 5", in, Vol. 5, edited by R. E. Hester and R. J. H. Clark, Advances in Infrared and Raman Spectroscopy (Heyden London, 1978) Chap. 2, p. 67 (cit. on p. 4).

[74] G. A. Somorjai and J. Carrazza, "Structure sensitivity of catalytic reactions", Ind. Eng. Chem. Res. **25**, 63–69 (1986) (cit. on p. 4).

[75] Z.-J. Zhao, Z. Li, Y. Cui, H. Zhu, W. F. Schneider, W. N. Delgass, F. Ribeiro, and J. Greeley, "Importance of metal-oxide interfaces in heterogeneous catalysis: A combined DFT, microkinetic, and experimental study of water-gas shift on Au/MgO", J. Catal. **345**, 157–169 (2017) (cit. on p. 4).

[76] A. M. Burow, M. Sierka, J. Döbler, and J. Sauer, "Point defects in CaF2 and CeO2 investigated by the periodic electrostatic embedded cluster method", J. Chem. Phys. **130**, 174710, 174710 (2009) (cit. on pp. 5, 18, 20).

[77] C. Duriez, C. Chapon, C. R. Henry, and J. M. Rickard, "Structural characterization of MgO(100) surfaces", Surf. Sci. **230**, 123–136 (1990) (cit. on p. 5).

[78] C. R. Henry, C. Chapon, and C. Duriez, "Precursor state in the chemisorption of CO on supported palladium clusters", J. Chem. Phys. **95**, 700–705 (1991) (cit. on p. 5).

[79] C. R. Henry, C. Chapon, and C. Duriez, "Physics and Chemistry of Small Clusters", in , Vol. 158, edited by P. Jena, B. K. Rao, and S. N. Khanna, 1st, NATO ASI Series (Plenum Press, New York and London) (Springer US, 1987) Chap. Molecular Beam Relaxation Spectroscopy Applied to Adsorption Kinetics on Small Supported Catalyst Particles, pp. 795–800 (cit. on p. 5).

[80] S. Furuyama, H. Fujii, M. Kawamura, and T. Morimoto, "Physisorption of nitric oxide, carbon monoxide, nitrogen, and oxygen by magnesium oxide powder", J. Phys. Chem. **82**, 1028–1032 (1978) (cit. on p. 5).

[81] H. Jian-Wei, C. A. Estrada, J. S. Corneille, W. Ming-Cheng, and D. W. Goodman, "CO adsorption on ultrathin MgO films grown on a Mo(100) surface: an IRAS study", Surf. Sci. **261**, 164–170 (1992) (cit. on p. 5).

[82] R. Wichtendahl, M. Rodriguez-Rodrigo, U. Härtel, H. Kuhlenbeck, and H.-J. Freund, "Thermodesorption of CO and NO from Vacuum-Cleaved NiO(100) and MgO(100)", Phys. Status Solidi A **173**, 93–100 (1999) (cit. on pp. 5, 93).

[83] C. Quintanar, R. Caballero, and V. M. Castaño, "Adsorption of CO on the rumpled MgO(100), MgO(100):Ni, and MgO(100):Cr surfaces: A density functional approach", Int. J. Quantum Chem. **102**, 820–828 (2005) (cit. on p. 5).

[84] F. Illas, G. Pacchioni, A. Pelmenschikov, L. G. M. Pettersson, R. Dovesi, C. Pisani, K. M. Neyman, and N. Rösch, "Comment on "First-principles determination of the bonding mechanism and adsorption energy for CO/MgO(001)" [Chem. Phys. Lett. 290 (1998) 255]", Chem. Phys. Lett. **306**, 202–204 (1999) (cit. on pp. 5, 93).

[85] R. Wu and Q. Zhang, "Reply to Comment on "First principles determination of the bonding mechanism and adsorption energy for CO/MgO(001)" Re. to PII nr.: S0009-2614(99)00410-8.1", Chem. Phys. Lett. **306**, 205–208 (1999) (cit. on pp. 5, 93).

[86] G. Comsa, "Surface scattering of thermal energy He beams: from the proof of the wave nature of atoms to a versatile and efficient surface probe", Surf. Sci. **299-300**, 77–91 (1994) (cit. on p. 5).

[87] J. Libuda and H.-J. Freund, "Molecular beam experiments on model catalysts", Surf. Sci. Rep. **57**, 157–298 (2005) (cit. on p. 5).

[88] R. B. Gerber, "Molecular scattering from surfaces: theoretical methods and results", Chem. Rev. **87**, 29–79 (1987) (cit. on p. 5).

[89] A. W. Kleyn, "Molecular beams and chemical dynamics at surfaces", Chem. Soc. Rev. **32**, 87–95 (2003) (cit. on p. 5).

[90] G.-J. Kroes and C. Díaz, "Quantum and classical dynamics of reactive scattering of H_2 from metal surfaces", Chem. Soc. Rev. **45**, 3658–3700 (2016) (cit. on p. 5).

[91] A. M. Wodtke, "Electronically non-adiabatic influences in surface chemistry and dynamics", Chem. Soc. Rev. **45**, 3641–3657 (2016) (cit. on p. 5).

[92] K. Golibrzuch, N. Bartels, D. J. Auerbach, and A. M. Wodtke, "The Dynamics of Molecular Interactions and Chemical Reactions at Metal Surfaces: Testing the Foundations of Theory", Annu. Rev. Phys. Chem. **66**, 399–425 (2015) (cit. on p. 6).

[93] G. Füchsel, M del Cueto, C. Díaz, and G.-J. Kroes, "Enigmatic HCl + Au(111) Reaction: A Puzzle for Theory and Experiment", J. Phys. Chem. C **120**, 25760–25779 (2016) (cit. on pp. 6, 29, 33, 63).

[94] W. Koch and M. C. Holthausen, *A chemists guide to density functional theory*, 2nd (Wiley-VCH, Weinheim, New York, Chichester, 2001) (cit. on pp. 8, 13, 17).

[95] D. J. Tannor, *Introduction to Quantum Mechanics* (University Science Books, 2007) (cit. on pp. 8, 9).

[96] E. Schrödinger, "An Undulatory Theory of the Mechanics of Atoms and Molecules", Phys. Rev. **28**, 1049–1070 (1926) (cit. on p. 8).

[97] A. Szabo and N. S. Ostlund, *Modern Quantum Chemistry: Introduction to Advanced Electronic Structure Theory*, 1st (Dover Publications, Inc., Mineola, 1996) (cit. on pp. 9, 14).

[98] M. Born and R. Oppenheimer, "Zur Quantentheorie der Molekeln", Ann. Phys. **389**, 457–484 (1927) (cit. on p. 10).

[99] N. W. Ashcroft and N. D. Mermin, *Solid State Physics*, HRW international editions (Saunders College, 1976) (cit. on p. 11).

[100] C. Kittel, *Introduction to Solid State Physics*, 7th (Wiley, 1996) (cit. on p. 11).

[101] F. Jensen, *Introduction to Computational Chemistry*, 2nd (Wiley, USA, 2007) (cit. on pp. 11, 13).

[102] G. Czycholl, *Theoretische Festkörperphysik Band 1: Grundlagen: Phononen und Elektronen in Kristallen*, 4th (Springer, 2015) (cit. on p. 11).

[103] F. Bloch, "Über die Quantenmechanik der Elektronen in Kristallgittern", Z. Phys. **52**, 555–600 (1929) (cit. on p. 11).

[104] F. Neese, "Prediction of molecular properties and molecular spectroscopy with density functional theory: From fundamental theory to exchange-coupling", Coord. Chem. Rev. **253**, 526 –563 (2009) (cit. on p. 13).

[105] N. Mardirossian and M. Head-Gordon, "Thirty years of density functional theory in computational chemistry: an overview and extensive assessment of 200 density functionals", Mol. Phys. **115**, 2315–2372 (2017) (cit. on p. 13).

[106] P. Hohenberg and W. Kohn, "Inhomogeneous Electron Gas", Phys. Rev. **136**, B864–B871 (1964) (cit. on p. 14).

[107] W. Kohn and L. J. Sham, "Self-Consistent Equations Including Exchange and Correlation Effects", Phys. Rev. **140**, A1133–A1138 (1965) (cit. on p. 14).

[108] J. C. Slater, "The Theory of Complex Spectra", Phys. Rev. **34**, 1293–1322 (1929) (cit. on p. 15).

[109] R. G. Parr and Y. Weitao, *Density-Functional Theory of Atoms and Molecules*, International Series of Monographs on Chemistry (Oxford University Press, 1989) (cit. on p. 16).

[110] J. P. Perdew and K. Schmidt, "Jacob's ladder of density functional approximations for the exchange-correlation energy", AIP Conf. Proc. **577**, 1–20 (2001) (cit. on p. 16).

[111] P. A. M. Dirac, "Note on Exchange Phenomena in the Thomas Atom", Math. Proc. Camb. Philos. Soc. **26**, 376–385 (1930) (cit. on p. 17).

[112] S. H. Vosko, L. Wilk, and M. Nusair, "Accurate spin-dependent electron liquid correlation energies for local spin density calculations: a critical analysis", Can. J. Phys. **58**, 1200–1211 (1980) (cit. on p. 17).

[113] D. M. Ceperley and B. J. Alder, "Ground State of the Electron Gas by a Stochastic Method", Phys. Rev. Lett. **45**, 566–569 (1980) (cit. on p. 17).

[114] J. P. Perdew and Y. Wang, "Accurate and simple analytic representation of the electron-gas correlation energy", Phys. Rev. B **45**, 13244–13249 (1992) (cit. on p. 17).

[115] A. D. Becke, "Density-functional exchange-energy approximation with correct asymptotic behavior", Phys. Rev. A **38**, 3098–3100 (1988) (cit. on pp. 17, 18).

[116] J. P. Perdew, J. A. Chevary, S. H. Vosko, K. A. Jackson, M. R. Pederson, D. J. Singh, and C. Fiolhais, "Atoms, molecules, solids, and surfaces: Applications of the generalized gradient approximation for exchange and correlation", Phys. Rev. B **46**, 6671–6687 (1992) (cit. on p. 17).

[117] J. Perdew, K. Burke, and M. Ernzerhof, "Generalized Gradient Approximation Made Simple", Phys. Rev. Lett. **77**, 3865–3868 (1996) (cit. on p. 17).

[118] Y. Zhang and W. Yang, "Comment on "Generalized Gradient Approximation Made Simple"", Phys. Rev. Lett. **80**, 890–890 (1998) (cit. on p. 17).

[119] B. Hammer, L. B. Hansen, and J. Nørskov, "Improved adsorption energetics within density-functional theory using revised Perdew-Burke-Ernzerhof functionals", Phys. Rev. B **59**, 7413–7421 (1999) (cit. on p. 17).

[120] J. P. Perdew, A. Ruzsinszky, G. I. Csonka, O. A. Vydrov, G. E. Scuseria, L. A. Constantin, X. Zhou, and K. Burke, "Restoring the Density-Gradient Expansion for Exchange in Solids and Surfaces", Phys. Rev. Lett. **100**, 136406 (2008) (cit. on p. 17).

[121] A. D. Becke, "Density functional thermochemistry. III. The role of exact exchange", J. Chem. Phys. **98**, 5648–5652 (1993) (cit. on p. 17).

[122] C. Adamo and V. Barone, "Toward reliable density functional methods without adjustable parameters: The PBE0 model", J. Chem. Phys. **110**, 6158–6170 (1999) (cit. on p. 17).

[123] C. Lee, W. Yang, and R. G. Parr, "Development of the Colle-Salvetti correlation-energy formula into a functional of the electron density", Phys. Rev. B **37**, 785–789 (1988) (cit. on p. 18).

[124] P. J. Stephens, F. J. Devlin, C. F. Chabalowski, and M. J. Frisch, "Ab Initio Calculation of Vibrational Absorption and Circular Dichroism Spectra Using Density Functional Force Fields", J. Chem. Phys. **98**, 11623–11627 (1994) (cit. on p. 18).

[125] L. A. Curtiss, K. Raghavachari, G. W. Trucks, and J. A. Pople, "Gaussian-2 theory for molecular energies of first- and second-row compounds", J. Chem. Phys. **94**, 7221–7230 (1991) (cit. on p. 18).

[126] V. Staemmler, "Theoretical Aspects of Transition Metal Catalysis", in , Vol. 12, edited by G. Frenking, Topics in Organometallic Chemistry (Springer Berlin Heidelberg, Berlin, Heidelberg, 2005) Chap. The Cluster Approach for the Adsorption of Small Molecules on Oxide Surfaces, pp. 219–256 (cit. on p. 18).

[127] K. N. Kudin and G. E. Scuseria, "A fast multipole method for periodic systems with arbitrary unit cell geometries", Chem. Phys. Lett. **283**, 61–68 (1998) (cit. on p. 19).

[128] K. N. Kudin and G. E. Scuseria, "Revisiting infinite lattice sums with the periodic fast multipole method", J. Chem. Phys. **121**, 2886–2890 (2004) (cit. on p. 19).

[129] L. Greengard and V. Rokhlin, "A fast algorithm for particle simulations", J. Comp. Phys. **73**, 325–348 (1987) (cit. on p. 19).

[130] L. Greengard, *The Rapid evaluation of potential fields in particle systems*, ACM distinguished dissertations (Cambridge, Mass. MIT Press, 1988) (cit. on p. 19).

[131] M. Sierka, A. Hogekamp, and R. Ahlrichs, "Fast evaluation of the Coulomb potential for electron densities using multipole accelerated resolution of identity approximation", J. Chem. Phys. **118**, 9136–9148 (2003) (cit. on p. 19).

[132] V. Rokhlin, "Rapid solution of integral equations of classical potential theory", J. Comput. Phys. **60**, 187 –207 (1985) (cit. on p. 19).

[133] C. A. White and M. Head-Gordon, "Derivation and efficient implementation of the fast multipole method", J. Chem. Phys. **101**, 6593–6605 (1994) (cit. on p. 19).

[134] P. P. Ewald, "Die Berechnung optischer und elektrostatischer Gitterpotentiale", Ann. Phys. **369**, 253–287 (1921) (cit. on p. 20).

[135] H. Jónsson, G. Mills, and K. W. Jacobsen, "Classical and Quantum Dynamics in Condensed Phase Simulations", in , edited by B. Berne, G. Ciccotti, and D. Coker (World Scientific, 1998) Chap. Nudged elastic band method for finding minimum energy paths of transition, pp. 385–404 (cit. on pp. 20–22).

[136] G. Henkelman, B. P. Uberuaga, and H. Jónsson, "A climbing image nudged elastic band method for finding saddle points and minimum energy paths", J. Chem. Phys. **113**, 9901–9904 (2000) (cit. on pp. 20–22).

[137] G. Henkelman and H. Jónsson, "Improved tangent estimate in the nudged elastic band method for finding minimum energy paths and saddle points", J. Chem. Phys. **113**, 9978–9985 (2000) (cit. on p. 20).

[138] *http://theory.cm.utexas.edu/henkelman/research/saddle/ [Online; accessed October 17, 2019]* (Henkelman, G.) (cit. on p. 20).

[139] S. Smidstrup, A. Pedersen, K. Stokbro, and H. Jónsson, "Improved initial guess for minimum energy path calculations", J. Chem. Phys. **140**, 214106 (2014) (cit. on p. 20).

[140] E. Bitzek, P. Koskinen, F. Gähler, M. Moseler, and P. Gumbsch, "Structural Relaxation Made Simple", Phys. Rev. Lett. **97**, 170201 (2006) (cit. on p. 22).

[141] A. H. Larsen, J. J. Mortensen, J. Blomqvist, I. E. Castelli, R. Christensen, M. Dułak, J. Friis, M. N. Groves, B. Hammer, C. Hargus, E. D. Hermes, P. C. Jennings, P. B. Jensen, J. Kermode, J. R. Kitchin, E. L. Kolsbjerg, J. Kubal, K. Kaasbjerg, S. Lysgaard, J. B. Maronsson, T. Maxson, T. Olsen, L. Pastewka, A. Peterson, C. Rostgaard, J. Schiøtz, O. Schütt, M. Strange, K. S. Thygesen, T. Vegge, L. Vilhelmsen, M. Walter, Z. Zeng, and K. W. Jacobsen, "The atomic simulation environment – a Python library for working with atoms", J. Phys. Condens. Matter **29**, 273002 (2017) (cit. on p. 22).

[142] P. Su and H. Li, "Energy decomposition analysis of covalent bonds and intermolecular interactions", J. Chem. Phys. **131**, 014102 (2009) (cit. on p. 23).

[143] L. Zhao, M. von Hopffgarten, D. Andrada, and G. Frenking, "Energy decomposition analysis", Wiley Interdiscip. Rev. Comput. Mol. Sci. **8**, e1345 (2018) (cit. on p. 23).

[144] W. Heitler and F. London, "Wechselwirkung neutraler Atome und homöopolare Bindung nach der Quantenmechanik", Z. Phys. **44**, 455–472 (1927) (cit. on p. 23).

[145] K. Morokuma, "Molecular Orbital Studies of Hydrogen Bonds. III. C=O...H-O Hydrogen Bond in H2CO...H2O and H2CO...2H2O", J. Chem. Phys. **55**, 1236–1244 (1971) (cit. on p. 23).

[146] K. Kitaura and K. Morokuma, "A new energy decomposition scheme for molecular interactions within the Hartree-Fock approximation", Int. J. Quantum Chem. **10**, 325–340 (1976) (cit. on p. 23).

[147] T. Ziegler and A. Rauk, "On the calculation of bonding energies by the Hartree Fock Slater method", Theoret. Chim. Acta **46**, 1–10 (1977) (cit. on p. 23).

[148]   *TURBOMOLE V7.0 2015, a development of University of Karlsruhe and Forschungszentrum Karlsruhe GmbH, 1989-2007, TURBOMOLE GmbH, since 2007; available from* `http://www.turbomole.com`. (Cit. on p. 23).

[149]   D. G. Truhlar and J. T. Muckerman, "Atom - Molecule Collision Theory: A Guide for the Experimentalist", in *Atom - Molecule Collision Theory: A Guide for the Experimentalist*, Vol. 3, edited by R. B. Bernstein, Physics of Atoms and Molecules (Springer US, Boston, MA, 1979) Chap. Reactive Scattering Cross Sections III: Quasiclassical and Semiclassical Methods, pp. 505–566 (cit. on pp. 27, 29).

[150]   G. H. Peslherbe, H. Wang, and W. Hase, "Monte Carlo Methods in Chemical Physics", in , Vol. 105, edited by D. M. Ferguson, J. I. Siepmann, and D. G. Truhlar, Advances in Chemical Physics (Wiley, 1999) Chap. Monte Carlo Sampling for Classical Trajectory Simulations, pp. 171–202 (cit. on pp. 27, 33).

[151]   A. Groß, *Theoretical Surface Science - A Microscopic Perspective*, 2. (Springer Science, Berlin Heidelberg, 2009) (cit. on pp. 27, 29, 98).

[152]   L. Verlet, "Computer "Experiments" on Classical Fluids. I. Thermodynamical Properties of Lennard-Jones Molecules", Phys. Rev. **159**, 98–103 (1967) (cit. on p. 27).

[153]   W. C. Swope, H. C. Andersen, P. H. Berens, and K. R. Wilson, "A computer simulation method for the calculation of equilibrium constants for the formation of physical clusters of molecules: Application to small water clusters", J. Chem. Phys. **76**, 637–649 (1982) (cit. on p. 28).

[154]   G. Czakó and J. M. Bowman, "Reaction Dynamics of Methane with F, O, Cl, and Br on ab Initio Potential Energy Surfaces", J. Phys. Chem. A **118**, 2839–2864 (2014) (cit. on pp. 29, 35).

[155]   P. Ehrenfest, "Bemerkung über die angenäherte Gültigkeit der klassischen Mechanik innerhalb der Quantenmechanik", Z. Phys. **45**, 455–457 (1927) (cit. on p. 29).

[156]   Y. Xiao, W. Dong, and H. F. Busnengo, "Reactive force fields for surface chemical reactions: A case study with hydrogen dissociation on Pd surfaces", J. Chem. Phys. **132**, 014704 (2010) (cit. on pp. 29, 30, 63).

[157]   J. Tersoff, "New empirical approach for the structure and energy of covalent systems", Phys. Rev. B **37**, 6991–7000 (1988) (cit. on p. 30).

[158] D. W. Brenner, "Empirical potential for hydrocarbons for use in simulating the chemical vapor deposition of diamond films", Phys. Rev. B **42**, 9458–9471 (1990) (cit. on p. 30).

[159] A. C. T. van Duin, S. Dasgupta, F. Lorant, and W. A. Goddard, "ReaxFF: A Reactive Force Field for Hydrocarbons", J. Phys. Chem. A **105**, 9396–9409 (2001) (cit. on p. 30).

[160] G. R. Darling and S. Holloway, "The dissociation of diatomic molecules at surfaces", Rep. Prog. Phys. **58**, 1595–1672 (1995) (cit. on p. 30).

[161] A. Gross, S. Wilke, and M. Scheffler, "Six-Dimensional Quantum Dynamics of Adsorption and Desorption of H_2 at Pd(100): Steering and Steric Effects", Phys. Rev. Lett. **75**, 2718–2721 (1995) (cit. on p. 30).

[162] T. B. Blank, S. D. Brown, A. W. Calhoun, and D. J. Doren, "Neural network models of potential energy surfaces", J. Chem. Phys. **103**, 4129–4137 (1995) (cit. on p. 30).

[163] J. Behler, "First Principles Neural Network Potentials for Reactive Simulations of Large Molecular and Condensed Systems", Angew. Chem. Int. Ed. **56**, 12828–12840 (2017) (cit. on p. 30).

[164] R. N. Porter and L. M. Raff, "Dynamics of molecular collisions: Part B", in , Vol. 2, edited by W. Miller, 1., Modern Theoretical Chemistry (Springer, 1976) Chap. Classical Trajectory Methods in Molecular Collisions, pp. 1–52 (cit. on p. 33).

[165] E. Wigner, "On the Quantum Correction For Thermodynamic Equilibrium", Phys. Rev. **40**, 749–759 (1932) (cit. on p. 34).

[166] W. L. Hase, "Encyclopedia of Computational Chemistry, A-D", in *Encyclopedia of Computational Chemistry*, Vol. 1, edited by P. von Ragué Schleyer, Encyclopedia of Computational Chemistry, 5 Volume Set (Wileys, 1998) Chap. Classical Trajectory Simulations: Final Conditions, pp. 399–402 (cit. on p. 35).

[167] L. Bonnet and J. C. Rayez, "Quasiclassical trajectory method for molecular scattering processes: necessity of a weighted binning approach", Chem. Phys. Lett. **277**, 183–190 (1997) (cit. on p. 37).

[168] L. Bonnet and J. C. Rayez, "Gaussian weighting in the quasiclassical trajectory method", Chem. Phys. Lett. **397**, 106–109 (2004) (cit. on p. 37).

[169] Q. Wang, D. Zhang, Y. Chen, W.-F. Fu, and X.-J. Lv, "Single-Atom Catalysts for Photocatalytic Reactions", ACS Sustainable Chem. Eng. **7**, 6430–6443 (2019) (cit. on p. 83).

[170] G. Pacchioni and H.-J. Freund, "Electron Transfer at Oxide Surfaces. The MgO Paradigm: from Defects to Ultrathin Films", Chem. Rev. **113**, 4035–4072 (2013) (cit. on pp. 84, 86).

[171] G. Mills, M. S. Gordon, and H. Metiu, "Oxygen adsorption on Au clusters and a rough Au(111) surface: The role of surface flatness, electron confinement, excess electrons, and band gap", J. Chem. Phys. **118**, 4198–4205 (2003) (cit. on p. 84).

[172] H. C. Fang, Z. H. Li, and K. N. Fan, "CO oxidation catalyzed by a single gold atom: benchmark calculations and the performance of DFT methods", Phys. Chem. Chem. Phys. **13**, 13358–13369 (2011) (cit. on pp. 85, 89).

[173] A. N. Smith and D. T. Moore, "Charge-Dependent Trends in Structures and Vibrational Frequencies of [CO-Au-O2]q (q = -1, 0, +1) Complexes: Evidence for Cooperative Interactions", J. Phys. Chem. A **116**, 9370–9381 (2012) (cit. on p. 85).

[174] M. Stamatakis, M. A. Christiansen, D. G. Vlachos, and G. Mpourmpakis, "Multiscale Modeling Reveals Poisoning Mechanisms of MgO-Supported Au Clusters in CO Oxidation", Nano Lett. **12**, 3621–3626 (2012) (cit. on pp. 86, 91).

[175] P. Frondelius, H. Häkkinen, and K. Honkala, "Adsorption and activation of O2 at Au chains on MgO/Mo thin films", Phys. Chem. Chem. Phys. **12**, 1483–1492 (2010) (cit. on p. 86).

[176] A. Hellman, S. Klacar, and H. Grönbeck, "Low Temperature CO Oxidation over Supported Ultrathin MgO Films", J. Am. Chem. Soc. **131**, 16636–16637 (2009) (cit. on p. 86).

[177] G. Barcaro and A. Fortunelli, "Structure and diffusion of small Ag and Au clusters on the regular MgO (100) surface", New J. Phys. **9**, 22 (2007) (cit. on p. 87).

[178] M. Yulikov, M. Sterrer, T. Risse, and H.-J. Freund, "Gold Atoms and Clusters on MgO(100) Films; An EPR and IRAS Study", Surf. Sci. **603**, 1622–1628 (2009) (cit. on p. 87).

[179] CRC Handbook, *CRC Handbook of Chemistry and Physics*, edited by D. R. Lide, 85th (CRC Press, 2004) (cit. on p. 87).

[180] P. Schwerdtfeger and J. K. Nagle, "2018 Table of static dipole polarizabilities of the neutral elements in the periodic table", Mol. Phys. **117**, 1200–1225 (2019) (cit. on p. 87).

[181] B. Cordero, V. Gomez, A. E. Platero-Prats, M. Reves, J. Echeverria, E. Cremades, F. Barragan, and S. Alvarez, "Covalent Radii Revisited", Dalton Trans. **21**, 2832–2838 (2008) (cit. on p. 87).

[182] K. Huber, *Molecular Spectra and Molecular Structure - IV. Constants of Diatomic Molecules*, 1. (Springer US, 1979) (cit. on p. 88).

[183] M. Shimauchi, T. Miura, and H. Takuma, "Determination of Molecular Constants of the X 3 Σ g - State of O2", Jpn. J. Appl. Phys. **34**, L1689–L1691 (1995) (cit. on p. 90).

[184] H.-D. Meyer, U. Manthe, and L. S. Cederbaum, "The multi-configurational time-dependent Hartree approach", Chem. Phys. Lett. **165**, 73–78 (1990) (cit. on p. 92).

[185] H.-D. Meyer, F. Gatti, and G. Worth, *Multidimensional Quantum Dynamics* (Wiley, 2009) (cit. on p. 92).

[186] L. Chen, R. Wu, N. Kioussis, and Q. Zhang, "First principles determinations of the bonding mechanism and adsorption energy for CO/MgO(001)", Chem. Phys. Lett. **290**, 255–260 (1998) (cit. on p. 93).

[187] G. Spoto, E. N. Gribov, G. Ricchiardi, A. Damin, D. Scarano, S. Bordiga, C. Lamberti, and A. Zecchina, "Carbon monoxide MgO from dispersed solids to single crystals: a review and new advances", Progr. Surf. Sci. **76**, 71–146 (2004) (cit. on p. 93).

[188] J. Behler, "Representing potential energy surfaces by high-dimensional neural network potentials", J. Phys.: Condens. Matter **26**, 183001 (2014) (cit. on p. 94).

[189] B. Kolb, X. Luo, X. Zhou, B. Jiang, and H. Guo, "High-Dimensional Atomistic Neural Network Potentials for Molecule-Surface Interactions: HCl Scattering from Au(111)", J. Phys. Chem. Lett. **8**, 666–672 (2017) (cit. on p. 94).

[190] K. Shakouri, J. Behler, J. Meyer, and G.-J. Kroes, "Accurate Neural Network Description of Surface Phonons in Reactive Gas-Surface Dynamics: N2 + Ru(0001)", J. Phys. Chem. Lett. **8**, 2131–2136 (2017) (cit. on p. 94).

[191] N. Gerrits, K. Shakouri, J. Behler, and G.-J. Kroes, "Accurate Probabilities for Highly Activated Reaction of Polyatomic Molecules on Surfaces Using a High-Dimensional Neural Network Potential: CHD3 + Cu(111)", J. Phys. Chem. Lett. **10**, 1763–1768 (2019) (cit. on p. 94).

[192] G. Groß, "Reactions at surfaces studied by ab initio dynamics calculations", Surf. Sci. Rep. **32**, 291–340 (1998) (cit. on p. 94).

[193] G. J. Kroes and M. F. Somers, "Six-Dimensional Dynamics of Dissociative Chemisorption of H2 on Metal Surfaces", J. Theor. Comput. Chem. **04**, 493–581 (2005) (cit. on p. 94).

[194] C. Díaz, E. Pijper, R. A. Olsen, H. F. Busnengo, D. J. Auerbach, and G. J. Kroes, "Chemically Accurate Simulation of a Prototypical Surface Reaction: H2 Dissociation on Cu(111)", Science **326**, 832–834 (2009) (cit. on p. 94).

[195] A. S. Muzas, M. del Cueto, F. Gatti, M. F. Somers, G. J. Kroes, F. Martín, and C. Díaz, "H_2/LiF(001) diffractive scattering under fast grazing incidence using a DFT-based potential energy surface", Phys. Rev. B **96**, 205432 (2017) (cit. on p. 94).

[196] G. Füchsel, S. Schimka, and P. Saalfrank, "On the Role of Electronic Friction for Dissociative Adsorption and Scattering of Hydrogen Molecules at a Ru(0001) Surface", J. Phys. Chem. A **117**, 8761–8769 (2013) (cit. on p. 95).

[197] W. Dou and J. E. Subotnik, "Perspective: How to understand electronic friction", J. Chem. Phys. **148**, 230901 (2018) (cit. on p. 95).

[198] J. I. Juaristi, M. Alducin, R. D. Muiño, H. F. Busnengo, and A. Salin, "Role of Electron-Hole Pair Excitations in the Dissociative Adsorption of Diatomic Molecules on Metal Surfaces", Phys. Rev. Lett. **100**, 116102 (2008) (cit. on p. 95).

[199] A. C. Luntz, I. Makkonen, M. Persson, S. Holloway, D. M. Bird, and M. S. Mizielinski, "Comment on "Role of Electron-Hole Pair Excitations in the Dissociative Adsorption of Diatomic Molecules on Metal Surfaces"", Phys. Rev. Lett. **102**, 109601 (2009) (cit. on p. 95).

[200] A. C. Luntz and M. Persson, "How adiabatic is activated adsorption/associative desorption?", j. Chem. Phys. **123**, 074704 (2005) (cit. on p. 95).

[201] A. C. Luntz, M. Persson, and G. O. Sitz, "Theoretical evidence for nonadiabatic vibrational deexcitation in H2(D2) state-to-state scattering from Cu(100)", J. Chem. Phys. **124**, 091101 (2006) (cit. on p. 95).

[202] P. Nieto, E. Pijper, D. Barredo, G. Laurent, R. A. Olsen, E. J. Baerends, G. J. Kroes, and D. Farías, "Reactive and Nonreactive Scattering of H2 from a Metal Surface Is Electronically Adiabatic", Science **312**, 86–89 (2006) (cit. on p. 95).

[203] T. Jaouen, G. Jézéquel, G. Delhaye, B. Lépine, P. Turban, and P. Schieffer, "Work Function Shifts, Schottky Barrier Height, and ionization Potential Determination of Thin MgO Films on Ag(001)", Appl. Phys. Lett. **97**, 232104, 232104 (2010) (cit. on p. 95).

[204] S. Heo, E. Cho, H. I. Lee, G. S. Park, H. J. Kang, T. Nagatomi, P. Choi, and B. D. Choi, "Band Gap and Defect States of MgO Thin Films Investigated Using Reflection Electron Energy Loss Spectroscopy", AIP Adv. **5**, 077167, 077167 (2015) (cit. on p. 95).

[205] R. G. Rowe and G. Ehrlich, "Rotationally inelastic diffraction of molecular beams: H2, D2, HD from (001) MgO", Journ. Chem. Phys. **63**, 4648–4665 (1975) (cit. on p. 99).

[206] G. Brusdeylins, R. B. Doak, J. G. Skofronick, and J. P. Toennies, "Elastic and inelastic scattering of He atoms from the (001) crystal surface of MgO", Surf. Sci. **128**, 191–206 (1983) (cit. on p. 99).

[207] M. Mahgerefteh, D. R. Jung, and D. R. Frankl, "Selective adsorption in ^{4}He-MgO scattering", Phys. Rev. B **39**, 3900–3904 (1989) (cit. on p. 99).

[208] G. Benedek, G. Brusdeylins, V. Senz, J. G. Skofronick, J. P. Toennies, F. Traeger, and R. Vollmer, "Helium atom scattering study of the surface structure and dynamics of in situ cleaved MgO(001) single crystals", Phys. Rev. B **64**, 125421 (2001) (cit. on p. 99).

[209] J. G. Skofronick, J. P. Toennies, F. Traeger, and H. Weiss, "Helium atom scattering studies of the structure and vibrations of H$_2$ physisorbed on MgO(001) single crystals", Phys. Rev. B **67**, 035413 (2003) (cit. on p. 99).

[210] A. Schüller, D. Blauth, J. Seifert, M. Busch, H. Winter, K. Gärtner, R. Włodarczyk, J. Sauer, and M. Sierka, "Fast atom diffraction during grazing scattering from a MgO(001) surface", Surf. Sci. **606**, 161–173 (2012) (cit. on p. 99).

[211] T. Kondo, H. S. Kato, T. Yamada, S. Yamamoto, and M. Kawai, "Rainbow scattering of CO and N2 from LiF(001)", J. Chem. Phys. **122**, 244713 (2005) (cit. on p. 99).

[212] A. Lubezky, Y. Kozirovski, and M. Folman, "IR spectral shifts and adsorption potentials of CO and N2 adsorbed on LiF and LiCl", J. Electron spectrosc. Relat. Phenom. **95**, 37–44 (1998) (cit. on p. 99).

[213] I. McKinnie and H. Kapteyn, "Ultrafast lasers yield X-rays", Nat. Photonics **4**, 149–151 (2010) (cit. on p. 100).

[214] B. W. J. McNeil and N. R. Thompson, "X-ray free-electron lasers", Nat. Photonics **4**, 814–821 (2010) (cit. on p. 100).

[215] T. Ishikawa et al., "A compact X-ray free-electron laser emitting in the sub-angström region", Nat. Photonics **6**, 540–544 (2012) (cit. on p. 100).

[216] J. Hajdu, "Single-molecule X-ray diffraction", Curr. Opin. Struct. Biol. **10**, 569–573 (2000) (cit. on p. 100).

[217] B. von Ardenne, M. Mechelke, and H. Grubmüller, "Structure determination from single molecule X-ray scattering with three photons per image", Nature Comm. **9**, 2375 (2018) (cit. on p. 100).

[218] T. Bredtmann, M. Ivanov, and G. Dixit, "X-ray imaging of chemically active valence electrons during a pericyclic reaction", Nat. Commun. **5**, 5589 (2014) (cit. on p. 100).

[219] V. A. Osipov, M. Kowalewski, and S. Mukamel, "Multiscale wavelet decomposition of time-resolved X-ray diffraction signals in cyclohexadiene", Proc. Natl. Acad. Sci. USA **115**, 10269–10274 (2018) (cit. on p. 100).

Danksagung

Während der letzten 10 Jahre des Studiums habe ich die Freude gehabt von vielen Menschen in meinen Zielen unterstützt zu werden. Von Einigen davon sogar noch länger. Ich möchte daher Allen meinen herzlichsten Dank aussprechen.

Ein besonderes Merci geht an Jean Christophe Tremblay, der mir mit seiner wunderbaren Betreung als Doktorvater geholfen hat, meinen Weg hin zur Promotion zu finden und zu bewältigen. Du hast immer ein offenes Ohr für alle die Fragen und Probleme gehabt und mir auch durch unsere Diskussionen den Blick in vielen Richtungen ermöglicht.

Ein ebenfalls großer Dank geht an Beate Paulus, die mir seit der Bachelorarbeit viel Unterstützung im wissenschaftlichen sowie organisatorischen Bereich gab. Dir habe ich es auch zum großen Teil zu verdanken, dass ich meine Entscheidung, in den Bereich Theoretische Chemie zu gehen, niemals bereut habe.

Zu der schönen Zeit in dieser Arbeitsgemeinschaft haben natürlich auch all die ehemaligen und aktiven Mitglieder beigetragen. Anders wie die Temperaturen im alten Gebäude war das Arbeitsklima durchgehend angenehm. Besonders gilt das für meinen Langzeit-Büromitbesetzer Christian Stemmle. Mit Dir gab es immer gute Gespräche, spaßige Aktionen und einen Ansprechpartner, der mir bei Fragen zu **D**en post-H**F** Me**T**hoden mit **F**ormidablen An**T**worten **W**eiterhalf**!**

Mein Dank geht auch an Axel Haupt, Karsten Sonneberg und Thomas Siemon für die gemeinsame Zeit und Zusammenarbeit in der ersten Hälfte unserer universitären Ausbildung und weiterhin viel Erfolg bei unseren kommenden Aufgaben.

Ein großen Einfluss auf diese Arbeit haben auch alle meine Freunde seit der Schulzeit und danach. Ohne Euch wäre die Arbeit möglicherweise viel früher fertig geworden, alles

andere aber umso mehr langweilig gewesen. Außerdem möchte ich die Unterstützung, die wir uns gegenseitig geben, nicht missen.

Zum Schluss geht das größte Dankeschön an meine Familie, die über die ganze Zeit hinweg an meiner Seite stand und meinen Werdegang all die Jahre lang unterstützt haben. Ihr gabt mir ein Platz voller Geborgenheit und die Möglichkeit der freien Entfaltung.

Danke!